Modeling the Near-Surface
Using
High-Resolution Seismic Data

by

Ramzy M. Al-Zayer

submitted to the graduate degree program in Geology
and the Graduate Faculty of the University of Kansas
in partial fulfillment of the requirements for the degree of
Doctor of Philosophy.

Georgios P. Tsoflias, Co-Chairman

Ross A. Black, Co-Chairman

Committee members

Donald W. Steeples

Daniel F. Stockli

William C. Johnson

Date defended: January 26, 2010

The Dissertation Committee for Ramzy M. Al-Zayer certifies
that this is the approved version of the following dissertation:

Modeling the Near-Surface
Using
High-Resolution Seismic Data

Committee:

Georgios P. Tsoflias, Co-Chairman

Ross A. Black, Co-Chairman

Donald W. Steeples

Daniel F. Stockli

William C. Johnson

Date approved: February 5, 2010

Acknowledgments

I would like to thank all the people who supported me through out my degree program. In particular, I would like to thank my two advisers Dr. George Tsoflias and Dr. Ross Black as well as the other committee members. I also like to thank all the faculty and the students of the Geology Department for their support.

Great appreciation to Saudi Aramco who provided me with the data and continuously supported me through out this dissertation. King AbdulAziz City for Science and Technology (KACST) provided some of the data shown in this thesis. For this and their technical support, I would like to thank them, in particular Dr. Tariq AlKahlifah.

Special thanks to my family who stood beside me all the time. I love you all.

ABSTRACT

In the Arabian Peninsula, the near-surface represents a major challenge in seismic exploration. For accurate deep subsurface reservoir imaging, an accurate near-surface velocity model is required. In this dissertation, I review the regional geology and geomorphology and the existing methods used for velocity modeling. A new method is developed, which depends on acquiring high-resolution shallow seismic data. The data is processed to obtain a near-surface velocity. The numerical modeling shows that the accuracy required for accurate imaging can be obtained through this new method. Alternative existing methods either lack the required accuracy or are very expensive to use. Three real field data cases are presented. In each case a high-resolution velocity model is obtained and used to process the conventional data. To make the new method more practical, I recommend using the CMP mode and a land streamer for data acquisition. I show that some artifacts in the data acquired using a land streamer can be overcome by using optimally-designed plate-mounded geophones. The two main factors in the design are the plate weight and area. From the experimental data, I conclude that land-streamer data over sand dune can be more coherent than conventional data, especially the first-arrival events.

TABLE OF CONTENTS

LIST OF FIGURES

LIST OF TABLES

Page left intentionally blank

Chapter 1

INTRODUCTION

1.1 Problem Definition

Since it was first used in middle of the last century, the seismic reflection method has been the primary tool for subsurface imaging in hydrocarbon exploration. Early seismic data were single-fold, one source and one receiver. Multi-fold coverage was later developed to, statistically, enhance the reflected signal and cancel noise. To obtain the required multi-fold coverage, a spread for 2D acquisition or a swath for 3D acquisition of receiver-groups are used in data acquisition. The degree of the clarity and reliability of the final seismic image depends, partially, on the complexity of the subsurface geology (Yilmaz, 1987).

The technique works the best when the characteristics of shallow and deep subsurface layers, such as velocity and structure vary slowly. Velocity anomalies should have the dimensions of a multiple of spread length. This makes it possible to estimate velocity using the Common-Mid-Point (CMP) gathers. In this dissertation the term CMP will be used interchangablly with the term CDP (Common-Depth-Point). The gathers then are normal-moveout (NMO) corrected using the estimated velocities and stacked to produce the final time-image. In the presence of complex deep subsurface or near-surface, seismic wave propagation becomes more complicated. Processing the seismic

data in such cases becomes more challenging and requires more advanced data processing techniques, such as prestack depth migration and datuming. These techniques were developed over years of research and development. Using simple processing techniques might not be sufficient to produce an accurate and interpretable final subsurface image.

Because of compaction and overburden pressure, seismic velocities of rocks become more stable and consistent with depth. On the other hand, the surface and the near-surface of the earth are usually more heterogeneous. On the surface, different rock types and sediments with large velocity contrasts outcrop next to each other. In addition, the near-surface is almost always heterogeneous vertically and laterally. The geomorphological features through which seismic data are collected are of different scales and complexity. Moreover, they are usually characterized by low-velocity, heterogeneous, weathered, and unconsolidated sediments. The influence of near-surface complex geology on seismic data, 2D and 3D, has been thoroughly investigated (e.g., Yilmaz, 1987, Cox, 1999).

In general, near-surface anomalies, such as wadi-fills, sand dunes, or igneous intrusives, degrade the quality of the final seismic image and should be accounted for to obtain a clear and reliable subsurface image. The seismic section in Figure 1.1 is an example from the the central part of the Arabian Peninsula (Ley et al., 2003). It shows the importance of applying the static corrections to the seismic data before stacking. The corrections lead to improved quality in subsequent processing steps which, in turn, impact the integrity, quality, and resolution of the final image. The effect on the seismic image depends on the size and magnitude of the anomalies relative to the effective

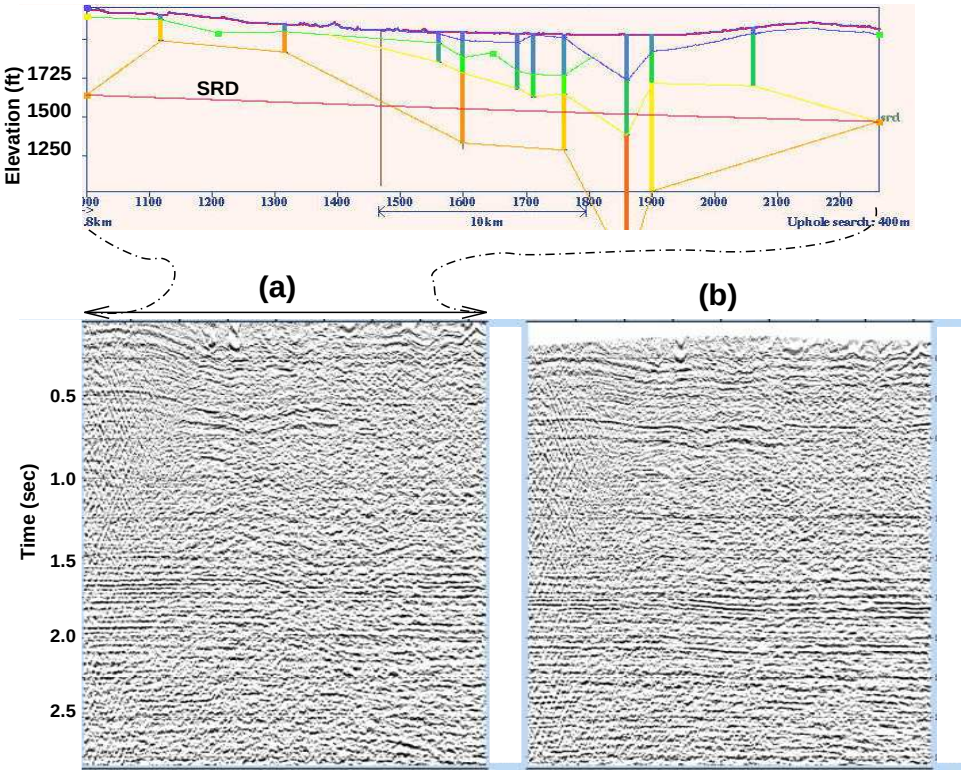

Figure 1.1. An example of a 2D seismic line through a wadi filled with low-velocity sediments. The top profile is a near-surface velocity model constructed from the posted discrete upholes. Three layers can be identified. The top blue layer has a velocity range of 500 to 999 m/s. The green layer has a velocity range of 1000 to 1999 m/s. The yellow layer has a velocity range of 2000 to 2500 m/s. The quality of the final stack is greatly degraded by this LVL, as shown in the surface stack, section (a). The stack quality improves with the application of statics correction, section (b), (Ley et al., 2003).

spread-length, the data after muting refraction and direct waves. There are two ways by which near-surface anomalies affect the final stack. First, they cause misalignment of reflection events, and therefore degrade the resolution of the final stack. Secondly, they create erroneous time-structures in the final stack. Which of these will be observed in the final seismic stack depends on the size and depth of the anomalies and depth of the reflectors.

While the coherency and the resolution of shallow reflections are degraded by small-size velocity anomalies, large-size anomalies mostly affect deep reflections. A given near-surface wide anomaly, creates an erroneous time-structure for a reflector beneath the anomaly. The size of this time-structure depends on depth of both the anomaly and the reflector. The most serious artifact, however, is the distortion in the time isochron, between two reflectors, caused by the differences in dynamic properties, such as velocity and mute functions, and the presence of the near-surface anomalies (GeoQuest, 1976). For all of these reasons, compensating for the near-surface layers is an important step in seismic imaging before any interpretation can be made.

The most commonly used method to remove the effect of near-surface layers is utilizing surface-consistent static time shifts (Figure 1.1) calculated from a near-surface velocity model (Marsden, 1993; Cox, 1999; Ley et al., 2003). In regions where the assumptions behind static-correction solutions are violated, more numerically-complicated approaches have been developed. These solutions are refereed to in the industry as datuming approaches. Some of these are based on Kirchhoff-integral solution (Berryhill, 1979). Others are based on a wave-equation solution (Holberg, 1988). In the industry, however, these techniques are used in limited cases (Hu et al., 2002) because of the high-

accuracy requirement in the velocity model. Whatever correction method is used in the seismic processing flow, the first step always is building an accurate near-surface velocity model.

1.2 Existing Velocity-Model Building Methods

In his book, Cox (1999) has discussed in detail several methods which can be employed to build a near-surface velocity model. Some of these methods are direct, such as estimating the velocity from check-shot surveys. Others use intermediate data, such as refraction travel times, to build the model through an inversion process. The methods can be grouped into five categories; namely uphole-based, refraction-based, elevation-based, reflection-based, and potential- or electrical-field-based methods. The methods in the first three groups are the simplest and the most widely used. The reason for their popularity is mostly economical. Other methods, such as those based on electrical and potential field theory, have been used in limited research studies (Cox, 1999). This dissertation focuses on using reflection-based methods to build the near-velocity model.

The primary technique to build the near-surface velocity model in the Arabian Peninsula is using velocity functions derived from check-shot surveys from upholes, Figure 1.1. The uphole is a shallow borehole, which is usually drilled down to the first high-velocity layer. Upholes are drilled to obtain near-surface velocity information. They are drilled in the exploration area where seismic data are collected. The accuracy of the velocity model depends on the accuracy of each velocity function, the distance between upholes, and the interpolation technique used. In areas where there is a good uphole coverage,

the velocity information from the surface to the SRD (Seismic Reference Datum) using tens of thousands of upholes has been compiled and interpolated to produce a regional velocity-map. The near-surface model for any new 2D line or 3D can be built from this map. This frozen model is believed to be sufficient for most parts of the Peninsula (Bridle et al.,2004). In more problematic areas, more information has been incorporated to enhance the accuracy of the interpolation, for example, using first-breaks to create a multi-layer model (Bridle et al., 2004).

The second approach is the first-break inversion using one of the refraction-based methods, such as the Generalized Linear Inversion, or GLI, and tomography (Hu et al., 2002). Although, these methods provide a better spatial coverage, they have their own issues. The most challenging problem is picking a consistent refractor and obtaining the velocity V_0 from the surface down to the top of the refractor. This problem is minimized by using velocity information from upholes. The industry has accepted this technique as the most accurate model-building process (Cox, 1999).

Most of the studies mentioned above are based on the conventional approaches of applying a surface-consistent static time shift calculated from the derived velocity model. Other, more numerically-complicated approaches have also been used in limited cases in the Arabian Peninsula. Examples include redatuming using either model-dependent algorithms, such as Kirchhoff-based and wave-equation datuming, or model-independent approach, such as Common Focus Point (CFP) datuming (Hu et al., 2002). They all, however, need a reasonably accurate velocity, even the CFP-based algorithm.

The geomorphological features found in the arid Arabian Peninsula can be

found in other arid regions. The features here, however, have different scales and might stack on top of each other, which make the problem more serious. The first four methods from the above list represent the primary choice for explorationists, mainly for an economical reason. To my knowledge, there is no published work which explicitly uses shallow-seismic data to account for the near-surface, except the work of Black et al., (1990). In the next section, I discuss briefly some of the problems associated with uphole- and refraction-based methods to establish the need for a more reliable method.

1.3 Problems Associated with Existing Methods

Medium parameters, such as density and seismic velocity, for both P- and S-waves, and the thickness of near-surface layers vary vertically as well as laterally.

In surface-seismic surveys, these variations are classified as having long, medium, or short wavelength relative to the effective spread-length. This is the longest usable offset beyond which data are usually muted. Since this parameter is time variant, the above classification of the anomalies is also time variant. Short-wavelength anomalies for a deep reflector are considered to be long-wavelength for a shallower reflector.

The influence of a near-surface anomaly on reflection data depends on its relative size and depth. Since the relative size of the anomaly is time variant, its influence is also time variant. For example, while short-wavelength anomalies affect the continuity of shallow horizons, long-wavelength anomalies affect deeper reflections. All anomalies, however, induce erroneous time-variant time shifts. The dynamic non-hyperbolic moveout velocity caused by

the near-surface anomaly contributes to the time-variant time shift. Therefore, the technique to be used is the one which accounts for all near-surface anomalies with all dimensions.

The optimal method, if there is one, should resolve all these variations down to the datum below which the velocity is more stable. No universal method exists today which can be used to build the near-surface velocity model for all near-surface geological conditions. Every method used in the industry has certain limitations. Nevertheless, each has enjoyed some success depending on the near-surface conditions. In this section I outline some of the major problems associated with the main methods; namely, uphole-based and refraction-based methods.

1.3.1 Uphole-based methods

Although the procedure of measuring seismic interval velocities in an uphole, the check-shot survey, is straightforward and simple, picking the travel-time accurately is not. This leads to large errors in the velocity computation.

The cost of drilling an uphole for velocity measurements only is high. The top soil in arid regions is usually unstable, which makes drilling more difficult and hazardous.

For economical reasons, the upholes usually do not penetrate all near-surface anomalies. In fact, many upholes do not penetrate down to the datum. The last sampled point is usually extrapolated to the datum.

The spacing between upholes is usually large, typically within 10 km, which causes the model to have poor spatial resolution that can be improved only through drilling more upholes, making it more cost-ineffective.

Upholes are drilled in accessible locations, which are not necessarily where they are most needed. Using the best interpolation technique then becomes critical.

1.3.2 Refraction-based methods

These methods invert first-break time arrivals to obtain a near-surface velocity model or the static-correction values. Most of the inversion methods are linear and are ray-theoretic, based on the geometrical interpretation of the propagation of refracted waves; the Generalized Reciprocal Method (GRM) and the Generalized Linear Inversion (GLI) methods are two examples (Palmer, 1980; Hampson and Russell, 1984). Non-linear methods employ tomographic inversion (Taner et al., 1998). The problems associated with these methods can be classified into three categories:

Inherent Problems These methods are based on simplified mathematical models, which hardly exist in nature. GRM, for example, is based on a model of a stack of velocity-increasing flat layers, at most dipping. Turning-ray tomography assumes a smooth increasing velocity gradient with depth. Taner et al. (1998) realized this fact and developed his algorithm to solve for static corrections only without the need to raytrace a velocity model.

Most of the methods can not account for pinch-outs, steeply-dipping and hidden layers, e.g., those having a small thickness or a velocity reversal.

The data is assumed to be collected in the plane of incidence, and therefore the apparent dip is modeled as a true dip.

The most serious problem, however, is the nonuniqueness of the inversion process. Although, this is a problem for almost all geophysical problems (Zh-

danov, 2002), it is more serious in the inverse refraction problem. According to Ivanov et al. (2005), the nonuniqueness is of type D which means that there is a continuous range of solutions which satisfies a given set of data. Such an unfavorable type of nonuniqeness can be uniquely solved only by providing abundant a priori information (Ivanov et al., 2005).

Acquisition Problems Picking first break from production records is not only a time-consuming process, but becomes difficult if not impossible in the presence of source-generated noise and wave scattering. Moreover, the acquisition plane is not flat, which causes direct-waves to overlap with refracted waves. The picking process becomes more inaccurate and difficult when the source type is a Vibroseis.

What is more challenging is to associate a range of time-picks to a certain refractor and to be consistent within the zone of investigation.

To image the near-surface correctly, we need to sample the wavefield properly, which means using the right temporal and spatial sampling frequency. For economical reasons, first-break times are usually picked from production shot-gathers whose acquisition parameters are too coarse for building an accurate velocity model.

Interpretation Problems The velocity and depth to the top of the refractor often change rapidly laterally and vertically, even within the critical distance, making it impossible to resolve these anomalies.

First-break times are used to estimate delay-time, vertical-time, and velocity and depth of the refractor. There are several methods which can be used in this inversion, such as ABC, GLI, and tomography methods. In the special

case of fairly smooth refractor, all methods output similar time images, which can be used to obtain a set of static-correction values. To build a velocity model, however, a priori velocity of the layers above the refractor is required.

Yet, the most limiting factor is the need for the a priori velocity or depth information down to the top of the refractor. In certain cases, this information can be obtained from direct waves. In most cases, however, direct waves sample only the top part of the first layer.

Given a perfect, error-free, set of first-break picks and the velocities above the refractor v_0, or depth, the inversion problem is still ill-posed and no unique model can be achieved. This was demonstrated by Zanzi (1990) for linear methods and recently by Ivanov et al. (2005), for all methods. In practice, uphole-velocity profiles are used to resolve long-wavelength variations in the near-surface, larger than or equal to uphole spacing. If successful, a refraction-based method, constrained by the uphole-based velocity information, might resolve the variations with smaller wavelength. In practice, reflection-based auto residual-statics algorithms are used to resolve the variations within a spread-length. The success of these methods depends on data quality, acquisition geometry, and density of coverage. Note also that some of the refraction-based methods, such as GLI (Hampson and Russel, 1984), incorporate refraction residual-statics.

Other techniques, such as gravity, and electrical methods usually have poor spatial resolution and are implemented in limited cases. One can come to a conclusion that a reliable, robust, and cost-effective method still needs to be developed to build the near-surface velocity model.

1.4 Dissertation Objectives

In this dissertation, I study and implement the high-resolution reflection-based methods to parameterize the arid and geologically-complicated near-surface of the Arabian Peninsula. The main technique which I will use is Shallow Seismic Reflection (SSR). The method has, generally, adequate depth of penetration with high temporal and spatial resolution. The depth of penetration can, almost always, be controlled by the source type and power. The velocity model is built directly from the data.

1.4.1 Dissertation Outline

In the second chapter, I review the geology and geomorphology of the Arabian Peninsula. Understanding the local geology helps anticipate where a new approach to near-surface modeling is needed.

In the third chapter, I study, numerically, the needed-accuracy to accurately image deep targets. I then try to build the near-surface model using high-frequency synthetic data.

I study, in two different parts of the Peninsula, the characteristics of real SSR data; in particular, depth of penetration, frequency response, and dominant noise components, such as ground-roll. From such analysis, I optimize source and acquisition parameters to obtain the required data. The SSR method is limited by the shallowest pickable reflector.

I also study the processing steps needed to improve data quality. Some of the expected problems are the statics and ground-roll problems. The statics problem, here, is the high-frequency component affecting stacking quality.

The processed gathers are the input to the velocity-model building proce-

dure. The study of different velocity-analysis procedures and their accuracy is one of the main research items. One of the methods is using reflection tomography, while the other method is the conventional stacking velocity analysis.

There are two ways to use such data; namely using direct estimation of statics from the surface-stack, or building the near-surface velocity model to be used in further processing. Here, I use both methods to correct the conventional low-frequency data and compare the results. From published results, e.g., Black et al. (1990), the SSR-based velocity model can be so accurate that it can be used for intra-array statics corrections. Moreover, there are different ways to use the velocity model to correct the conventional data, the simplest of which is applying surface-consistent static shift to all traces. Here, I also use the derived model as an input to a wave-equation datuming algorithm.

Integrating the SSR with other existing uphole-based velocity data lead to a better inter-uphole interpolation. Also, stacking velocities are used to constrain the refraction-based solution. Both of these approaches are studied together with a comparison between using the SSR only or using existing methods. I also test the accuracy of the model by applying the model to conventional low-frequency data and check it against uphole velocity.

Many researchers and studies have been conducted on how to make the SSR more cost-effective (Van der Veen, 1998, Steeples, et. al., 1999, Tsoflias, et. al., 2006). Here, I explore using some of these methods to estimate near-surface velocity. In the last chapter, I analyze theoretically and practically the land-streamer response. In particular, I study ground-coupling of plate-mounted geophones.

Beside the literature review chapter, the dissertation includes numerical modeling, field data acquisition, and analysis. Seismic data were acquired along exploration 2D lines which have near-surface problems that are were not fully resolved using existing methods. The second step was processing the data to produce velocity models. The resultant models have then been used to calculate the static-correction values. Finally, the exploration 2D lines are corrected using the statics values before they are stacked.

.

Chapter 2

GEOLOGY AND GEOMORPHOLOGY OF THE ARABIAN PENINSULA

2.1 Objective

This chapter is a summary of the geology and geomorphology of the Arabian Peninsula. It includes a brief history and a description of the two main regional terrains: the Arabian Shield and the Arabian Shelf. The geology of the Quaternary geology is emphasized here since the surface and near-surface sediments are of Quaternary and late Tertiary age.

2.2 Structure and Geologic History of the Peninsula

The Arabian Peninsula is a huge crustal plate composed of ancient sedimentary and volcanic rocks, deformed and metamorphosed and injected by plutonic intrusions. The satellite image in Figure 2.1 shows the surface geology of the Arabian Peninsula. Up until the Tertiary period, the peninsula was part of the African Shield. In the late Precambrian, its surface was deeply eroded and peneplained. At the beginning of the Cambrian, a great sedimentary basin, the Tethys geosyncline, had developed in the area now occupied by Turkey, northern Iraq, and southwestern Iran. Thousands of meters of sediments were accumulated in this slowly-sinking region throughout Paleozoic, Mesozoic, and early Cenozoic. At the same time, flat-laying strata were de-

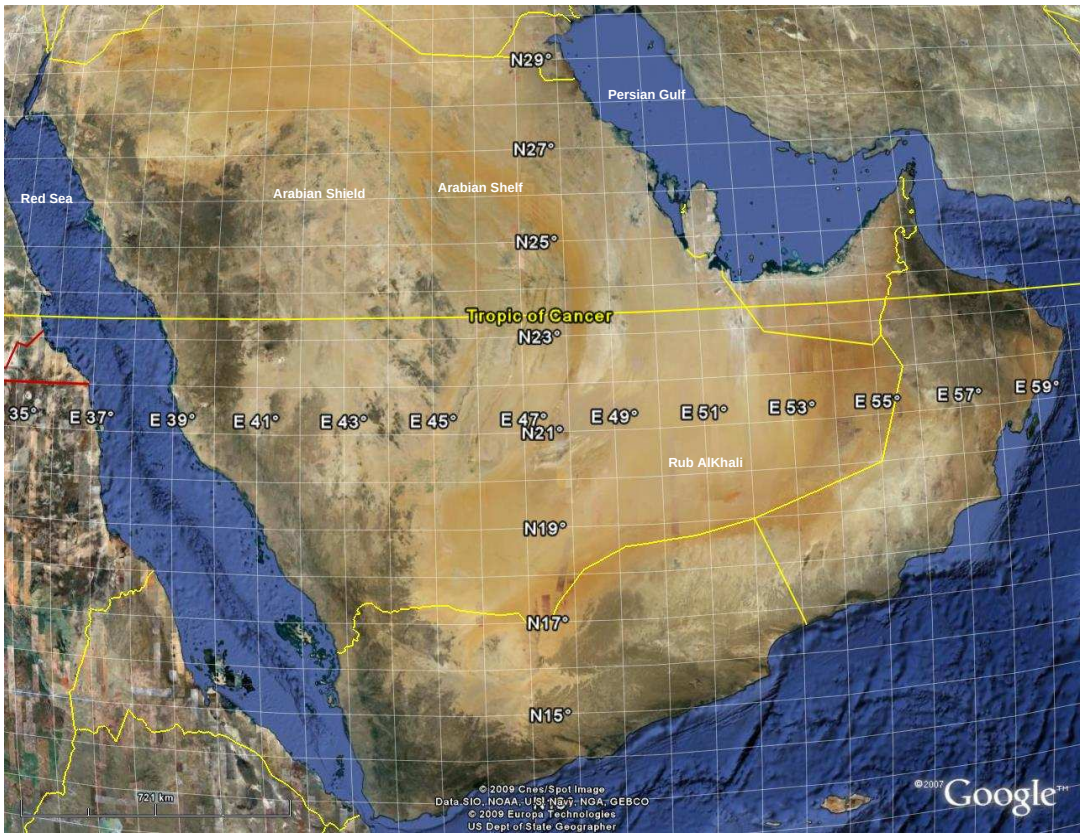

Figure 2.1. A composite satellite image of the Arabian Peninsula showing in detail the surface geomorphology. Notice that the image is blurry in Rub AlKhali because of the low resolution. The image was produced by Google Earth software (courtesy of Google Earth software).

posited in the broad epicontinental seas between the Tethys and the Arabian Peninsula. Continental deposits were laid down inland. In response to slight vertical movements, the transgressions and regressions of the sea gave rise to unconformities (Powers, 1966).

In the late Cretaceous, the first stage of the Alpine orogeny heralded the destruction of the ancient Tethys and caused the strata to fold and overthrust. In the second stage, these deformed strata started to rise forming the Taurus, Zagros, and Oman mountains. In the Arabian Peninsula, this uplift caused a slight eastward tilt of the strata. During the Tertiary orogeny, which began in the middle Tertiary, the Arabian plate split away along the Red Sea trough and began moving northeast against the Asian plate. Throughout the Paleozoic, Mesozoic, and Tertiary, the Arabian Plate and the covering sediments were barely disturbed. Today, the peninsula is divided into two main structural regions: the Arabian Shield, and the Arabian Shelf. Most of the main elements of the tectonics in the Arabian Plate were created after the late Cretaceous (Al-Sayari and Zotl, 1978). The Arabian Shield is part of the Precambrian crustal plate sloping gently toward the north and northeast. It consists of Precambrian gneiss and metamorphosed sedimentary and volcanic rocks that were folded and faulted during the two main orogenies and then intruded by granites. The Hijaz orogeny, which took place 660 MY ago, induced a north-south fold-fault pattern. The younger Najd orogeny, 450 MY, resulted in northwesterly-trending left-lateral faults (Al-Sayari and Zotl, 1978). The Arabian Shelf occupies two thirds of the peninsula east of the shield. The basement is part of the Precambrian plate that makes up the shield. Above the basement is a thick sedimentary sequence, which dips away from the shield

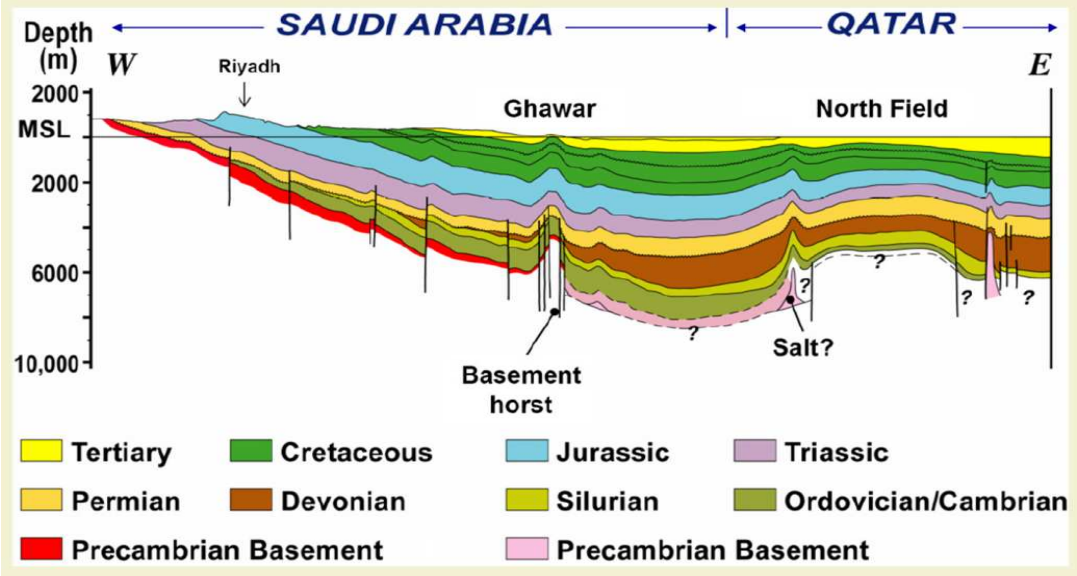

Figure 2.2. A regional 700-km East-West cross section from the Arabian Shield, to the North Field, a giant gas field offshore of Qatar Peninsula (Konert et al., 2001).

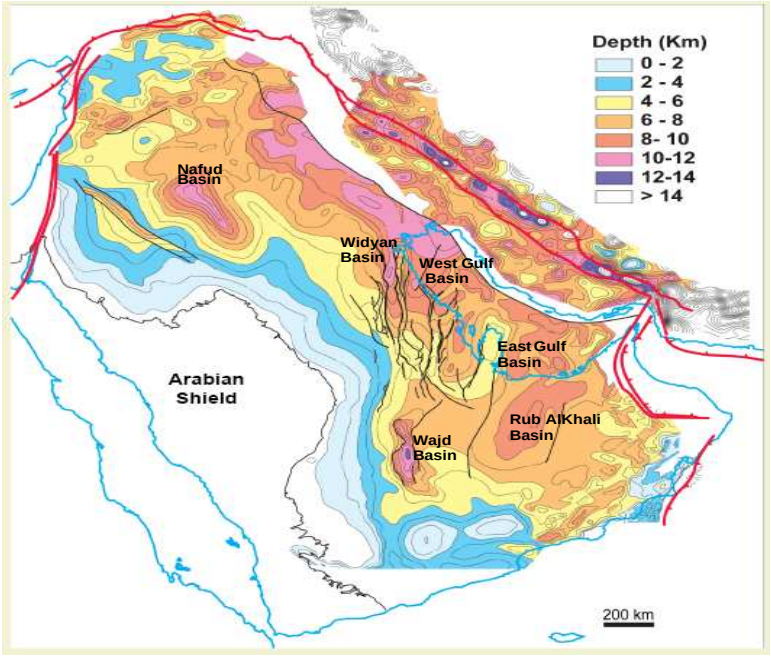

Figure 2.3. A regional depth map of the crystalline basement. The areas where basement is deep have received more sediments to create a local basin or sub-basin (Konert et al., 2001).

into a number of deep basins, e.g. AdDibdibah. The largest of these basins is Rub AlKhali basin. The regional geological cross section shown in Figure 2.2 extends from the Arabian Shield in the west down to the North Field east of Qatar Peninsula. The thickest part of the section, directly below the Western coast of the Persian Gulf, thins out to the west and east. The map in Figure 2.3 shows the depth of the basement in the Arabian Peninsula. It shows the local basins, where most of the petroleum exploration activities occur today. Based on formation dips, the shelf is divided into two major structural features: the Interior Homocline and the Interior Platform. The following is a brief description of these two features.

The Interior Homocline is located along the eastern margin of the shield and extends about 400-600 km outward. The beds in this region are characterized by gentle and uniform dips, less than one degree. One the surface, this structure is covered by the geomorphology of the central and the cuesta regions. The sharp change of the Paleozoic, Mesozoic, and Cenozoic strata in the homocline near latitude 24 degrees is caused by a deep-seated uplift causing a ridge extending all the way to Qatar known as the Arabian arch. The Hail arch, at latitude 27, is a similar structure, which also causes change in strike, see Figures 2.1 and 2.2.

The Interior Platform is a flat structural feature located just to the east of the homocline and separated by an abrupt break in slope, Figure 2.2. Well and seismic information indicate that the sedimentary rocks on the platform are thick and unusually flat. However, several major north-south anticlinal axes rise above the platform. These make up the trap of some of the major oil fields in the Arabian Peninsula, such as Ghawar, Abqiq, and Qatif. Their origin is

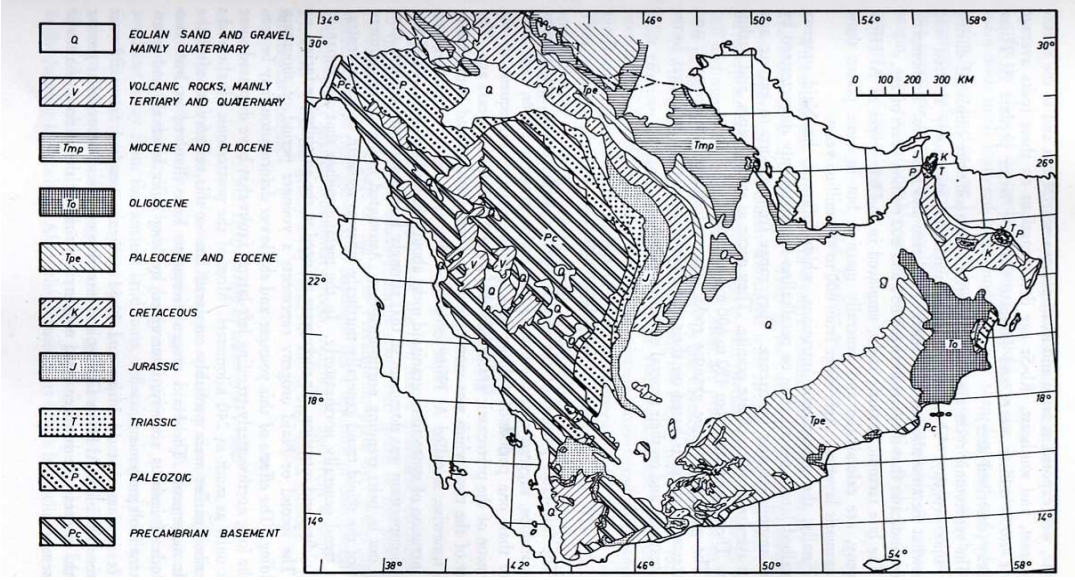

Figure 2.4. A regional surface geology map showing the formations outcrop (Al-Sayari and Zotl, 1978).

believed to be an uplift at great depth. Adjacent to the platform are several sub-basin that have received thick deposits of sedimentary rocks. These basins are shown on the basement depth map in Figure 2.3. The Rub AlKhali basin, the recipient of vast alluvial deposits of late Tertiary time, is the largest of these basins. Deposition into this basinal area provided the substratum from which Quaternary aeolian sands were reworked and on which Quaternary lake beds were deposited.

2.3 Stratigraphy and Sedimentation

One third of the Arabian Peninsula is covered by the non-sedimentary rocks in the Arabian Shield. Except for occasional epeirogenic uplifts, the shield has been tectonically stable since the Cambrian. During this time nearly 5500 meters of sedimentary rock has accumulated on the eastern flank of the

shield. Paleozoic, Mesozoic, and early Tertiary rocks are exposed in the form of escarpments and cuestas bordering the shield in the central part of Arabia. To the east, in the subsurface, these same beds dip gently and uniformly towards the Persian Gulf and into the Rub AlKhali, covered for the most part by late Tertiary and younger Quaternary rocks, as shown in the cross section through the shelf in Figure 2.2.

Shallow, epeiric seas, part of the ancient Tethys Sea realm, lapped onto the shield from the east from Cambrian time onward. The sea retreated gradually and progressively building up and out to the east the thick section or sedimentary rocks. Figure 2.5 shows a generalized stratigraphic section of the layers deposited in the shelf (Jado and Zotl, 1984).

Lower Paleozoic rocks are chiefly medium to coarse grained sandstones of near shore to terrestrial origin. The sandstone layer is interrupted by thin beds of marine shale or limestone. The Permian and Triassic rocks are extensive shallow-water limestones with non-marine clastics toward the top marking one of the brief regressive phases.

Jurassic rocks are almost totally marine and outcrop along the great length of Jabal Tuwaiq, forming the 'spine of Arabia'. They are shallow shelf, very fossiliferous limestones, shales, and marls, with a brief period of shallowing-upward marked at the closing of the sequence by evaporite (Hith Anhydrite) deposition. These shallow carbonates, often of porous calcarenitic (oolitic and pellety) nature, contain much of the oil of Arabia, e.g. Arab Formation. The overlaying anhydrite forms the caprock.

Cretaceous rocks are largely shallow marine limestones, with an extensive thick middle unit of sandstone (Biyadh and Wasia Formations) marking re-

Age			Formation	Generalized lithologic description	Thickness (Type or reference section near outerop)	Aquifer characteristics
Cenozoic	Quaternary and Tertiary		Surficial deposits and basalt	Gravel, Sand, Silt and Basalt		Produce variable quality and quantity of water depending upon recharge by rainfall. Basalt yields little water in western Saudi Arabia.
	Tertiary — Miocene and Pliocene		Al Kharj	Limestone, lacustrine Limestone, Gypsum	28 m.	Generally called Neogene aquifer. Irregular occurences of water. Artesian and non-artesian conditions. Prolific aquifer in the areas of Al Hasa, Wadi Miyah and some others in Eastern Province.
			Hofuf	Sandy marl and sandy Limestone	95 m.	
			Dam	Marl, Shale, subordinate Sandstone	91 m.	
			Hadrukh	Calcareous, silty Sandstone	84 m.	
	Eocene	Lutetian	Dammam	Limestone, Dolomite	33 m.	Produces moderate amount of water with artesian and non artesian conditions.
		Ypresian	Rus	Marl, chalky Limenstone	56 m.	Productivity unknown.
	Paleocene	Thanetian	**Umm er Radhuma**	Limestone, dolomitic Limestone	243 m.	One of the **most prolific aquifer** of the Kingdom with high transmissibility varying between 500,000 and 3 million gpd/ft.
		Montian(?)				
Mesozoic	Cretaceous	Maastrichtian	Aruma	Limestone	142 m.	Yields little water of low quality.
		Campanian				
		Turonian(?)	**Wasia** (Sakaka sandstone northwest Arabian)	Sandstone, subordinate Shale	42 m.	Low productive or even dry near outcrop, very **high productive artesian and non-artesian conditions in Eastern Province.** Hydraulically interconnected with Biyadh near outcrops.
		Cenomanian				
		Aptian	Biyadh	Sandstone, subordinate Shale	425 m.	**Moderately productive sandstone aquifer,** hydraulically interconnected with Basia near outcrop.
		Barremian				
		Hauterivian	Buwaib	Biogenic Calcarenite and calcarenite Limestone	180 m.	Productivity low or unknown.
		Volanginian	Yamama	Biogenic Calcarenite	46 m.	Productivity low or unknown.
		Berriasian	Sulaly	Chalky aphapitic Limestone	170 m.	Productivity low or unknown.
	Jurasic		Hith	Anhydrite	90 m.	Yields always mineralized water.
		Tilhonian	Arab	Calcarenite, calcarenite & aphanitic Limestone	124 m.	Yields little amount of water, mostly mineralized. Irregular occurence of water.
		Kimmeridigian	Jubaila	Aphanitic Limestone	± 118 m.	Similar to Arab Formation above.
			Hanifa	Aphanitic Limestone	113 m.	Unknown productivity.
		Oxfordian — Callovian	Tuwaiq Mountain	Aphanitic Limestone	203 m.	Productivity unknown.
		Callovian(?) — Bathonian — Bajocian	Dhruma	Aphanitic Limestone Sandstone south of 22° N, and north of 26° N	375 m.	Produces moderate amount of water north of 26° N and south of 22° N where it is generally represented by sandstone. South of 22° hydraulically connected with Minjur.
		Toarcian	Marrat	Shale and aphanitic Limestone	103 m.	Yields little water fair to poor quality.
	Triassic	Upper	**Minjur**	Sandstone, Shale	315 m.	Generally **highly productive sandstone aquifer** with flowing and non-flowing artesian conditions.
		Middle	Jilh	Aphanitic Limestone Sandstone and Shale	± 326 m.	Mostly hydraulically interconnected with Minjur, produces low quality water.
		Lower	Sudair	Red & Green Shale	116 m.	Aquiclude.
Paleozoic	Permian	Upper	Khuff	Limestone and Shale Sandstone south of 21° N	171 m.	Moderately productive limestone aquifer, mostly mineralized water.
		Lower	**Wajid**	Sandstone	950 m. Calculated	**Highly productive sandstone aquifer** with flowing and non-flowing artesian conditions.
		Undated				
	Devonian	Lower	Jouf	Limestone, Shale & Sandstone	299 m.	Productive generally in Al Jouf area.
	Ordovician and Silurian		**Tabuk**	Sandstone and Shale	1072 m.	**Productive sandstone aquifer** with flowing and non-flowing artesian conditions.
	Cambrian		Saq { Umm Sahm, Ram, Quwiera, Siq }	Sandstone	± 600 m.	**One of the most productive Sandstone aquifers of Saudi Arabia,** with flowing and non-flowing artesian conditions.
Precambrian Basement Complex						

Figure 2.5. The regionalized stratigraphic column of the Arabian Peninsula.

gional epeirogenic uplift and near continental conditions of deposition in the east.

Upper Cretaceous and lower Tertiary rock sequences consist of limestone and dolomite with some shales. They are extensively exposed at the eastern edge of the escarpment belt, continuing northward into Iraq.

The last remnant of the Tethys Sea retreated from Arabia toward the end of the Eocene. The extensive Pre-Neogene unconformity marks the end of Eocene deposition. In the late Tertiary time, continental deposition, with a brief middle Miocene shallow marine incursion, prevailed in Arabia.

Late Tertiary rocks (Miocene and Pliocene) are on the order of 200 to 600 meters thick. Lithologically, they comprise a heterogeneous mixture of marly sandstones, sandy marls, sandy limestones and green and red claystones. They blanket the Rub AlKhali basically leveling it off and attaining maximum thickness in the central part of the region. They also cover much of the northeast Arabia.

Quaternary deposits of great sand sheets, dune fields and gravel plains directly overlie the Miocene-Pliocene sequence. Sands of the Rub AlKhali in the south-central Arabia alone cover about 600000 square kilometers.

Most of the surface-seismic problems are associated with near-surface geological features of late Tertiary and/or Quaternary age. Because of the low-velocity nature of these sediments, the problems become more serious.

2.4 Regional Geomorphology of Arabia

Al-Sayari and Zotl (1978) and Jado and Zotl (1984), provide a comprehensive description of the Quaternary geology and geomorphology of the Arabian

Peninsula especially the Central and the Eastern Saudi Arabia.

At the end of Eocene, the last remnant of the Tethys Sea retreated from the Arabian Peninsula as a result of eastward movement of the Arabian plate against the Asian plate. This movement resulted in a northeast tilt of the Arabian plate and the upthrusting of the Zagros Mountains about 3 MY ago. The formations, which were deposited as a result of these activities, were the Hadrukh, Dam, and Hofuf, of Early Miocene, Middle-Late Miocene, and Pliocene ages, respectively.

As a result of these activities, concurrent with the Pliocene pluvial periods, the great through-drainage wadis of the Arabian Peninsula were incised, while the shield has been tectonically stable except for occasional epeirogenic uplifts. Wadi AdDawasir and wadi AsSahba drained the west and the central shield and fed to Rub AlKhali. The ArRimah wadi system drained the north-central shield and discharged at the head of the Arabian Gulf.

The map in Figure 2.6 shows the principle geomorphological features in the Arabian Peninsula. The main provinces are: Arabian Gulf Coastal Region, AsSumman Plateau, Eolian Sand Areas, Cuesta Region, Central Plateau Region, Mountains of Western Arabia, Red Sea Coastal Plain, Mountains of Southern Arabia, and Oman Mountains.

Here, I give a brief description of the first four regions and the main morphological features dominating them. For more information, consult Al-Sayari and Zotel, 1978. The Arabian Gulf Coastal Region is bounded between the Gulf in the east and the AsSumman plateau in the west as shown in the generalized geologic map in Figure 2.7. The elevation rises gradually at a rate of 1 m/km inland to the western boundary, the escarpments of AsSumman

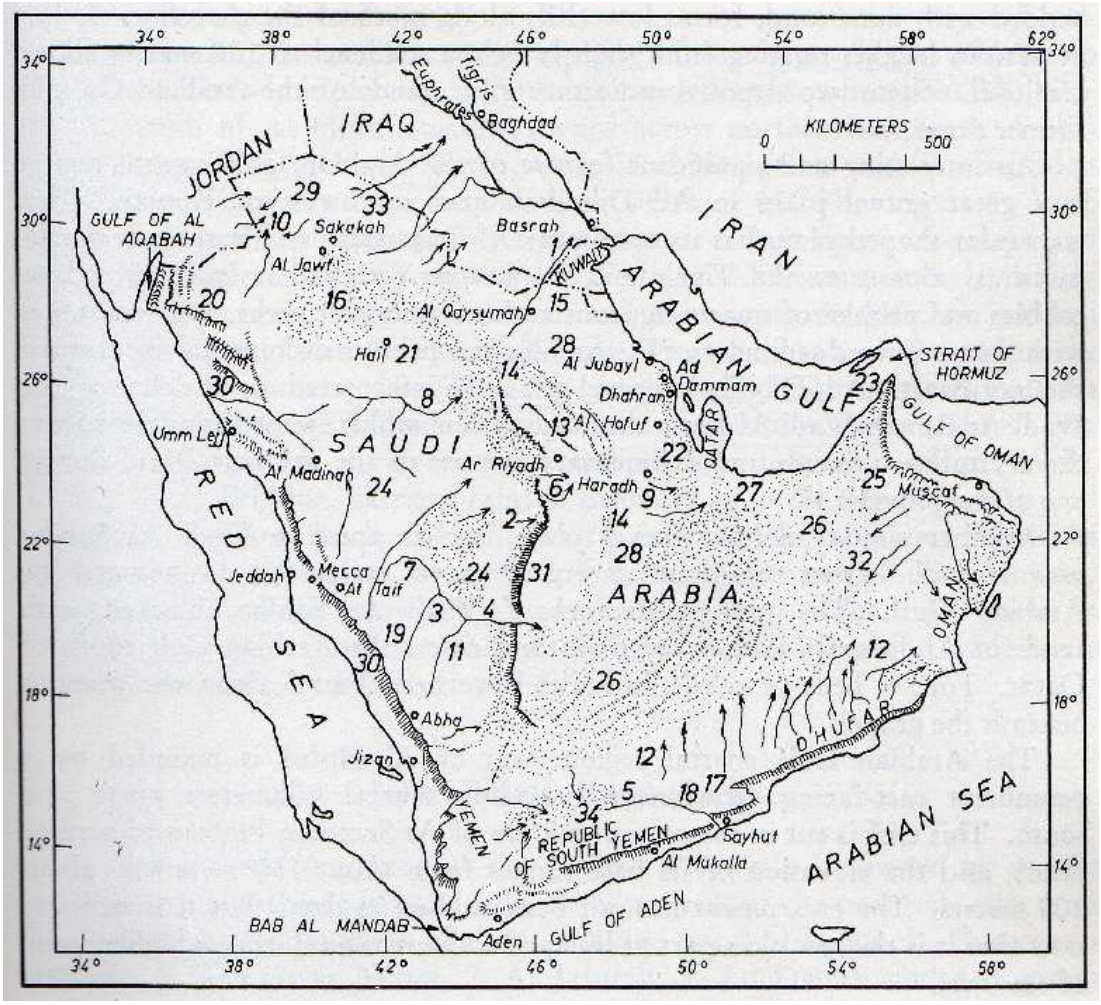

Figure 2.6. Map of the Arabia Peninsula showing the principal geomorphological features in the Arabian Peninsula. Numbers indicate the locations of following wadis: (1) Wadi AlBatin, (2) Wadi Birk, (3) Wadi Bishah, (4) Wadi AdDwawasir, (5) Wadi Hadhramawt, (6) Wadi Nisah, (7) Wadi Raynah, (8) Wadi ArRimah, (9) Wadi AsSahba, (10) Wadi AsSirhan, and (11) Wadi Tathlith. Also, the following landforms are shown: (12) Aden Hinterland, (13) AlAramah Escarpment, (14) AdDahna Desert, (15) AdDibdibah Plateau, (16) Great Nefud Desert, (17) Hadhramawt Plateau, (18) Hadhramawt Valley, (19) Hijaz Plateau, (20) Hisma Plateau, (21) Jabal Shammar, (22) AlJafurah Desert, (23) Musandam Peninsula, (24) Najd Pediplain, (25) Oman Mountains, (26) ArRub AlKhali, (27) Sabkhat Matti, (28) AsSumman Plateau, (29) Syrian Plateau, (30) Tihamah Mountains, (31) Tuwayq Escarpment, (32) Umm AsSamim Desert, (33) AlWidyan Plateau, and (34) Yemen Highlands (Al-Sayari and Zotl, 1978).

plateau. The salt flats or sabkhas can clearly be seen in the satellite image (Figure 2.1), the biggest sabkha is Sabkhat Matti near Qatar. They are most common along the shoreline between Abqaq, in the south, and AsSafanya, in the north. Sabkha can exist as far as 70 km from the Gulf at an elevation of about 150 m. These flat features are composed of layers and mixtures of sand, silt, mud, and salt to a depth of several meters. Except for operational problems, sabkhas are usually not problematic for surface seismic surveys.

The second dominant feature is the eolian sand, which covers a large part of the Gulf region. It is thin and hummocky north of AlJubail, with large dunes south of Dhahran, where it merges with AlJafurah desert, west of AlHassa oasis. In areas where there is no sand or sabkha, the surface consists of limestone outcrops.

Two great triangular-shaped gravel plains exit in this region; one is in the north, AdDibdibah gravel plain, and the other one is in the south, beneath AlJafurah sand. AdDibdibah plain has its apex in wadi AlBatin, and the south plain has its apex in wadi AsSahba. Both plains are interpreted as deltas of old drainage systems.

AsSumman Plateau is a long, flat plateau, overlain by lithified bedrocks. It begins at a point 300 km south of AlHofuf and extends toward the northwest to Syria. The width of the plateau ranges from 50 km in the south to 650 km in Syria. The elevation of the plateau in Saudi Arabia ranges from 400 m in the west to 250 m in the east, the average eastward dip gradient is 0.7 m/km. Figure 2.7 shows the geology of part of AsSumman Plateau located in the Eastern Province of Saudi Arabia.

The bedrock is a permeable flat-lying fresh-water sandy limestone riddled

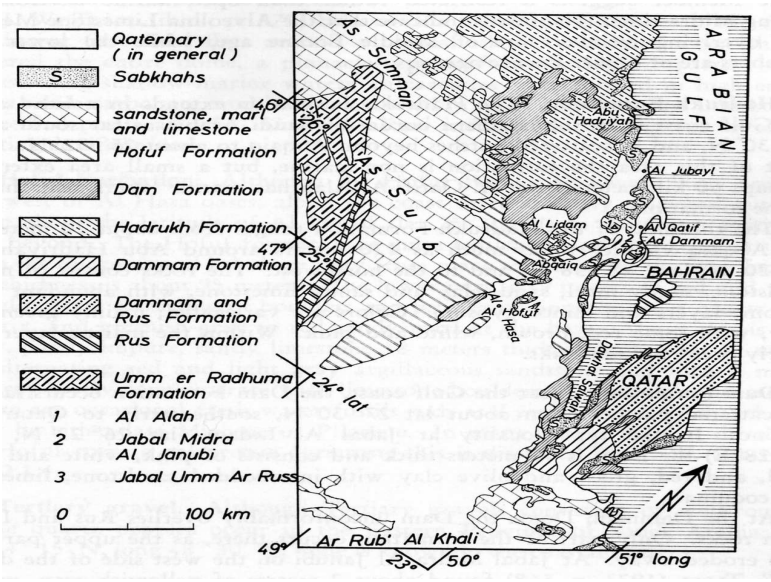

Figure 2.7. Geological map of part of AsSumman Plateau (Al-Sayari and Zotl, 1978).

with broad shallow sinkholes, solution cavities and caves, karst topography. Carbonate enrichment developed a massive duricrust on the surface, which is about 3 m thick today. AsSulb Plateau, the largest part of AsSumman Plateau, occupies its central region. The other important part of AsSumman Plateau is the Shadgum plateau, beneath which lies the giant Ghawar oil field. The east-facing escarpments are indented by innumerable small wadis, about 1 km in width, and some larger wadis with several clearly defined tributaries, such as Scribners Canyon.

The Cuesta Region is a ridge with an escarpment at the western end, which sweeps around the central plateau, and dips eastward below the Ad-Dahna desert. The width of this region is over 250 km (see the map in Figure 2.6). The largest escarpment, the Tuwayq Escarpment, is 800 km long and rises about 240 m above the plains to the west. The ArRimah Escarpment

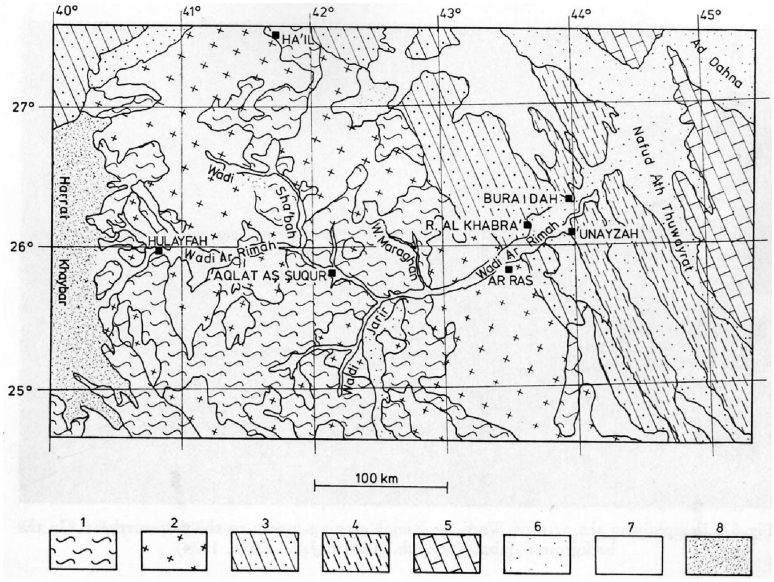

Figure 2.8. Geologic map of wadi ArRimah (one of three major wadi systems in the central part of the Arabian Peninsula). Generalized after U.S. Geol. Survey and Arabian American Oil Company. Numbers in the legend are for (1) metamorphic rocks, (2) granite, (3) sandstones, (4) sandstones and gypsiferous, (5) carbonate rocks, (6) eolian sand, (7) alluvium and related surficial deposits, and (8) Tertiary and Quaternary basalts (Al-Sayari and Zotl, 1978).

is approximately 250 km long, and stands only 120 m above the plains. The escarpments are truncated by a number of major wadi channels that give rise to geomorphical features that influence surface seismic surveys. Examples of such channels are wadi AdDawasir, wadi AlBirk, wadi AlHawtah and wadi AlNisah, with an eastward drainage. Wadi ArRimah, shown in the Figure 2.8, truncates ArRimah escarpment north of Riyadh, and drains in the coastal region as Wadi AlBatin.

The Eolian Sand Areas covers one third of the Arabian Peninsula. Geologists recognize four classes of eolian sand dunes in the Arabian Peninsula. According to their shapes, they are classified into: Transverse, Longitudinal,

Uruq, and Mountainous sand dunes. These sand bodies are distributed regionally in five terrains, as shown in Figure 2.6 and the image in Figure 2.1.

AlJafura desert lies within the coastal region. It widens rapidly to the south, where it eventually merges with the sand of Rub AlKhali.

The Great Nefud desert in the southwestern part of the peninsula covers AlJawf-Sakakah Basin. Its reddish sand form rolling dunes with sparse vegetation, a region without streams or oases.

The AdDahna desert is a long narrow belt of shifting sand and dunes extending nearly 1300 km in a broad arc from the Great Nefud in the north to Rub AlKhali in the south. It lies between AsSumman Plateau on the east and the cuesta region on the west. The quartz sand grains, in AdDahna and Rub AlKhali, are red-to-orange in color due to the coating by iron oxide.

Rub AlKhali is the largest continuous body of sand in the world, 0.6 million km^2. Enormous groups of sabkhas interspersed among the sand dunes exist in the eastern part of the desert. Grains size of the sediments, from the shield and the sedimentary rocks, grade down from coarse to very fine as they spread out to the east. The sediments reach the maximum thickness of 600 m in the central Rub AlKhali. This influx of alluvial sediment into the basin continued to the arid era in the Pleistocene. The Quaternary sediments of Rub AlKhali, therefore, are basically reworked Pliocene alluvial sediments. The unconsolidated sediments grade down to subsurface consolidated sediments of the Neogene 'undifferentiated' such as the Hofuff formation. Beside these large bodies of sand, there are some smaller bodies to the west of the Tuwayq Escarpments.

2.5 Geomorphological Classification

Features affecting surface seismic data are either on the surface or near the subsurface. Morphological features affecting the quality of seismic data acquired in the Arabian Peninsula can be classified into three zones:

Zone one: The surface in this zone is relatively flat or having low-relief dunes. Although no surface-related problems are expected here, subsurface anomalies are possible. Karsting and anhydrite dissolution are some of the well-known problems in Eastern Saudi Arabia. Most of the coastal regions of the Gulf and the Red Sea are of this zone. The AsSumman Plateau has a flat surface, but has large problematic sink holes.

Zone two: This region is characterized by a uneven surface with serious scattering. This zone occurs mainly along wadis and in the cuesta region in the central region. The zone can be outlined using elevation mapping.

Zone three: The surface is covered by sand dunes which cause poor signal penetration and seismic stacking coherency. The three main sand bodies are in the AlNufud, Rub AlKhali, and AdDahna deserts.

It is also possible to get a combination of zone one with any of the other two zones. The problem then becomes more serious with multiple features to resolve.

Chapter 3

NUMERICAL MODELING

3.0.1 Objective

The objective of this chapter is to numerically study the effects of a complex near-surface layer on synthetic seismic data. I implement the two most widely used correction-estimation methods: refraction-based and uphole-based methods. To overcome the shortcomings of these conventional methods, I apply the proposed method of using high-resolution seismic reflection data to construct the velocity model. The data modeling algorithm used here is a finite difference (FD) modeling program from Seismic Unix (CWP, 2005).

3.0.2 Introduction

There is no optimal method to build a velocity model, but the most widely used methods are those based on shallow uphole or refraction data. The best solution is one which incorporates uphole information and as many different wave types as possible (Vesnaver, 2001). This chapter examines the required accuracy needed to image a subsurface target accurately. The accuracy of the velocity model derived from different methods are compared to justify using the reflection-based methods.

In the first part of the chapter, numerical modeling is used to study the effects of a complicated near-surface layer on seismic data and how it influences

the final time and depth images. The near-surface model is built using different methods and the results are qualitatively assessed and compared.

3.0.3 Modeling Parameters

In this section, I use four (Model 1 to Model 4) different two-dimensional (2D) earth models to create synthetic seismic data. The synthetic shot gathers were processed to produce a final stack. All the numerical models used here are 12000 m in length by 1200 m in depth and use 5-m square cells. In addition, all models consist of four major layers plus a near-surface layer. All the layers have a constant density, 1.6 g/cm^3, but different P-wave velocities. The velocity for each of the four major layers is constant, but increases with depth of the layers.

The geometry and parameters of reflectors number one to four were kept unchanged for all models (Figure 3.1). The difference between the different models, however, is in the degree of complexity of the first low-velocity-layer, or the LVL. The base of the LVL, or top of the bedrock, was modeled to be complex, creating variations in the layer thickness. The three models have increasingly more complex geometry of the base of the LVL. In the fourth model, the velocity of the LVL was modeled to vary laterally. The anticlinal feature shown in the fourth reflector, see the model in Figure 3.1 for example, simulates a structural target. Also, a wadi feature was placed in the LVL directly above the target.

Using the acoustic finite-difference Seismic Unix (SU) program fdmod2d, two datasets were created using entirely different modeling parameters listed in Table 3.1. The two datasets simulate conventional and high-resolution seis-

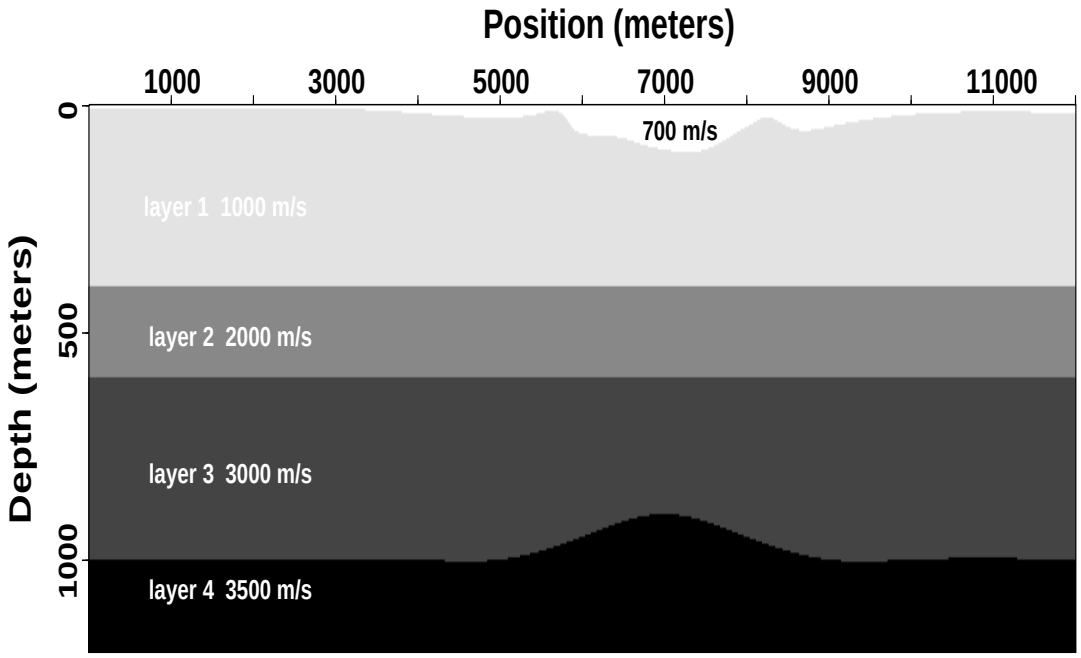

Figure 3.1. Model 1 consists of a stack of four layers plus a Low-Velocity-Layer (LVL). The density of all the layers is kept constant at $1.6\,\mathrm{g/cm^3}$. P-wave velocities increase with depth, but are held constant in each layer. The model is 12000 m in length and 1200 m in depth.

mic acquisition procedures. Since the exploration targets are usually deep, conventional acquisition parameters are routinely used in the hydrocarbon-exploration industry. An identical source wavelet was used for both datasets: the zero-offset Ricker wavelet shown in Figure 3.2. The frequency bandwidth, however, is much larger in the case of the high-resolution dataset. Figure 3.3 shows a sample shot gather, which was actually taken from Model 4 dataset. The reflection from the LVL is not clear, but the reflections from the deeper reflectors are evident.

parameter	conventional	high-resolution
receiver interval	30 m	2 m
traces/shot	101	101
source interval	30 m	4 m
spread	split	off-end
CDP interval	15 m	1 m
maximum fold	51	25
dominant frequency	35 Hz	150 Hz
sampling interval	4 ms	0.5 ms

Table 3.1. Modeling parameters for conventional and high-resolution data.

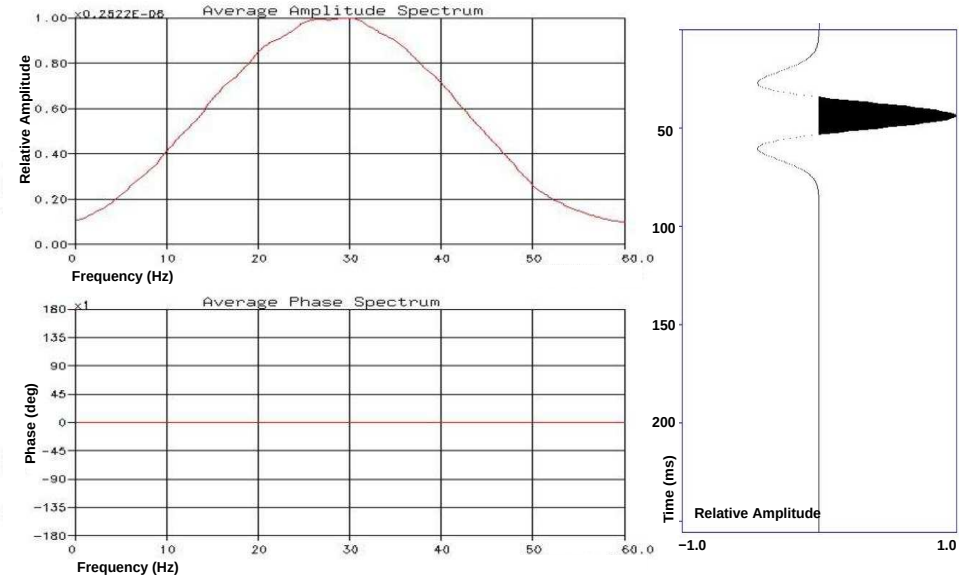

Figure 3.2. The source wavelet used in all the FD modeling is shown to the right. The same wavelet is shown again to the left, but in the frequency domain.

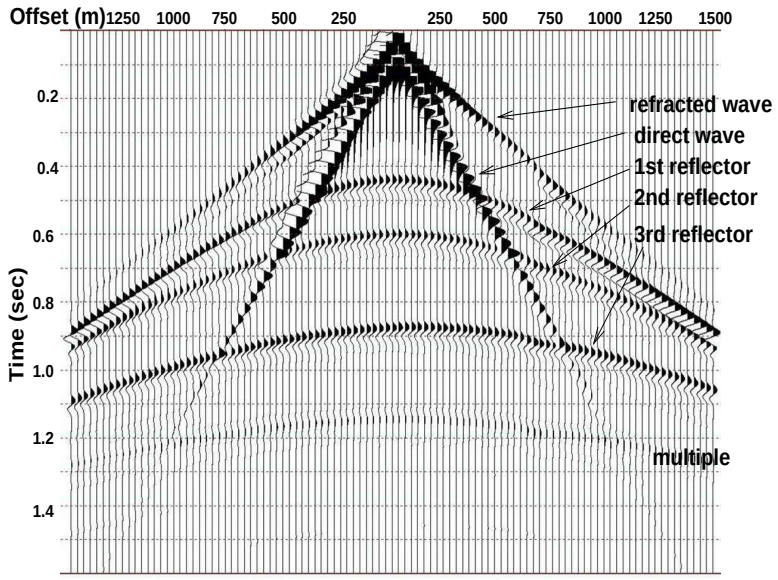

Figure 3.3. A sample synthetic common-source gather taken from Model 4 dataset. Notice that reflected and refracted waves are accurately modeled, but no surface waves.

3.0.4 Influence of the Near-Surface

The thickness of the LVL in Model 1, shown in Figure 3.1, varies slowly to simulate a gravel-plain and a wadi-fill or alluvium. In reality, however, this layer might have more complicated characteristics such as pinchouts or truncations. Also, the sediments of the LVL are usually more heterogeneous than what is assumed in this model. The influence of the LVL becomes more pronounced with increasing complexity. To illustrate this point, two other new models were created by introducing a sinusoidal variation in the LVL thickness of Model 1, Figure 3.1. The spatial wavelength of the variations in the second model, Model 2, is 500 m and 200 m in the third model, Model 3. Relative to the 1500-m spread length, the variations in Model 3 are considered to be high-frequency, while those in Model 2 are considered to be medium- to high-

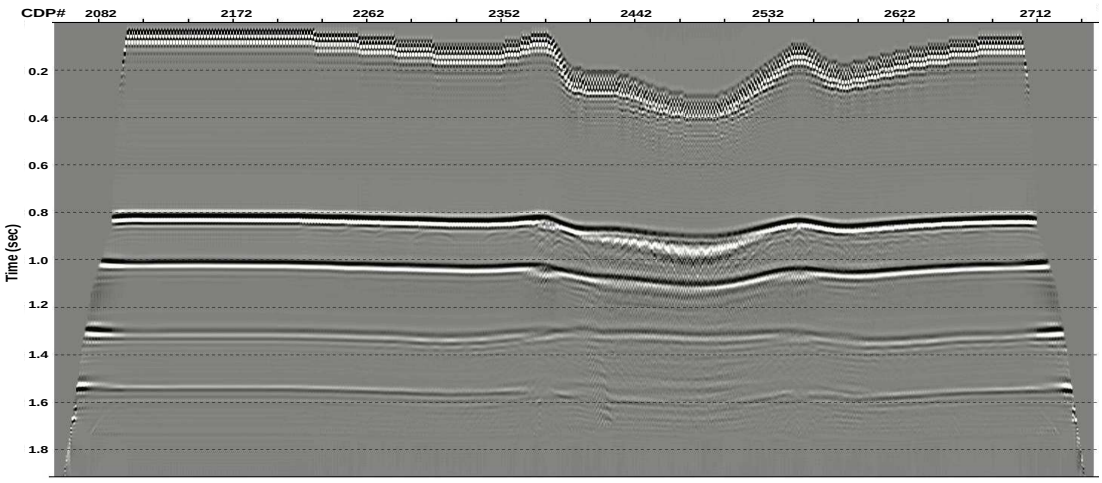

Figure 3.4. Surface stack of the conventional data over Model 1. Coherency of the horizons suffer minor degradations, but the time image does not resemble that shown in Figure 3.1. In particular, the structure has been totally eliminated.

frequency at the target level. The thickness of the LVL changes more rapidly in Model 2 and Model 3 than Model 1.

The modeled shot gathers were then processed to generate an interpretable stack. The data processing sequence included sorting into CDP gathers, static corrections, normal moveout (NMO) corrections, muting, and stacking. To demonstrate the influence of the LVL on the time image, the data were first stacked without applying any static corrections. The stack in Figure 3.4 shows how the target structure has almost been eliminated by the effect of the long-wavelength variation in the LVL thickness. The short-wavelength components caused the poor stack response, see Figure 3.4. Of course, models dominated by small-wavelength components usually suffer more degradation in stack quality as can be seen in the surface stack for Model 2 and Model 3, Figure 3.5 and Figure 3.6, respectively. The degree of stack-quality degra-

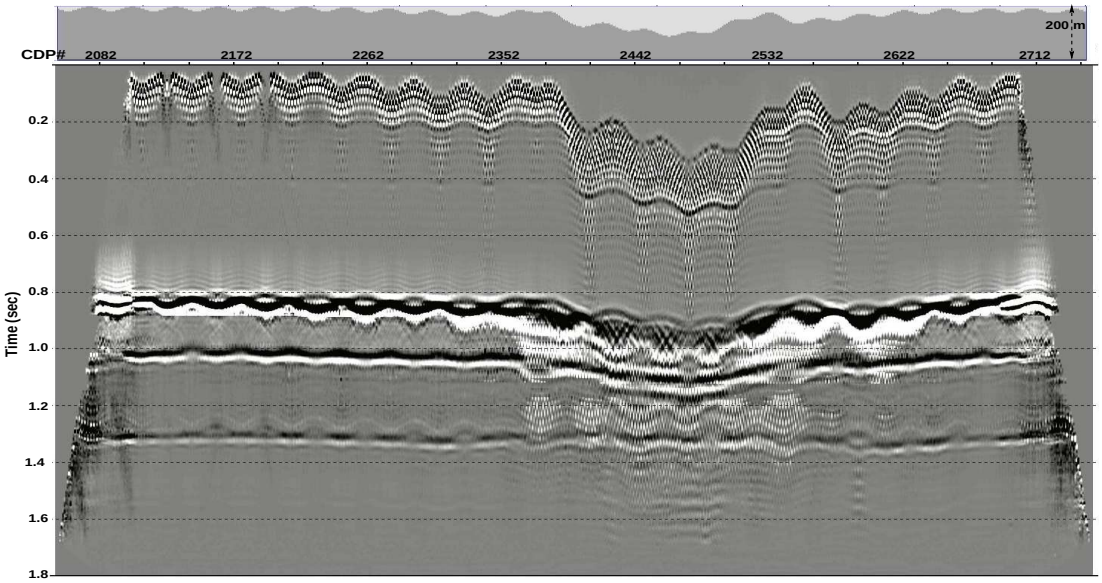

Figure 3.5. The exact near-surface velocity model of Model 2 (top), and the surface stack of the synthetic data over the same model (bottom). Notice how the degradation is more noticeable here than that shown in Figure 3.4 especially for shallow reflectors.

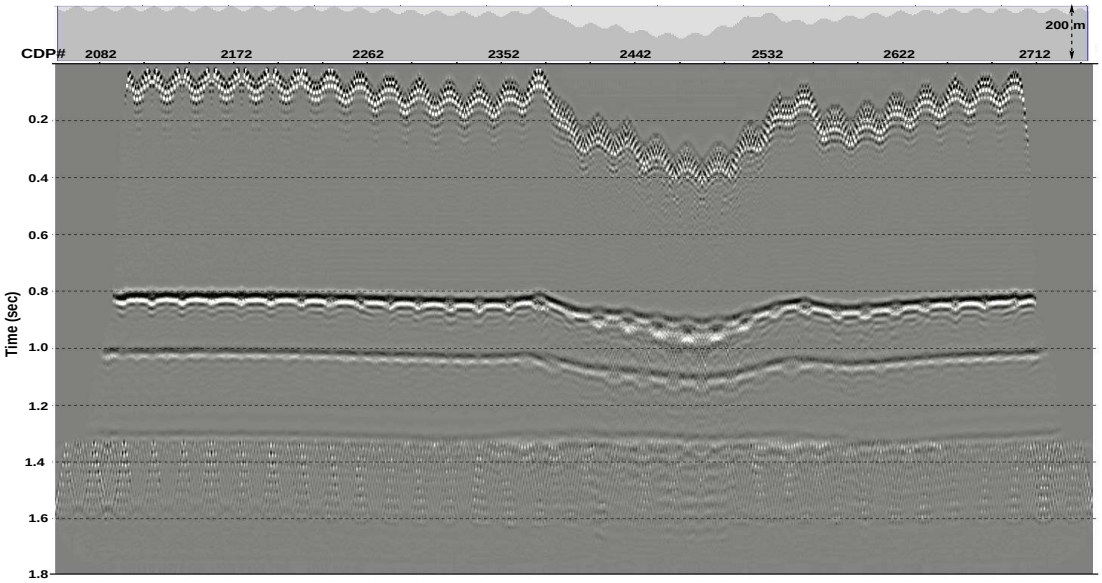

Figure 3.6. The near-surface velocity model (top) of Model 3, and the surface stack (bottom) of the synthetic data over the same model. Notice how the degradation is more noticeable here than that shown in Figure 3.5 especially for shallow reflectors.

dation is frequency-dependent. Because of the low-frequency content in the input wavelet, only mild degradations are observed.

The surface stacks shown in Figures 3.5 and 3.6 are clear examples of the fact that larger complexities in the near-surface result in more distortions to the stack, especially for shallower reflectors. Wavefront healing reduces the influence of the near-surface inhomogeneities in the reflections of deeper layers. Because of earth filtering, high-frequency contents of the signal usually decays with depth. Because of the low-frequency content, deep reflections suffer less from the LVL. The degradation in the CDP stack response depends, also, on the magnitude of the time shift caused be such anomalies. The effect on a particular horizon ranges from low-frequency response due to incoherent stacking to a total elimination in extreme cases.

3.0.5 Correcting for the Near-Surface

To eliminate these artifacts from the data and therefore from the stack, the sources and receivers need to be redatumed below the complicated near-surface layer. Using the simple static correction, the redatuming was calculated from an estimated velocity model. In the more complicated cases such as Model 4, wavefield extrapolation is necessary. In the introduction chapter, I have reviewed some of most commonly used methods to build the near-surface velocity model: uphole-based and refraction-based methods. Both methods were tested to demonstrate the shortcoming of these methods when dealing with a relatively complex near-surface.

First, in order to validate the static correction approach for this model, the data were corrected using the exact statics values, which were directly

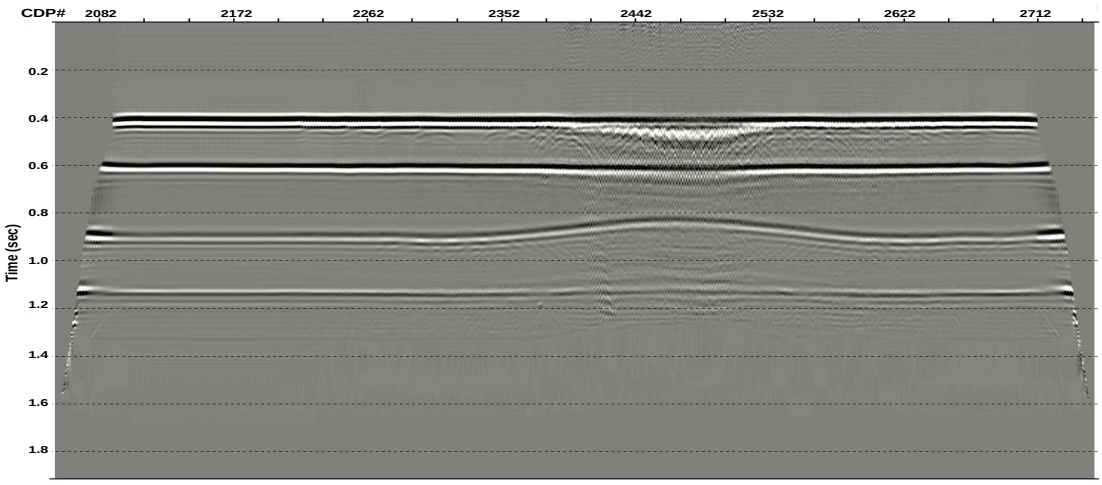

Figure 3.7. The initial stack over Model 1 after applying the exact static correction values calculated from the true model. Notice that we use a flat reference datum below the LVL.

calculated from the LV layer of the true model, Model 1 in Figure 3.1. These values were then applied in the seismic data processing sequence. The final stack, shown in Figure 3.7, indicates that this approach eliminated the artifacts associated with the LVL. In particular, there was no misstacking and the final time image represents the true model with reasonable accuracy. The small non-flatness observed in the first horizon below the alluvium is a clear indication that the vertical-ray assumption, the base of static correction approach, is violated here.

To demonstrate the applicability of the refraction-based methods, one of these methods was applied to Model 1 and Model 2 in an attempt to obtain an accurate near-surface depth model from a set of observed first-arrival time picks. The method used here is the Generalized Linear Inversion algorithm, or GLI, implemented using commercial software from Hapmson-Russell Inc. (Hampson and Russell, 1984). Refraction arrival-times were picked and input

to the software, together with the acquisition geometry. The initial model, which was built using discrete control points along the line, was iteratively updated in order to fit the calculated refraction times with the observed times. The velocity above the refractor V_0 needs to be given as apriori information. The program updates the depth and velocity of the refractor. At the end of the process, the GLI software calculates and applies refraction residual statics. Refraction residual statics are those static corrections which best align first-break picks of a refractor (Laidley and Mills, 1986). The residual statics are added to the model-based statics when reporting the final static correction values. Notice that this inversion converges to a more accurate model when apriori information are incorporated such us uphole information.

The output of the refraction inversion program is a smooth velocity-depth model with the smoothness controlled by the user. Figure 3.8 shows the inversion result for Model 1. When compared with the true model in Figure 3.1, this model was able to capture the main features. The erroneous features seen at both ends of the model are the result of poor data coverage. Static corrections are calculated from this model, plus the automatically-calculated refraction residual statics. The residual statics are the time shifts that flatten the first break shown in panel (b). The seismic reference datum (SRD) was set at a depth of 100 m. The CDP gathers for Model 1 were corrected using these refraction statics, NMO corrected, and then stacked (Figure 3.9). The stack quality is reasonably good; however, it might have been more severely degraded if the data are dominated by higher frequency content; the dominant frequency here is 35 Hz. Again, as we have noticed earlier, shallow horizons suffer most from a bad set of statics. The artifacts in horizons 1 and 2 are

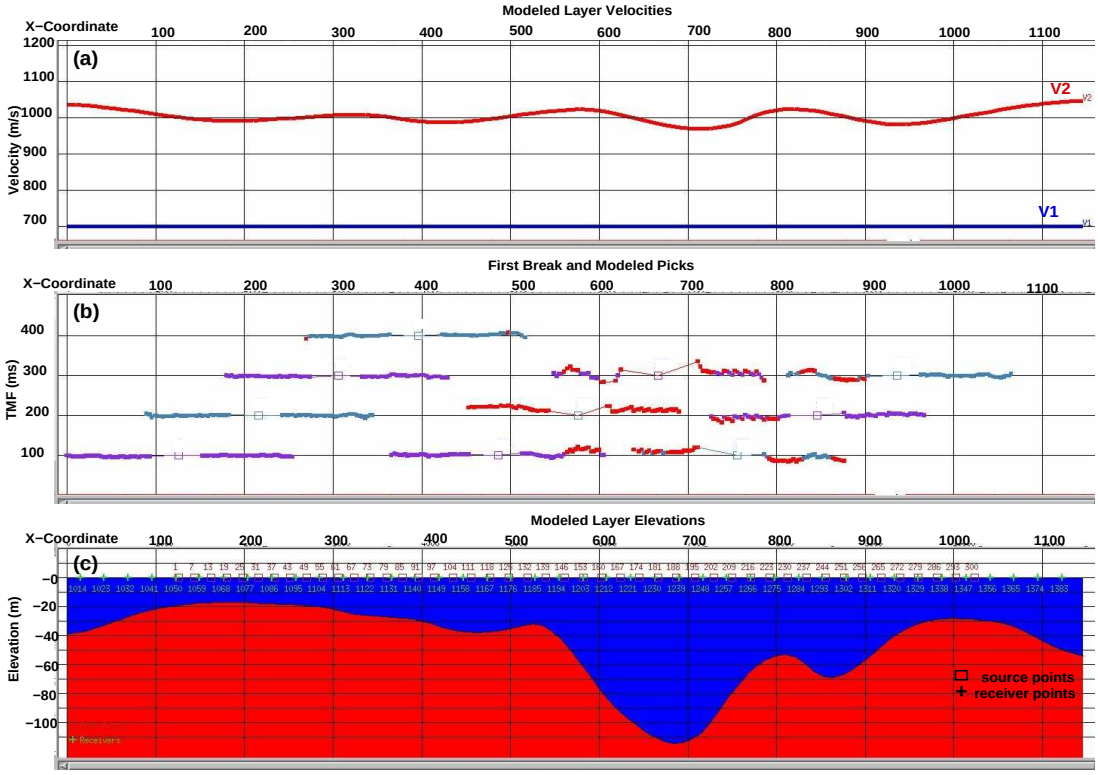

Figure 3.8. The output model from the refraction inversion software program. The two-layer depth model at (c) is a smooth version of the true Model1. The velocity of the top layer, 700 m/s was provided to the inversion program. The refractor velocity, V2, at figure (a) has a maximum error of 50 m/s, the true velocity is 1000 m/s. The middle figure (b) shows the first break after a applying the linear moveout for QC purpose. The different colors show different degrees of flatness.

located below the zone where dip of the LVL base is large. This indicates the inability of this algorithm to handle large dips, like most refraction inversion programs.

The same procedure was repeated for Model 2, where the base of the weathering layer now is more complicated than Model 1. A set of static values were derived using the GLI refraction-based method. These values were later used in the processing sequence to correct the CDP gathers and produce the

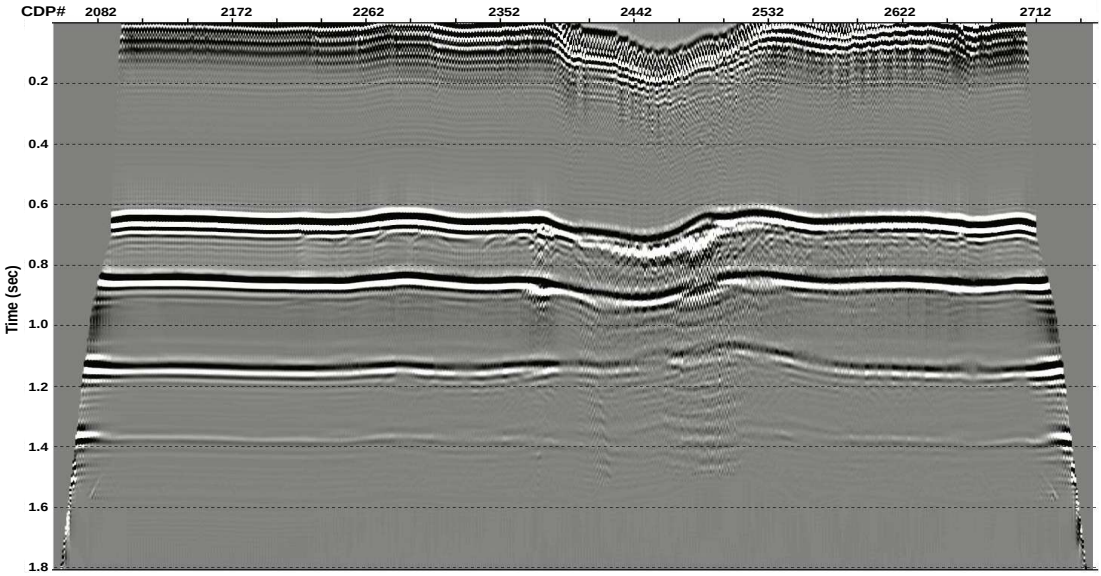

Figure 3.9. The initial stack of Model 1 prestack dataset after applying the refraction-based static values shown in Figure 3.8.

seismic stack given in Figure 3.10. Although the stack quality is acceptable, similar to Model 1, the image contains erroneous structures. Horizons 1 and 2 are not flat under the alluvium as they should be. Figure 3.11 compares the exact statics values with those derived from refraction inversion for Model 2. Although the two profiles correlate well with each other, the difference is very large under the thick part of the LVL. The large error in the statics created the erroneous features seen in the time stack. Although the exact weathering velocity V_0 was provided, the inverted long-wavelength statics were not accurate.

From these examples, one could conclude that for a simple earth model, such as Model 1 and Model 2, refraction-based methods produce an acceptable, but not an accurate, set of static correction values. The resultant earth model is only a smooth version of the actual model. The near-surface geology is

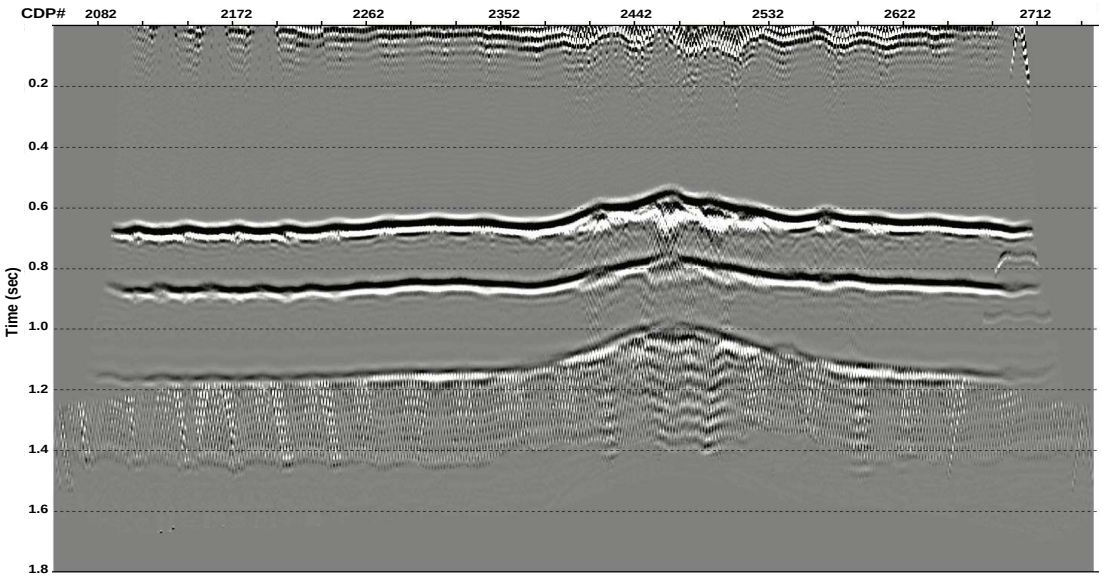

Figure 3.10. The initial stack for Model 2 after applying the refraction static values.

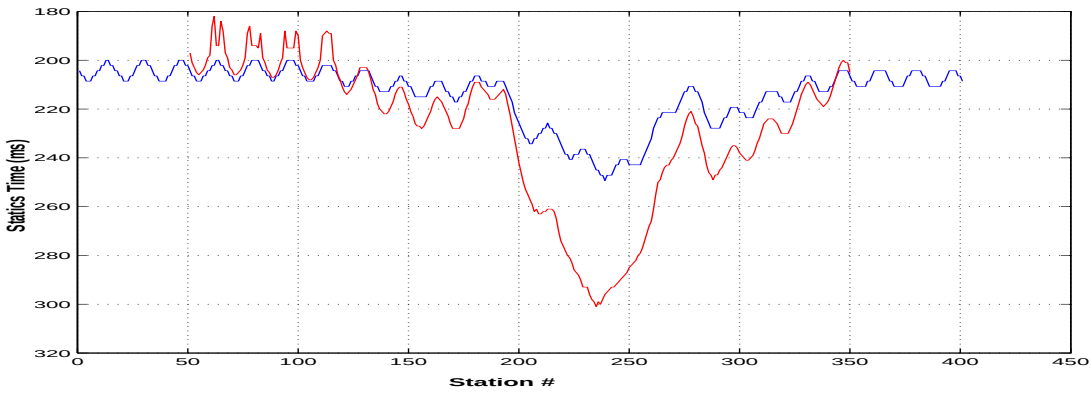

Figure 3.11. A comparison between the refraction-based statics (the red curve) and the exact statics (the blue curve). Notice that because of the acquisition geometry, the refraction statics curve does not cover the whole range.

usually more complicated than a simple stack of constant-velocity layers as was the case in the previous two models. There are four types of conditions with which any refraction-based algorithm is expected to have problems: very rapid variations in thickness and velocity, continuous vertical velocity variations, significant errors in refraction-time picking, and significant errors in the initial model (Hampson and Russel, 1984). In the previous models, there were no errors associated with refraction picking or the apriori weathering velocity V_0. Also, the layers had constant horizontal and vertical velocity distribution. Nevertheless, mild variability in weathering thickness caused appreciable error in the long-wavelength statics.

Uphole-based models are built by interpolating the depth and velocity at discrete points, usually at uphole locations. For economical reasons, sparse points are usually used to build the model, which usually results in a poor-horizontal-resolution model. Here I show that such a method easily fails to resolve simple anomalies in the constant-velocity LVL in Figure 3.1.

The model shown in the top of Figure 3.12 was built using few of the seed points used in the actual interface (Figure 3.1). In practice, this model is obtained if only a few sparse upholes are used in building the near-surface velocity model. In this stack, horizon 4 is as highly distorted as the surface stack (Figure 3.4). If an explorationist tries to use this section to map the target horizon (Horizon 4), the crest of the structure will be missed by about 3 km!

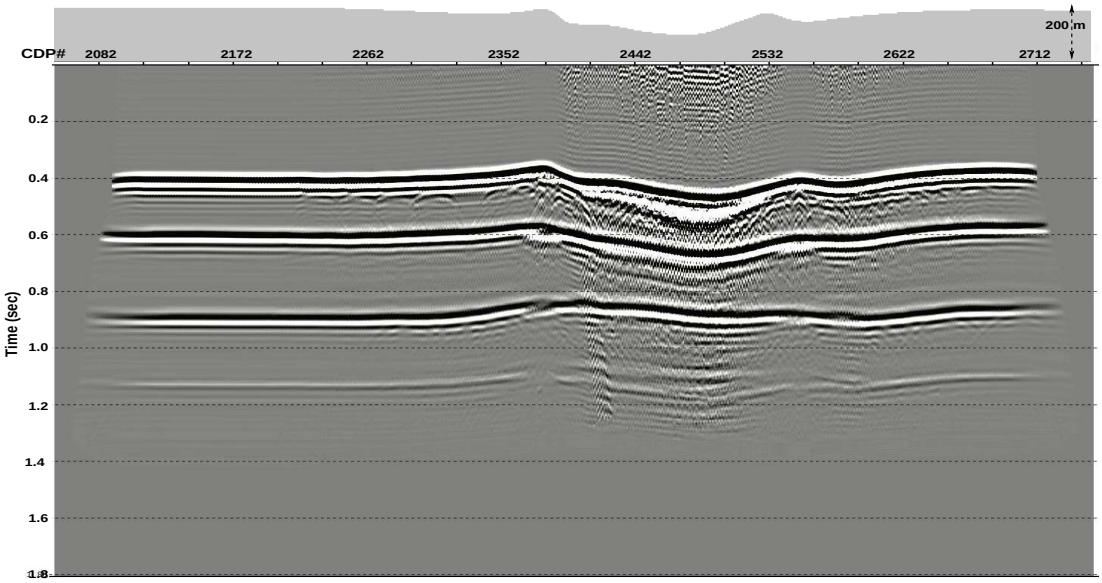

Figure 3.12. The initial stack of Model 1 using the near-surface model shown in the top plot. This model was built from the true Model 1 by using fewer points to define the base of the LVL. This procedure simulates drilling few discrete upholes to build the model.

3.0.6 Error analysis:

How fine should the near-surface be sampled to be able to resolve the anomalies? Also, given an error in the near-surface model, how does this error propagate to an error at the reservoir level? The numeric model shown in Figure 3.13 addresses this issue. In this model, both velocity and thickness of the base of the LVL vary laterally. The frequency spectrum of the vertical-one-way-time profile, Figure 3.14, shows that the minimum wavelength is about 140 m, while the maximum wavelength is about 9 km. The long wavelength static components display the highest amplitude. Thus the problem persists even if the short-wavelength component is determined through residual statics analysis.

According to sampling theory, at least two samples per wavelength are needed to accurately represent an analytical signal. Therefore, to be able to reproduce the true model using few upholes, an uphole needs to be drilled every 70 m. For obvious economical reasons, a larger sampling interval is usually implemented in practice, with an uphole drilled every about 10 km. Such a coarse sampling will introduce an error in the interpolated model. There are two types of errors: the sampling error, or aliasing, and the interpolation error. The former error is small and can be ignored here. The total error in the datum statics can be quantified using the Root-Mean-Square-Error (RMSE) of the error function, i.e, the difference between the exact profile and the same profile sampled at a coarser interval.

The plot in Figure 3.15 is the RMSE for a number of models with different sampling interval. The x-axis is the ratio of the sampling interval to the minimum wavelength in the original signal, which is 140 m in this case. Beyond the ratio of 1/2, required by the theory, the error increases rapidly. This was observed in this model and many other models that are not shown here whose minimum wavelength is larger or smaller than this model.

The frequency spectrum of some of these error functions are shown in Figure 3.16. Each vertically-shifted curve is the wavelength spectrum for a particular sampling δ, which is the sampling interval relative to half of the minimum wavelength, 70 m in this case. The x-axis is the ratio of the wavelength to half the minimum wavelength. One might expect that, for $\delta = 8$, for example, the error component would be zero for wavelength ratio greater than 8. The figure does not show that; in fact we see non-zero components even for relatively small sampling such as $\delta = 4$. For a particular sampling ,

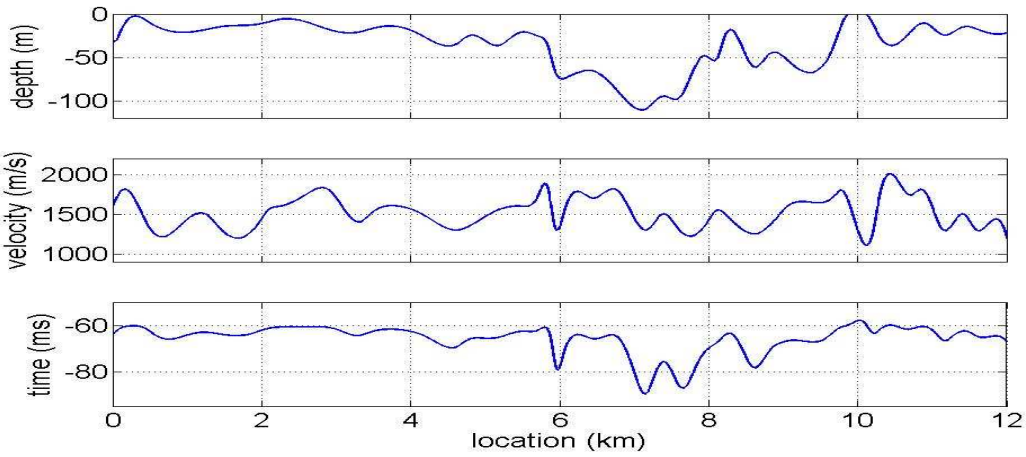

Figure 3.13. This numerical model is used to study the errors induced by using fewer-than-needed upholes to model the near-surface accurately. This model is similar to Model 4, but without the top 5-m layer.

$\delta = 8$ for example, the long-wavelength components of the profile are sampled accurately. The smaller wavelength components, however, get aliased into the long-wavelength components, which make them non-zero.

Since our seismic targets are usually of long wavelength, this analysis shows the importance of resolving the relatively small near-surface anomalies to be able to image the subsurface targets accurately.

Combining the above two methods, refraction-based and uphole-based, a more accurate model can be built. This is obtained by using the velocity and/or depth of the refractor at the uphole locations as apriori information to refraction modeling (Cox, 1999).

3.1 Model 4 Analysis

From the above analysis, one can come to a conclusion that even for relatively simple constant-velocity models, the existing methods fail to produce

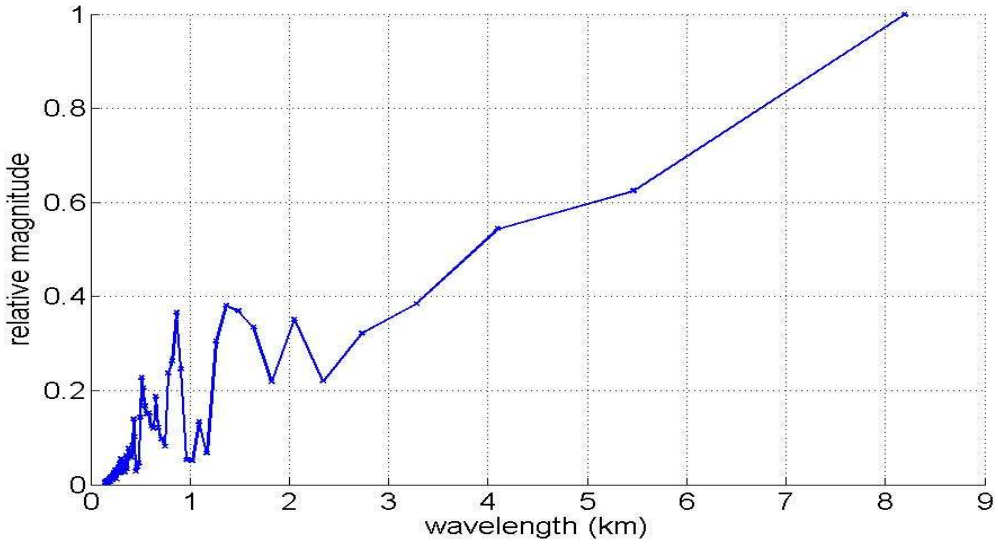

Figure 3.14. This is the travel-time shown in Figure 3.13, but in wavelength domain. At a wavelength of about 140 m, the magnitude is almost zero. So, the minimum wavelength in this model is about 140 m.

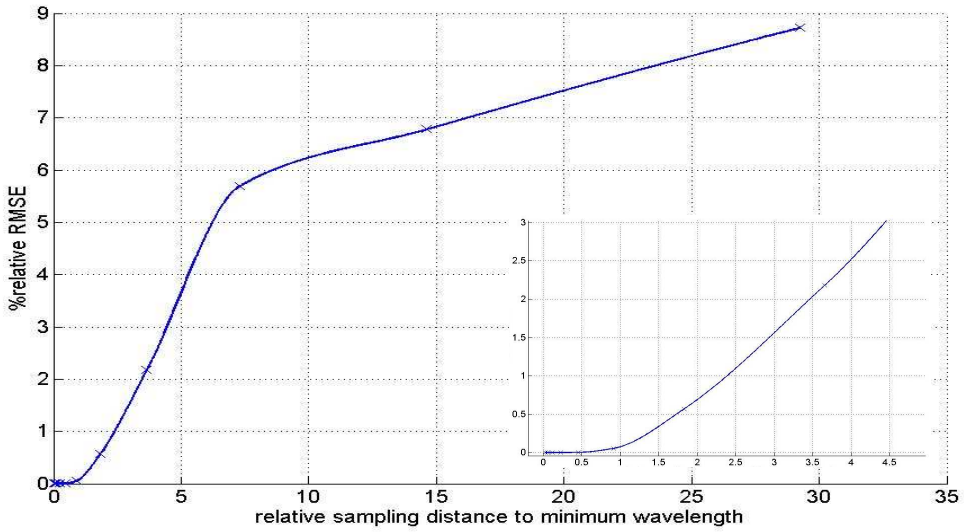

Figure 3.15. This is the Root-Mean-Square-Error (RMSE) of the vertical-time down to the base of the LVL as a function of relative sampling to the minimum wavelength of 140 m. The plot in the inner frame is a zoom around ratio of 1.

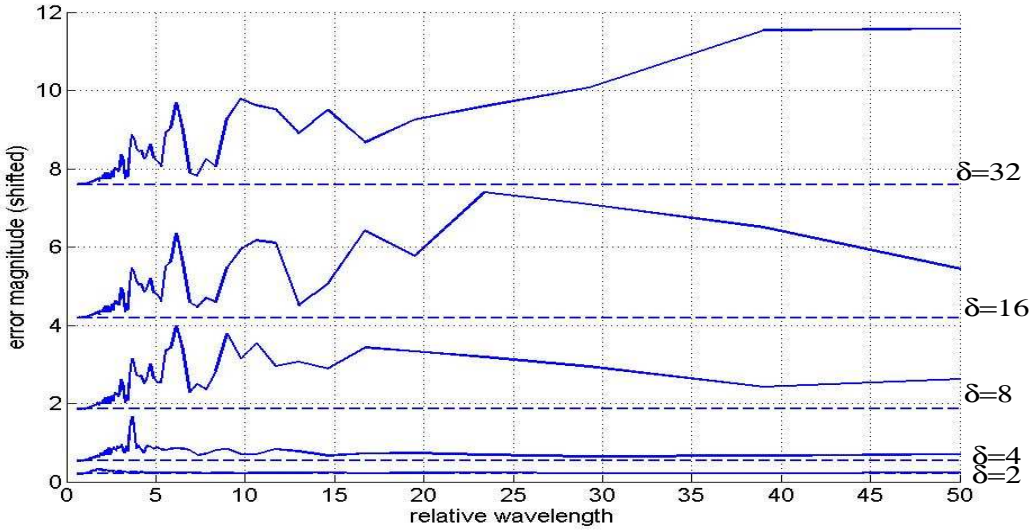

Figure 3.16. The wavelength spectrum of some error functions, vertically-shifted for easy comparison. The δ is the model sampling interval relative to 70 m, which is half the minimum wavelength in the exact model. In each curve, the magnitude of the error function is plotted against the relative wavelength range $1 - 50$.

an accurate model with enough lateral resolution. To get the desired model, I proposed earlier acquiring high-resolution seismic data as a mean to build the model. The characteristics, dynamics and kinematics, of such data are used in the inversion process to obtain a near-surface velocity model. The analysis can utilize different modes: direct, reflection, refraction, or surface waves.

In this section, I implement this methodology using numerical modeling. However, I consider a more realistic model than those studied above. The new model, Model 4, is a modification of Model 2 after introducing a laterally-varying weathering velocity. The variations are smooth and in the horizontal direction only. Moreover, a 5-meter low-velocity layer is added to the top of the model. The model is shown in Figure 3.17. Notice that the deep part of Model 4 is similar to Model 1 (Figure 3.1); both have four layers. The effect of the near-surface on the seismic stack is shown in the surface stack shown in Figure 3.18. Horizons 1 and 2 are not flat, but dipping toward the deep part of the wadi. The coherency of these horizons is week compared to horizon 3. The crest of the structure is shifted from the true location by about 3 km.

3.1.1 Applying Refraction Method

Clearly, trying to reconstruct the weathering layer thickness and velocity of this model from discrete points is almost impossible unless we drill a hole every 70 m, which means we need to drill 172 upholes! Next, we try to compute the static correction values using a refraction analysis method. Here we are going to use an GLI-based refraction method. In this technique, the refracted-wave arrival picks are first aligned using cross-correlation. This process ensures a more accurate linear velocity estimation. Depth and velocity of the refractor

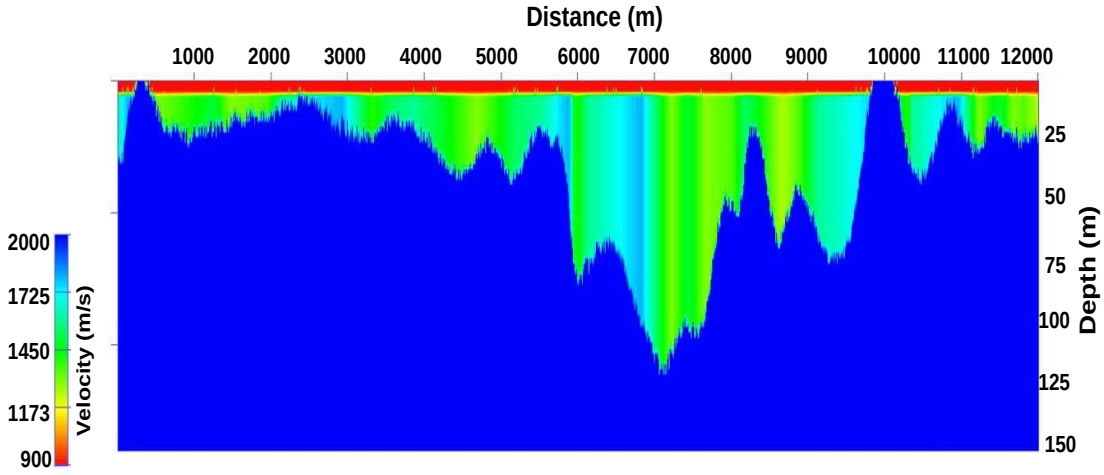

Figure 3.17. The near-surface of Model 4. To make the model more realistic, the velocity varies laterally with a rough base. A thin, 5-meter low-velocity, 900 m/s, layer is added to the top of the model.

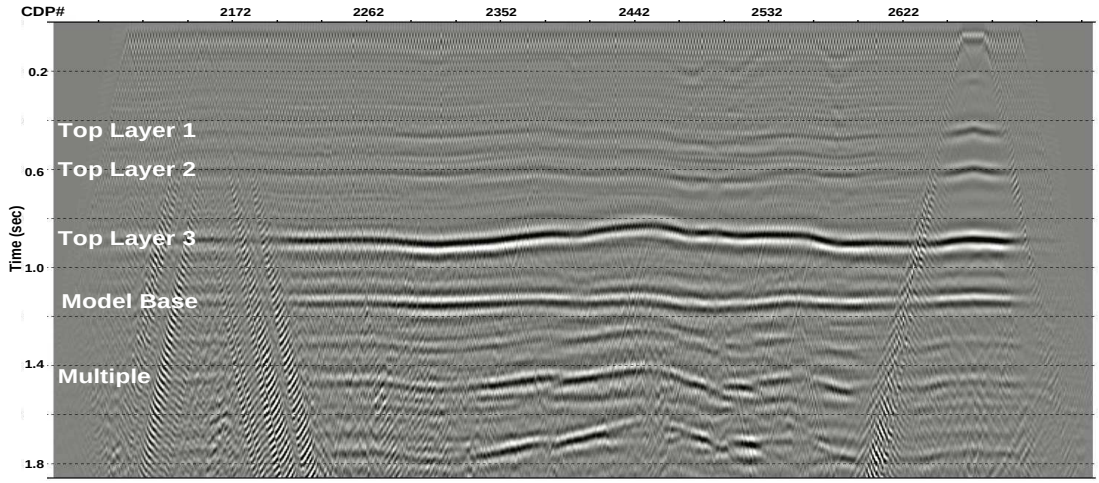

Figure 3.18. A brute surface stack of the conventional data over Model 4.

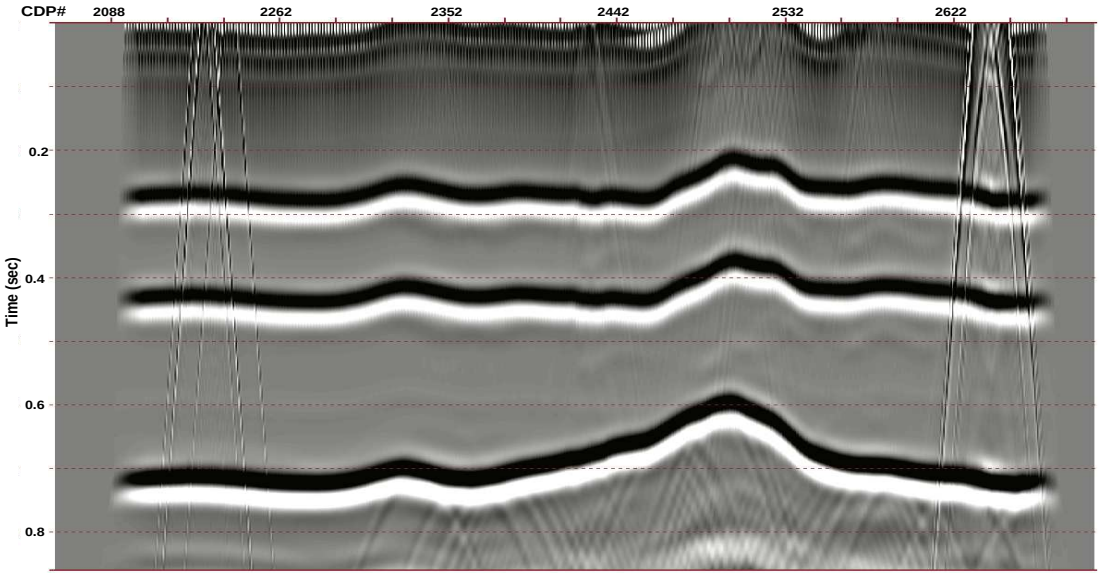

Figure 3.19. The initial stack of the data over Model 4. The static correction values were computed using the Hampson and Russel GLI-based refraction method. The datum is 180 m below the surface.

are inverted for using the aligned refraction times and the apriori weathering velocity V_0. Figure 3.19 shows the stack obtained after using the refraction-based statics. Notice that the stack response as well as the target geometry are similar to that obtained for the constant-velocity Model 2, Figure 3.10. The stack coherency is very good because of the refraction-residual statics discussed above. The geometry of all three horizons, however, are erroneous. In fact, such a stack gives the impression that this structure is only a static anomaly.

3.1.2 Applying the New Methodology on Model 4

My proposed methodology is based on utilizing a separate high-resolution seismic dataset. The velocity model is the outcome of an inversion process

which uses such data. The method assumes that the resolution of the output model is proportional to the resolution of the data. So, as a preliminary step, we need to generate the necessary synthetic seismic data. Table 3.1 shows the modeling parameters for the high-resolution data. The small group interval ensures that the high spatial frequencies are not aliased. A coarser sampling interval might be sufficient, however, depending on near-surface velocities.

The high-frequency source, however, dos not ensure the temporal-resolution unless the near-surface lithology has a high quality factor Q. Figure 3.20 shows a sample shot gather from the modeled high-resolution dataset. This gather was taken from the location at 5370 m, the same location where the conventional shot gather shown in Figure 3.3 was acquired. Notice that I have simplified the model here for more accurate reflection picking and velocity analysis. The base of the LVL was smoothed to minimize scattering. In reality, we will have the complications of the very near-surface direct waves, surface waves, and the near-field effects. Along the 12-km line, six thousand shot gathers were generated using source and receiver intervals of 4 and 2 meters, respectively. Note that because we focus on the near-surface, layers 2, 3, and 4 are not included in this model.

Velocity Analysis: In conventional data processing, the velocity is estimated at discrete points along the line. The final velocity model is built by interpolating between these points. But, for our data, we utilize each of the 24000 CDP gathers to pick a velocity function to ensure the velocity-model accuracy. The process, however, is a time-consuming task. It can be accomplished more easily by using horizon-based velocity analysis (HVA). Here, a time horizon is first picked from the stack. The stacking coherency for a range

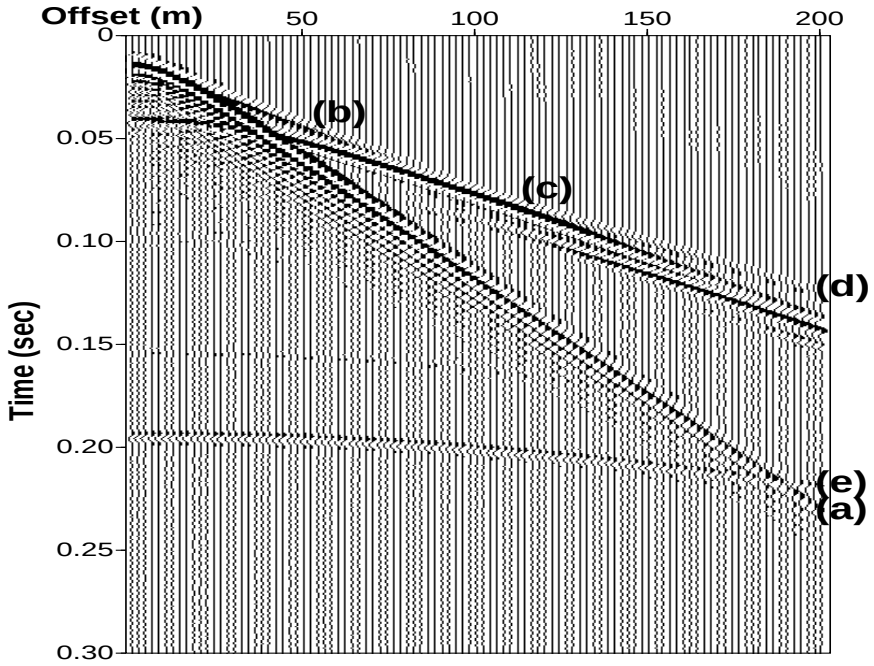

Figure 3.20. A sample shot gather from the high-resolution dataset. The receiver interval is 2 m, while the source interval is 4 m. This gather was taken from the same location as the conventional shot gather shown in Figure 3.3. The events (a) is the VLVL reflection, (b) is the VLVL refraction, (c) is the LVL reflection, (d) is the LVL refraction, and (e) is the base-of-model reflection.

of velocities is computed and contoured for all the CDPs. From an HVA panel like the one shown in Figure 3.21, we can pick the stacking velocity associated with that horizon.

This technique works well if we have a continuous horizon along the line. Figure 3.22 shows the velocity model developed, based on the HVA stacking velocity, in pink, while the exact model is shown in blue. The exact velocity in this figure is the effective average velocity calculated from the total depth and the total vertical time to the base of the LVL. Notice that our model included the thin 5-m layer, therefore the estimated velocity will be the rms velocity V_{rms} of this layer and the LVL layer. The rms velocity is usually larger than the average velocity at a particular depth. That is why there is a bias in the estimated velocity profile toward a generally lower velocity. In general, the main features of the model were resolved except where the weathering layer thins out, and where there is no velocity contrast with the subweathering layer. The depth profile is calculated from the time picks from the stack and the picked velocity. Table 3.2 shows statistical error analysis for this model. Although the relative RMS error in velocity and depth profiles are larger than 8%, the error in time is only 2.3%. If we compare this number with the plot in Figure 3.15, we can conclude that this method is able to resolve anomalies as small as 3 times the shortest wavelength, or about 420 m. This number is related to the size of the Fresnel zone, which in turn is related to depth and velocity of the weathering layer.

Besides the medium velocity, the stacking velocity also depends on the dip of the reflector, the near-surface variations, and the mute function. The dip-dependency can be dealt with using dip-moveout (DMO) velocity analysis.

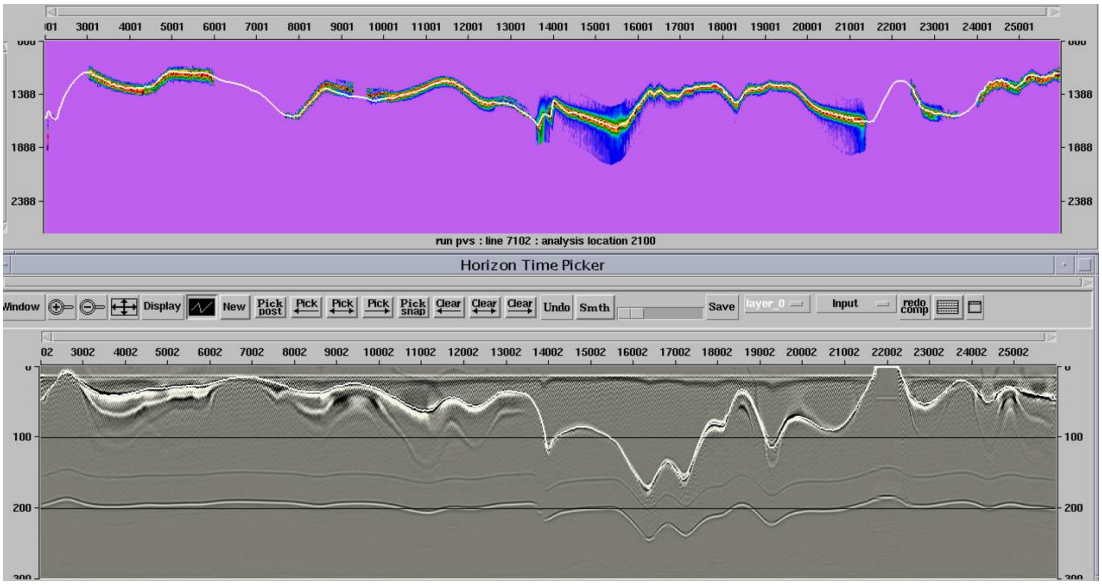

Figure 3.21. A horizon-based velocity analysis panel. The reflection from the weathering layer is clear and the velocity analysis is easy due to the absence of noise.

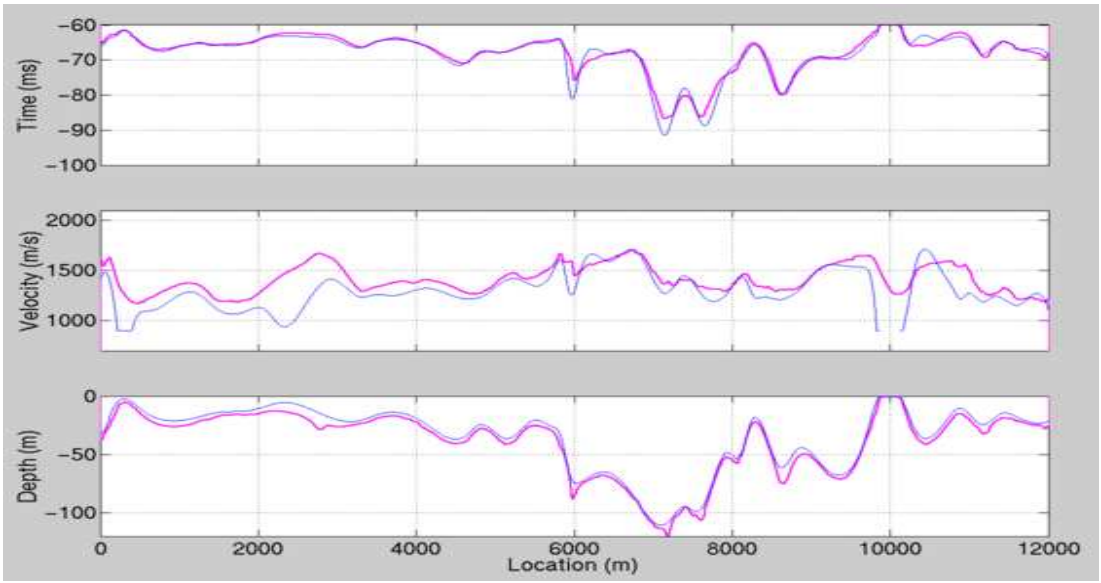

Figure 3.22. A velocity-depth model estimated from the horizon-based velocity analysis (the pink profiles) plotted with the exact model (the blue profiles). In zones where there is no strong reflected signal or the LVL outcrops to the surface, the two curves diverge. Also, the picked velocity is the rms velocity, while the exact velocity is the average velocity.

Attribute	Min. Error	Max. Error	Mean Error	RMS	% RMS
velocity(m/s)	0.026944	1418.492744	93.247435	119.585831	8.891571
depth(meter)	0.001119	30.134487	4.270980	4.882684	10.512790
time(ms)	0.00016	11.158	0.939	1.591274	2.307403

Table 3.2. statistical error analysis of the model obtained from conventional velocity analysis.

Residual statics help in removing the effects of the high-frequency velocity variations. Mute functions help produce the best stack and improve the result of the velocity-picking process. The stacking velocities must be converted to interval velocities using Dix equations, which were derived for usually simple models (Dix, 1955). For all these reasons, tomography inversion is alternatively used to estimate the velocity-depth model directly from the prestack data. This method, however, is more time-consuming than the conventional velocity analysis because of the need to pick the prestack refraction and/or reflection time arrivals. Also, in certain cases, it is difficult to distinguish reflection hyperbolic events in the prestack gathers.

Reflection Tomography: Here, I use reflection times from the base of the weathering LVL layer as an input to a commercial horizon-based reflection-tomography package (CAT3D). The peak of the reflected wavelet is picked for all or part of the shot gathers. The program uses a raytracing program which has two options: straight raytracing or the more accurate curved raytracing. The software has several algorithms for the travel-time inversion; for example, Simultaneous Iterative Reconstruction Tomography (SIRT) and the Algebraic Reconstruction Tomography (ART). Figure 3.23 shows the exact model to-

Attribute	Min. Error	Max. Error	Mean Error	RMS	% RMS
velocity(m/s)	0.004909	481.157960	94.869919	129.187305	9.605469
depth(meter)	0.000772	28.915252	3.938588	5.063904	10.902970
time(ms)	0.000116	5.416901	1.014183	1.423707	2.064425

Table 3.3. Statistical error analysis of the model obtained from reflection-tomography inversion.

gether with the tomographic inversion result. The exact velocity in this figure is the effective average velocity calculated from the total depth and the total vertical time to the base of the LVL. The main features of the model were reasonably resolved in depth and velocity. Like the conventional velocity analysis, the method fails where the time picking is inaccurate; either because the reflector is very shallow or there is no velocity contrast. Table 3.4 shows more clearly that the accuracy obtained here is similar to that obtained from the conventional velocity analysis.

The tomography procedure was repeated using less data points by decimating the number of shot and receiver stations. Similar results were obtained even by using every tenth shot points, or every fifth receiver station. Someone might predict, however, that picking accurate reflection times after decimation would be more difficult if not impossible. Also, to confirm stability of the solution, the inversion was repeated using different initial models. The final models were found to be similar, which leads to high confidence in the output model.

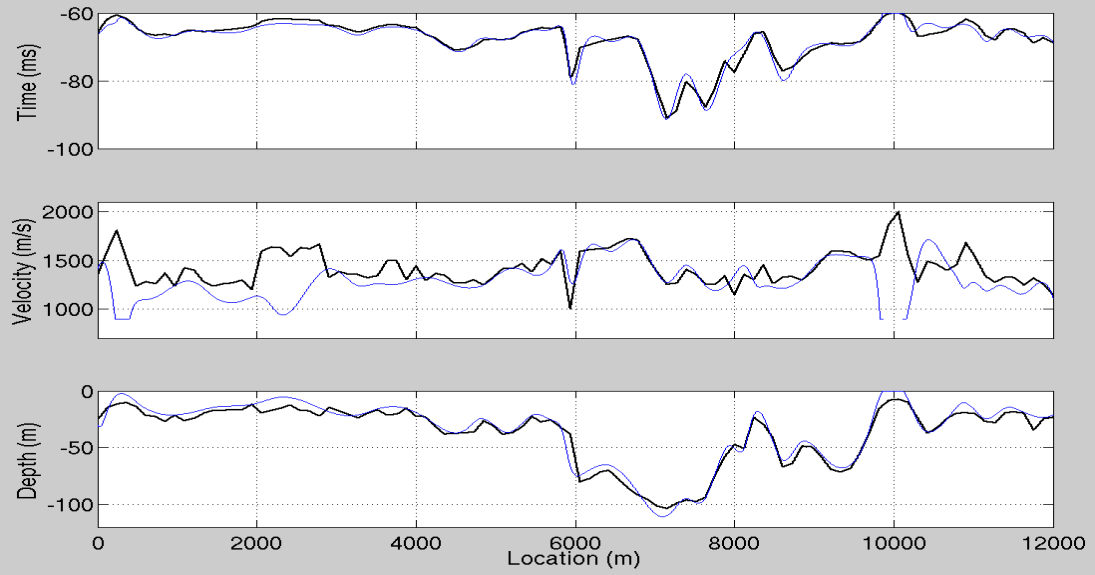

Figure 3.23. A velocity model which was obtained from reflection-tomography inversion of the high-resolution data. The blue profiles are for the exact model, while the black profiles are for the estimated model.

3.1.3 Applying the New Methodology on Simplified Model 4

The complications in Model 4; namely, the top 5-m layer and the relatively short offset, 200 m, might have affected the accuracy of the output velocity model. To investigate this more, I have created a new dataset with source and receiver intervals of 2 and 10 m, respectively. With a simulated 50-channel cable, the maximum attainable offset is 500 m. Figure 3.24 is one shot gather from that dataset taken from the same location as the gather in Figure 3.20. This dataset will be used later in testing reflection tomography.

Velocity Analysis: The main purpose of acquiring such dataset is to use it as a means to develop a near-surface velocity model. The most conventional and robust method to obtain velocity information is through stacking

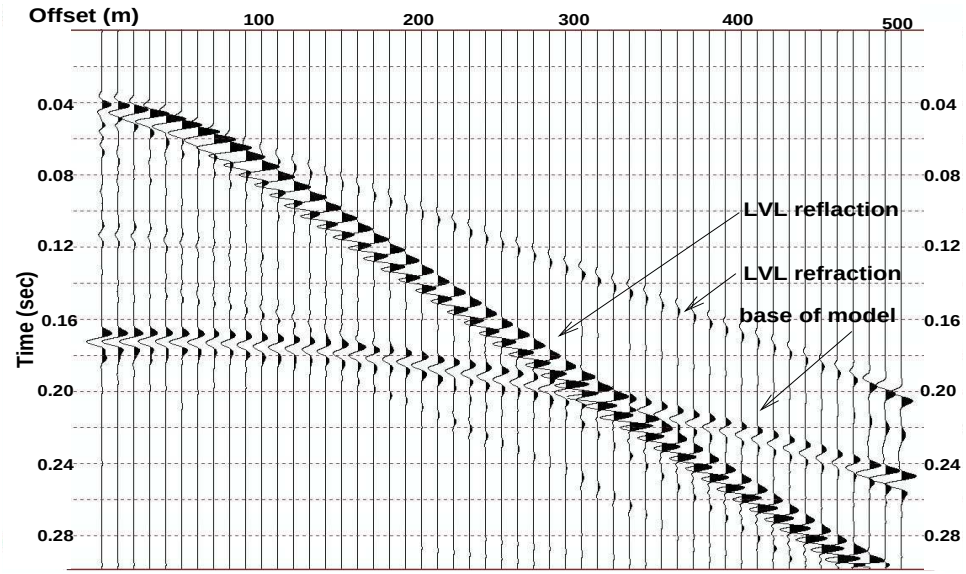

Figure 3.24. A sample shot gather from a second high-resolution dataset. The receiver interval in this dataset is 10 m. This gather was taken from the same location as the conventional shot gather shown in Figure 3.3.

velocity analysis. The stacking velocity, V_{stk}, is an estimation to the root-mean-square velocity, or V_{rms}. The V_{rms} velocity is converted to interval velocity, or V_i, through some equation such as Dix equation (Dix, 1955). The stacking velocity analysis program is an interactive program in which the analyst, usually manually, picks the velocity that produces the best stack. Of course, this estimation is influenced be the noise in the data as well as the field statics. For this reason, the data should be preprocessed and filtered before the analysis. As for the field statics, within the small spread-length, the near-surface does not drastically change. But, we also could estimate and apply residual statics to improve on data stacking coherency. In fact, it is not uncommon for a processing sequence to include two cycles of velocity and residual estimation.

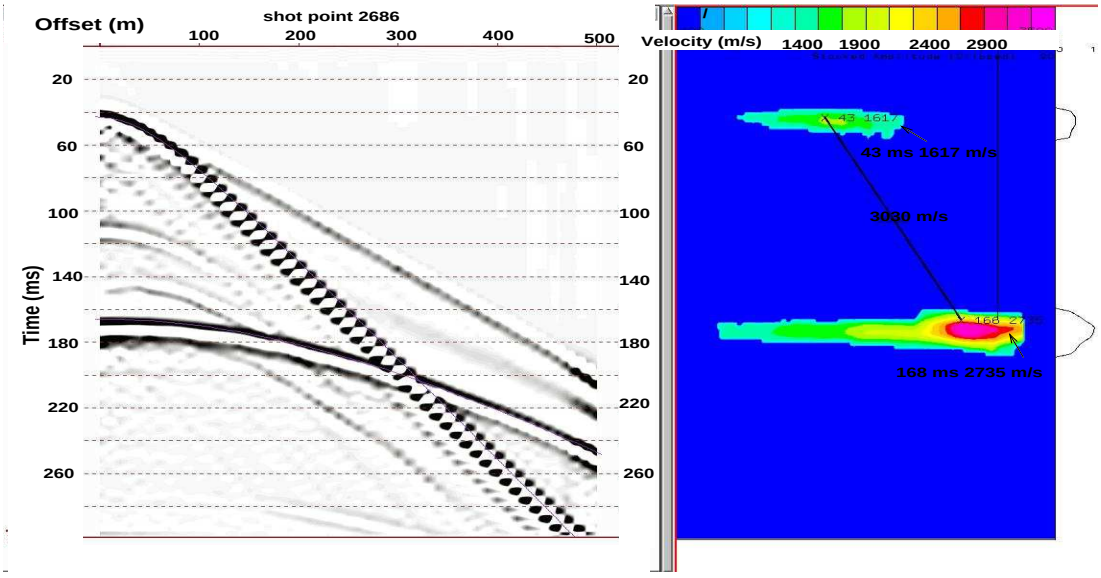

Figure 3.25. A velocity-analysis panel for the gather shown in Figure 3.24. It shows the reflection from the top of the weathering layer and the base of the model. The velocity of the LVL is 1617 m/s, off by 17 m/s, while the velocity of the base of the model 3030 m/s, off by 30 m/s. Note that the true velocity below the weathering layer is 3000 m/s.

For this synthetic dataset, the preprocessing is not necessary and we will assume that the data is ready for velocity estimation. The velocity-analysis panel shown in Figure 3.25, shows that the stacking velocity from top of the weathering layer can be picked with confidence. In fact the picked velocity, about 1600 m/s, is very close to that shown in the model in Figure 3.13. Below the weathering layer, the interval velocity is set to 3000 m/s. This is different from the velocity of the second layer in Model 1 or Model 4 to avoid FD modeling noise. In the panel, the interval velocity of this layer is only off by 30 m/s.

Attribute	Min. Error	Max. Error	Mean Error	RMS	% RMS
velocity(m/s)	0.004383	220.223328	31.517699	42.531151	2.801902
depth(meter)	0.001022	12.820413	3.803467	4.575164	9.846760
time(ms)	0.000426	9.952496	2.505819	2.981861	9.582545

Table 3.4. Statistical error analysis of the model obtained from reflection-tomography inversion shown in Figure 3.26.

Reflection Tomography: The reflection times from the gathers were also picked and used in reflection tomography. The output model is shown in Figure 3.26. The output model clearly is a better match to the exact model than that shown in Figure 3.23. The errors shown in Table 3.4 confirm this. The velocities in this model are three times more accurate than the previous model. The vertical time, however, is unexpectedly less accurate.

Model non-uniqueness is a major problem in the reflection-tomography technique. However, the larger redundancy in the data, a gather every 2 m, and the large aperture of 500 m helped in obtaining a better constrained solution. The velocity invariability in depth, within a layer, is an ideal model for reflection tomography.

3.1.4 Using the Velocity Model in Conventional Data Processing

Once we obtained the model from the auxiliary high-resolution seismic data, it was used to process the conventional seismic either through statics correction or gathers redatuming.

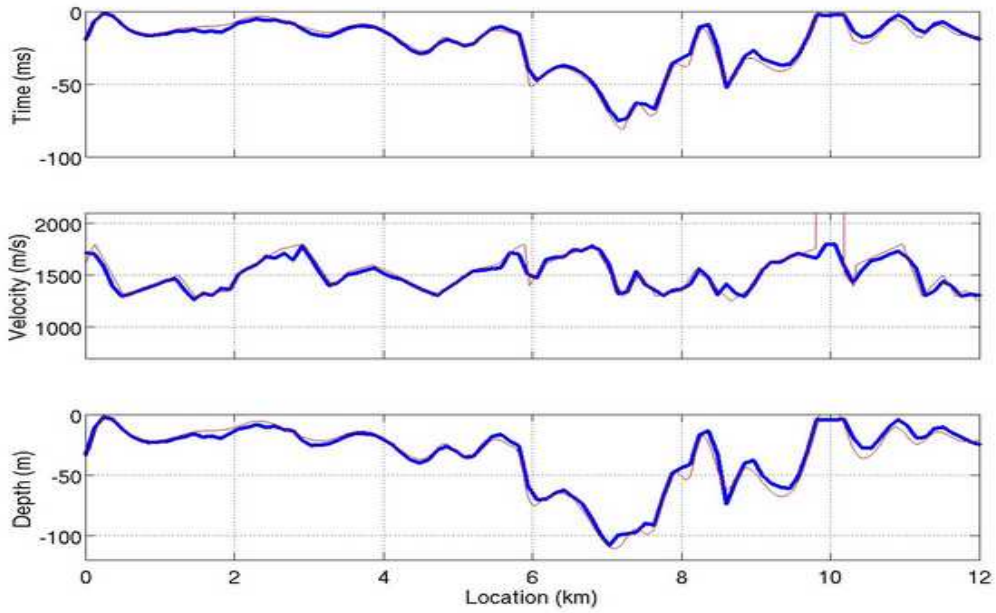

Figure 3.26. A velocity model obtained from reflection-tomography inversion of the high-resolution data. The blue profiles are for the exact model, while the black profiles are for the estimated model. Source and receiver intervals for this dataset are 2 and 10 m, respectively.

Statics Correction As we have discussed earlier, the simplest correction method is the robust statics correction. The vertical travel time from the surface to a flat datum, usually below the weathering layer, is calculated and applied for every source and receiver location. Using the model in Figure 3.23, the datum is assumed to be a flat surface, 120 m below the surface. The subweathering velocity used here is 3000 m/s.

The bottom panel in Figure 3.27 shows the stack after applying the statics corrections from the model in Figure 3.23. From the stack quality and reflectors geometry, we can conclude that the statics have corrected most of the erroneous artifacts introduced by the complex near-surface. The wavelength of the remaining oscillations in the time horizons is about 500 m. The smallest wavelength that was resolved in model 3.23 and 3.22 is about 420 m. Therefore, one possible reason for these oscillations is the accuracy of the model. Another possible reason is the inaccuracy of the correction technique. The weathering layer in the middle is thick with a small velocity difference between the weathering and the subweathering layer. These conditions cause the violations of the vertical-ray assumption, which is the basis behind the statics correction technique. To determine the exact reason, I have calculated and applied the exact statics values from the true model and applied it to the data. The resultant stack is shown in the top panel of Figure 3.27. Clearly, the horizons, still, look oscillatory in certain parts of the line; in fact, they look more oscillatory than the tomography-based stack. This can be attributed to the smoothness of the inversion-based statics values.

Datuming A more accurate way to correct for the near-surface is using wavefield extrapolation or redatuming. In such techniques, the prestack data

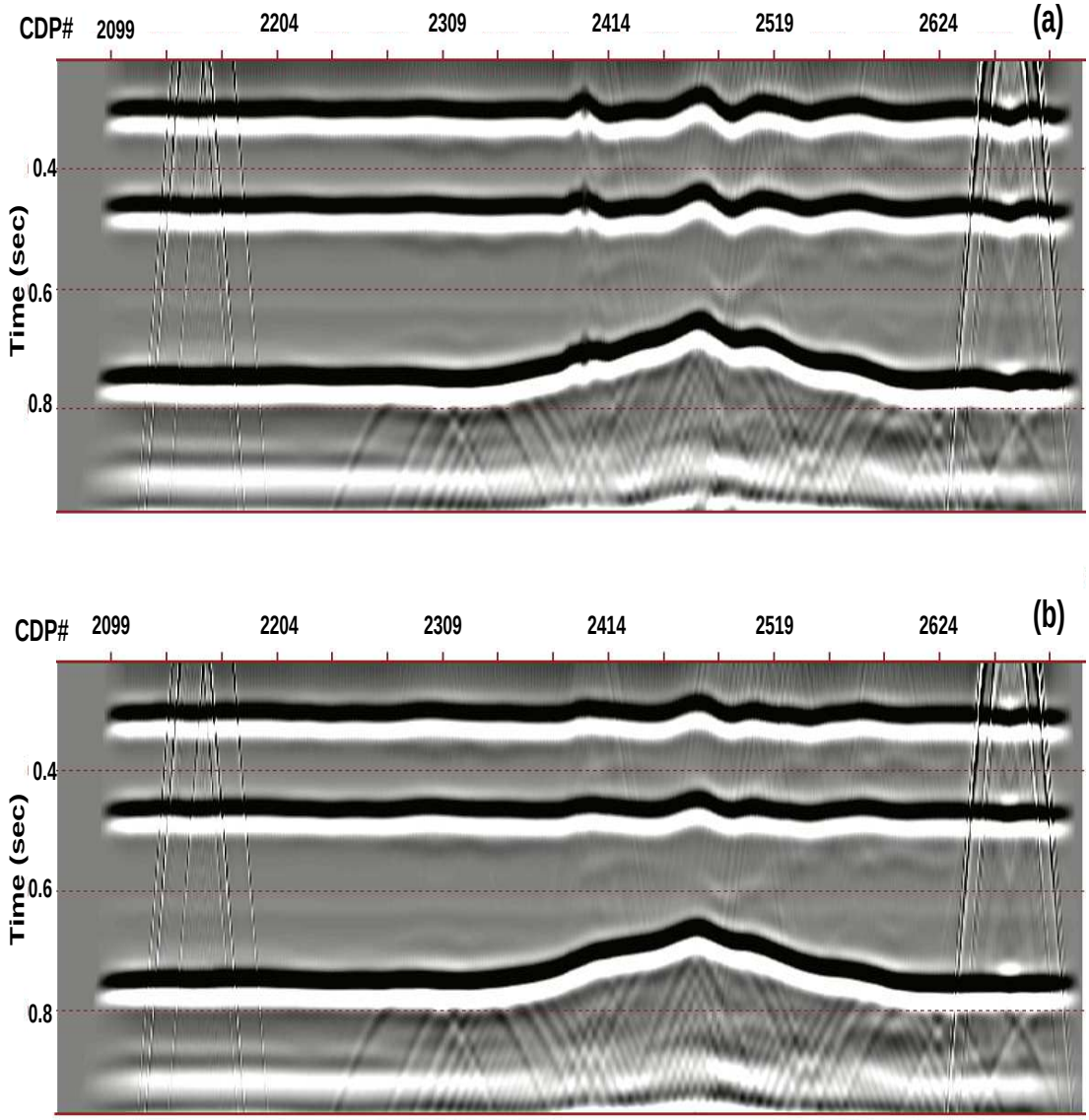

Figure 3.27. The initial stacks after applying the exact statics (top panel) and those estimated from the model in Figure 3.23 (bottom panel).

are downward continued to a ,usually, flat datum below the surface. Generally, there are two different classes of redatuming techniques: ray-based techniques and Wave-Equation-based (WE). The WE technique produce more focused output gathers because it takes into account multi-pathing. For this reason, it is more accurate than the ray-based techniques. However, they are more sensitive to the input velocity model. Here I use an WE-based SU redatuming program to redatum the data to a flat datum 120 m below the surface (CWP, 2005). Figure 3.28 shows the stack of the data after redatuming. The tomography-based model is used in the bottom section, while the exact model is used in the top section. There are few differences between the two sections, which indicate the accuracy of the tomography-based model. The differences in the velocity model were so minor that it did not affect the redatuming result. The horizons in both sections are coherent and have the correct geometry. The flat horizon at 1 sec is the surface multiple from the second reflector. Notice how flat this multiple is; unlike the sections in Figure 3.27.

3.1.5 Summary

In the first part of this chapter, three constant-velocity near-surface models were used to demonstrate the importance of an accurate near-surface velocity model in conventional seismic data processing. The normal refraction and uphole-based methods have failed for these relatively simple methods. From the error analysis, the required accuracy dictate using a more accurate method.

In the second part, the laterally-varying velocity Model 4 was used to implement the proposed new method. This modeling shows that high-resolution

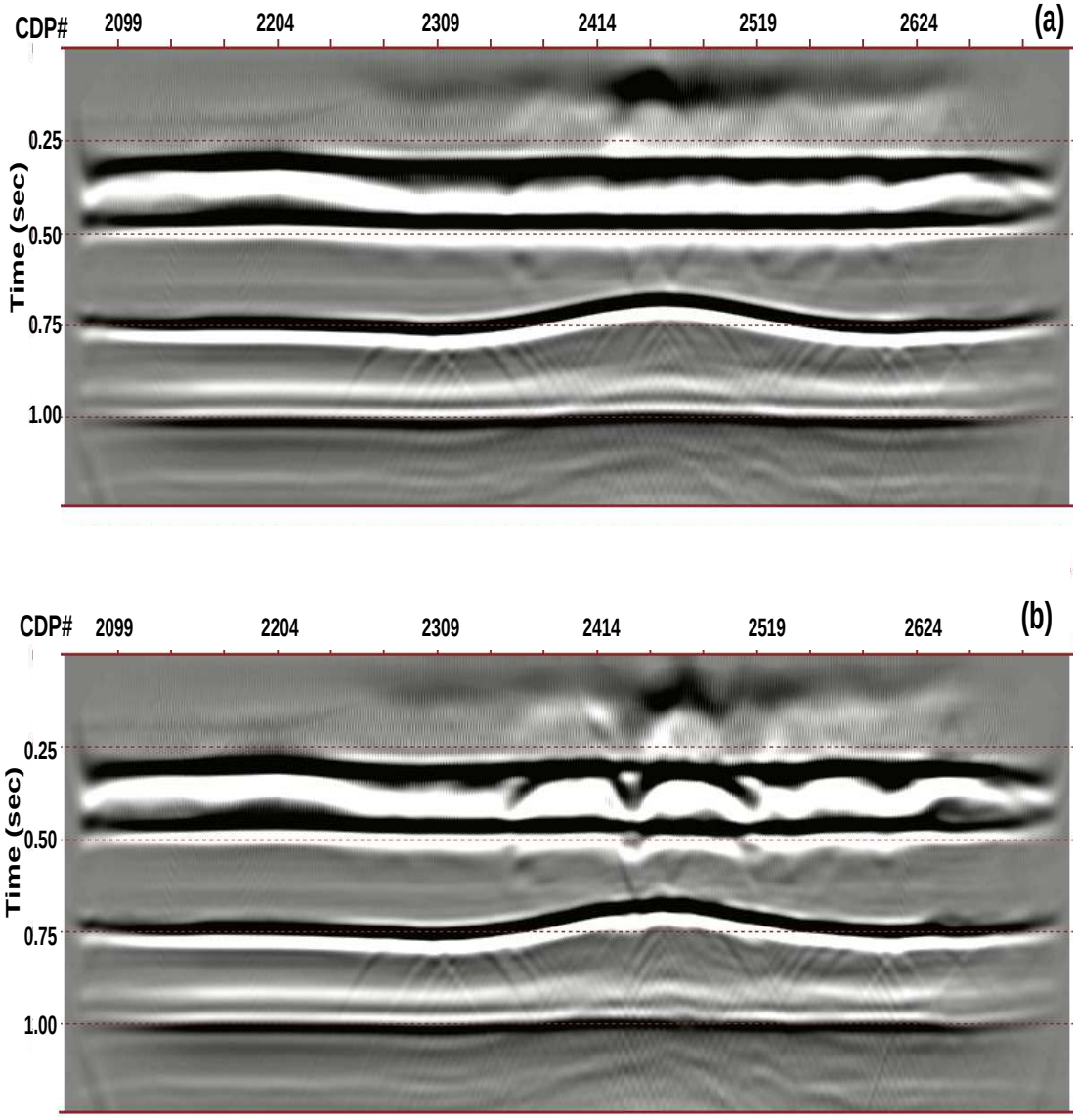

Figure 3.28. The initial stack after Wave-Equation redatuming to a flat datum below the complex near-surface layer. The tomography-based velocity model, Figure 3.23, was used in the bottom panel, while the exact model was used in the top panel.

data can provide us with the velocity information that we need to correct conventional seismic data.

In the velocity analysis, two techniques were used: the conventional coherency analysis and the reflection tomography. Although reflection-based methods might be accurate because of the deeper depth of investigation. Turning-ray tomography can help improve the model at shallow depth. The joint inversion of multi-modes, such as reflection and refraction, has also been found to enhance the accuracy of the model by other researchers (MacMachan, 1992)

Chapter 4

FIELD DATA

4.1 Objective

In the last chapter, it was shown numerically how high-resolution seismic data are utilized to build a near-surface velocity model. This model then is used as an input to a conventional data processing sequence. Such a model has a better spatial resolution and allows improved imaging of deeper layers. In this chapter, these results are evaluated using field datasets. High-resolution near-surface models are constructed for three 2D lines using high-resolution seismic. Two lines, Zahar1 and Zahar2, are from the eastern Coastal Region of Saudi Arabia. The third line, Dilam1, is from the Central Region of Saudi Arabia.

The conventional 2D line, Zahar1, was originally acquired using small spatial sampling and was used as an approximation to the true shallow high-resolution data similar to that used in the previous chapter. As for the other two lines, Zahar2 and Dilam1, two high-solution datasets were specially acquired for this dissertation.

4.2 Line Zahar1

Line Zahar1 is a conventional 2D seismic line which was acquired in the Eastern Province of Saudi Arabia. The terrain is a gravel plain covered sparsely

Table 4.1. Line Zahar1 acquisition parameters.

source and receiver intervals	5 m
number of channels	3500
spread type	symmetric
CDP interval	2.5 m
maximum fold	1500
source type	sweep 10-180 Hz
sampling interval	2 ms

by low-relief sand dunes. The parameters listed in table 4.1 were used in acquiring this dataset. The line was acquired in the year 2000 for the purpose of testing. The conventional source and receiver intervals used in Saudi Arabia are between 20 and 30 m. In this line a smaller spatial sampling (5 m) was used to examine the benefits of using the same high-fidelity data to estimate the residual statics and image deep targets at the same time.

The source type used for this dataset was not of a high-frequency type. Yet this dataset was a good approximation to the true shallow-seismic dataset needed to model the very near-surface.

4.2.1 Local Near-Surface Geology

The surface in this area consists of flat gravel plain covered with low-relief sand dunes with about 10 m of relief. Sediments are transported from the Central Region of the Arabian Peninsula through a major now-dry wadi system and deposited in this Tertiary delta.

Partially consolidated shale, sand, and marl constitute the top 100 m of sediment. The stratigraphic column shown in figure 4.1 is from one of the deep upholes drilled in that area. It shows in general the near-surface stratigraphy

in this area. The water table (WT) is at a depth of about 60 m below the surface.

The shallowest coherent reflections commonly observed in seismic data are from the Pre-Neogene unconformity (PNU). Above the PNU is a thick layer of poorly consolidated rocks of marl, gravel, and sand. The second strong reflector is the RUS anhydrite. It is usually at an average depth of 320 m as in the lithology log in Figure 4.1. In this area, the thickness between top of PNU and top of RUS anhydrite is small, which makes it difficult to distinguish the reflection from one interface or the other in a seismic section. So, from here on, the first main event below the water table will be called the RUS.

The brute stack section in Figure 4.2 shows that the major horizons are almost continuous and interpretable. So, from the stack quality viewpoint, there are no serious problems except at isolated zones like the area between CDP 8000 and 9000. The main interpretational problems here are the long-wavelength variations in the near-surface velocity and thickness, which create erroneous time-structures. An example is the anticlinal structure at TARGET1, shown between CDP 8000 and 9000. Several structural prospects were identified by interpreters, but the structural relief is small and within the error of the near-surface velocity model.

The overburden above and below the WT are layers of low-velocity unconsolidated clay, gravels, and sand with an average velocity of 1500 m/s. Top of the bedrock is the PNU below which the limestone has an average velocity of 2200 m/s (Figure 4.1).

To estimate the depth interval of these velocity and thickness variations, zero-offset two-way times of the WT and the RUS were picked from the section

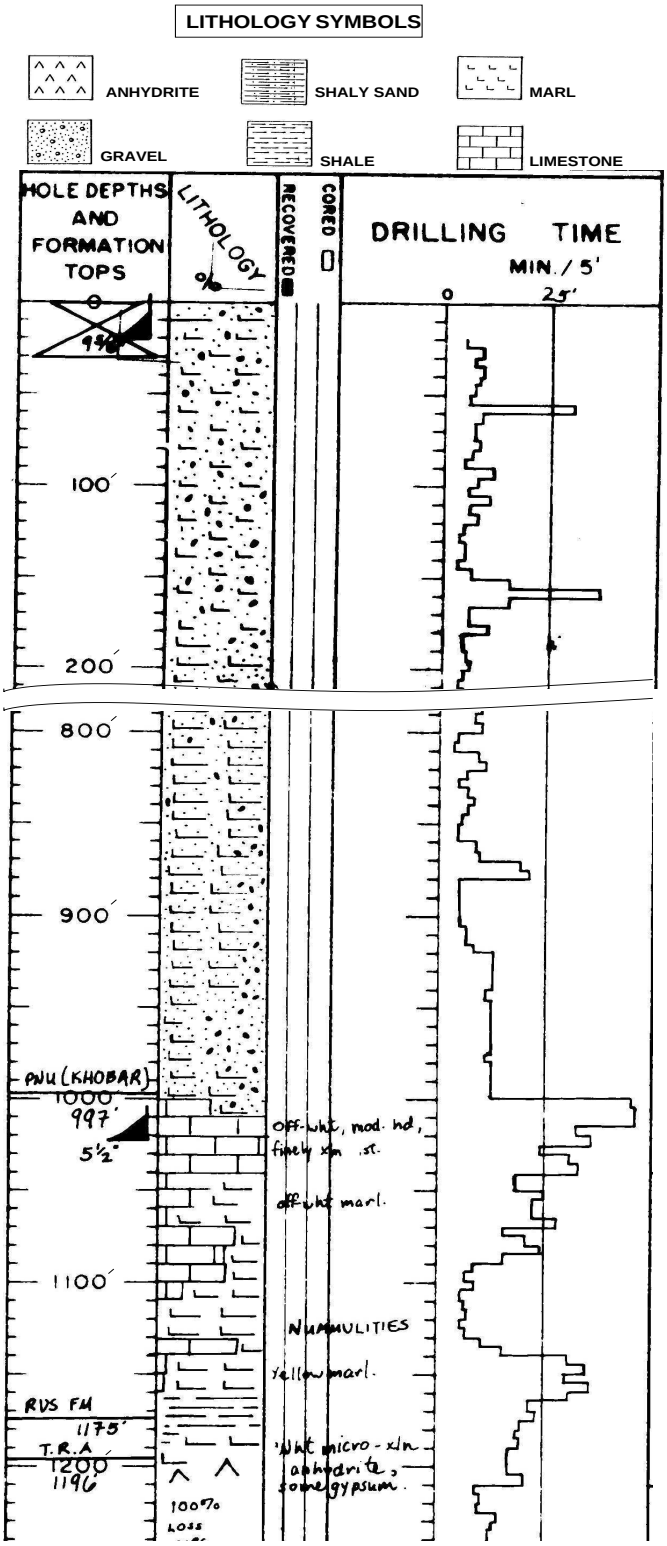

Figure 4.1. Lithology-strip log for one of the several deep upholes in this area. Depth is in feet from the surface. The key symbols are shown in the top. The deepest layer in this log is Top of RUS Anhydrite (TRA).

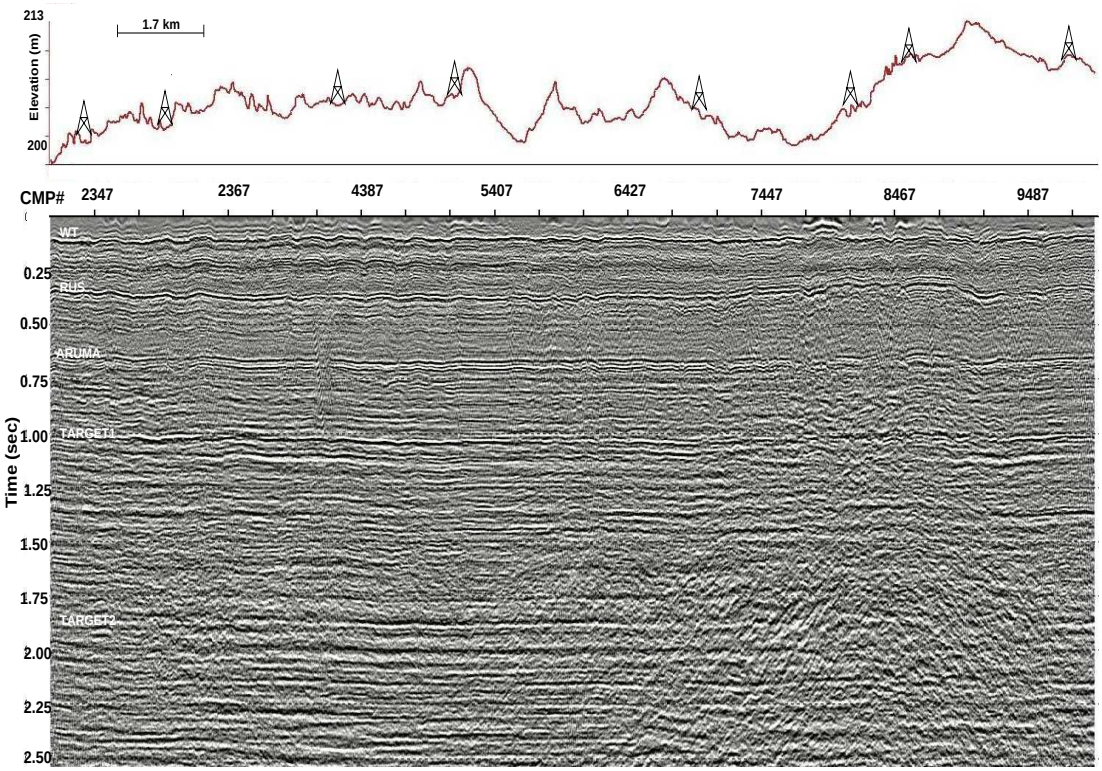

Figure 4.2. A brute surface stack of the original 5-m dataset of line Zahar1. The top panel shows the elevation profile and the projected location of the shallow upholes within 500 m.

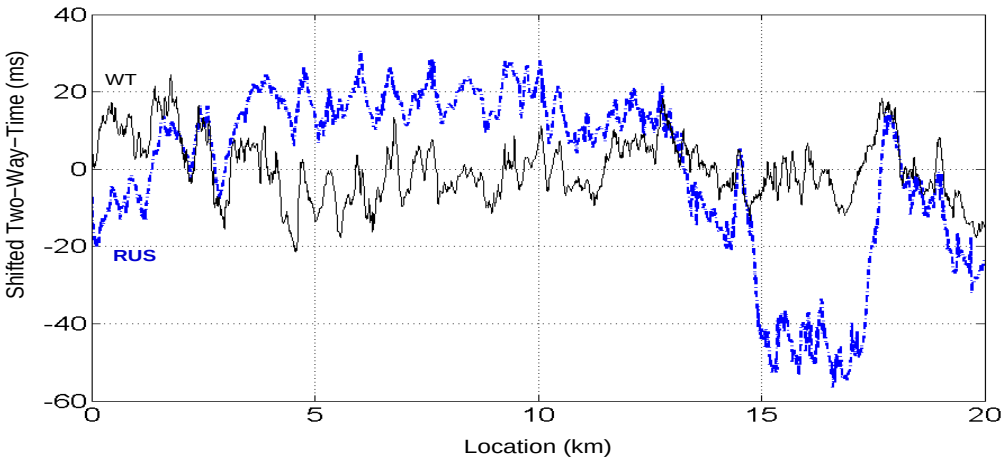

Figure 4.3. Zero-offset two-way time of the two horizons: the water table (WT) and the RUS. Both horizons were shifted so the mean is zero. The similarities between the two curves are strong indications that the near-surface anomalies are mostly above the water table.

in Figure 4.2. Figure 4.3, shows these time horizons after applying a bulk time-shift to both for ease of comparison. Velocity or thickness variations in the overburden should influence both shallow and deeper horizons, such as RUS.

One can observe a good correlation between the high-frequency components of both curves. This is a strong indication that the anomalies are mostly above the WT. The lateral extent of these variations is about 700 m. Most likely they correlate with the sand dunes. To fit the two curves, a smooth curve must be added or subtracted from one of the two curves. This indicates that the variations below the WT, velocity or thickness, are smooth and of long wavelength in nature. This is expected since the velocity stabilizes with depth especially below the water table.

These near-surface anomalies cause statics problems, which influence the final subsurface seismic image. The solution to these problems is to virtually

place the sources and receivers on a flat or nearly flat datum below the problematic overburden. The seismic datum (SRD) was mapped in the early 70s for the whole kingdom. It is a smooth surface at a depth close to the water table. The average depth of the datum in this area is about 70 m. Another possible cause of the statics problems is the existence of structural elements, such as folds or faults, that influence both shallow and deep horizons. In these cases, seismic data migration is used to obtain more accurate subsurface image.

In practice, the problem is usually addressed by applying a static correction value for each source and receiver. In the previous chapter, we discussed two classes of methods to derive the static correction: uphole-based and refraction-based methods. These methods fail in the case of complex overburden. In the following sections, it will be clear that although the topography is not complex, the uphole-based method failed to account for all near-surface variations. Residual-static corrections, however, solved some of the statics that were not accounted for by the datum statics. But, this should not be an excuse for not obtaining a good set of statics because such methods are data-dependent. The automatic residual-static algorithms work well when the statics values are small, smaller than half a wavelength, and the velocity is reasonably accurate.

4.2.2 Data Acquisition and Processing

The 2D acquisition parameters in Table 4.1 result in a dense subsurface converge with a CDP every 2.5 m. The receiver interval of 5 m enabled the accurate sampling of air and surface waves, and subsequent filtering using

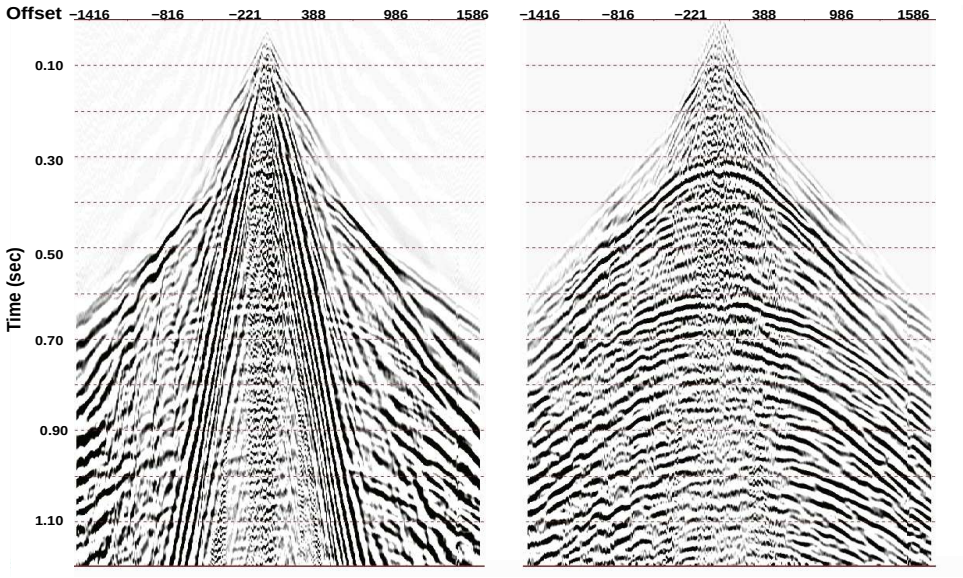

Figure 4.4. A sample common source gather from the seismic line Zahar1. The same gather after the local f-k filtering is shown in the right panel. Notice how the process, effectively, removed much of the linear noise.

frequency and f-k filters. Velocity f-k filters, however, tend to degrade shallow reflections where the fold is small. Therefore, to eradicate linear noise, local f-k filters were used. In this algorithm, the data within each small window in the t-x domain is filtered separately. The data is first decomposed into bands of frequencies. The desired range of linear velocities are rejected from each band before they are merged together again. This process is repeated throughout the shot gather with an overlap between windows. A sample shot gather is shown in Figure 4.4. This example shows the effectiveness of the filter in removing linear noise and still enhancing shallow reflections, such as the WT at 100 ms.

A normal processing sequence was used to prepare the data before stacking. The sequence includes gain recovery, deconvolution, normal moveout,

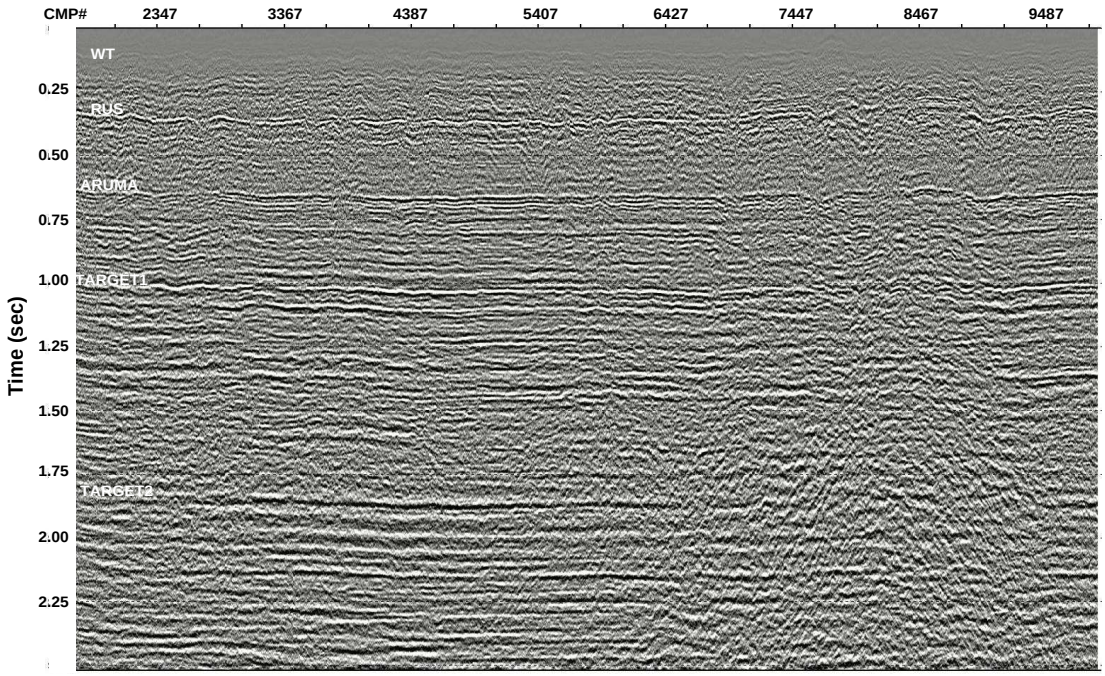

Figure 4.5. A brute surface stack of the decimated dataset.

statics application, and mute. One pass of velocity analysis and residual statics estimation was enough to improve the coherency of the stack.

Data Decimation: The small 5-m source and receiver spacing is not a conventional 2D acquisition parameter. To simulate a conventional 2D dataset, the data were decimated at 25-m source and receiver intervals. The same processing sequence was used here again to generate the final time image.

For a fair comparison, the decimated dataset was restacked again without applying any kind of statics. The result is shown in Figure 4.5. In the next section, several techniques are used in which the datum statics are estimated and applied to the prestack data.

4.2.3 Near-Surface Correction

In this section, The prestack data are processed to correct for the near surface. In the first subsection, the velocity model is built using discrete upholes. In the second subsection, the original high-resolution seismic data are used to build the velocity model. In each case, the statics values are calculated and applied to the prestack decimated gathers. In the third subsection, the high-resolution velocity model from the second subsection is used for wavefield extrapolation.

Uphole-Based Statics Correction: The conventional way of creating a near-surface velocity model in this part of the world is the frozen model. A velocity-to-datum map has been compiled for the whole country using velocity information from thousands of shallow upholes. The statics correction values for any source or receiver location are found using the survey elevation of the point and velocity from the velocity map. For comparison purposes, static values derived this way were used to correct the prestack data. The top label in the brute section in Figure 4.2 shows the upholes locations. These wells are within 500 m of the line.

Figure 4.6 shows the stack after applying the uphole-based statics. When compared to the surface stack, Figure 4.5, the improvements in the stack quality are small; see, for example, the horizons below TARGET2. In some parts of the section, there is a degradation in the stack quality.

High-Resolution-Stack-Based Statics Correction: In the previous chapter, I suggested using the stack of the high-resolution data to help compute the datum statics. One proposal is to use the stack directly to compute

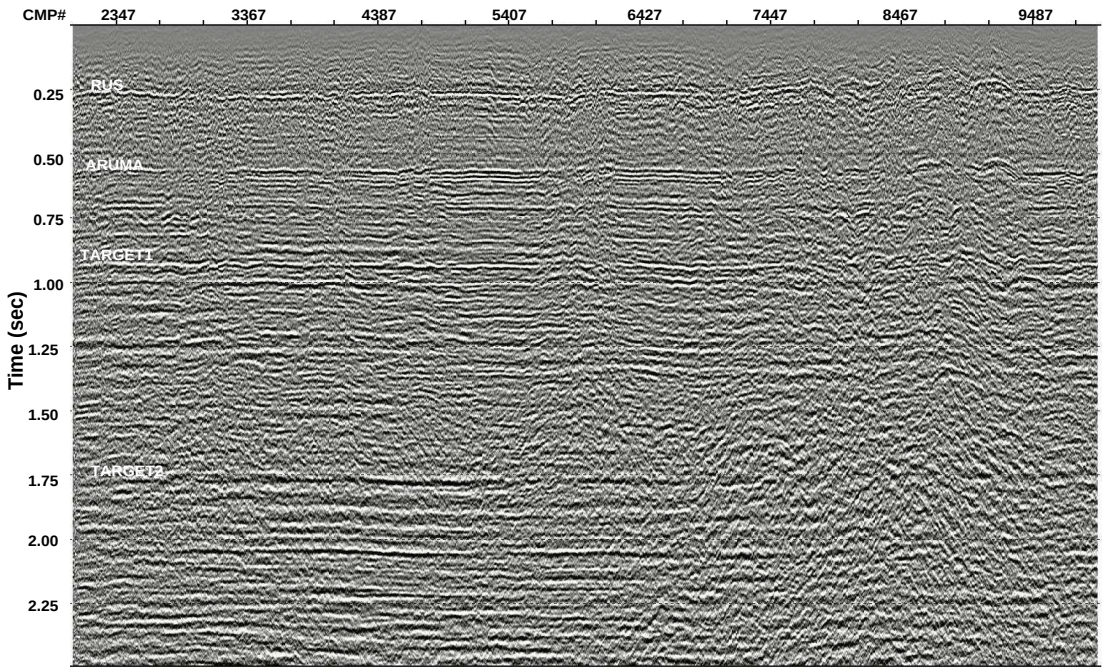

Figure 4.6. The initial stack after applying the uphole-based statics.

the two-way vertical time to a near-surface reflector. The near-offset traces (offset $<$ 200 m) of the 5-m data were processed and stacked. The result is a high-resolution stack section that images the WT clearly as in the stack in Figure 4.2. Here the WT is treated as a local datum and the reflections from the shallow WT are picked. The source and receiver statics are calculated from the total vertical time, which are decomposed in a simple surface-consistent way into source and receiver datum statics.

The advantage of this simple datuming technique is that the datum is a physical reflector rather than a hypothetical plane defined at a specific subsurface depth and x-y coordinates. Of course, it is preferable that such a datum be as flat as possible to obtain interpretable section. In this example, the WT is a good reflector located at a depth of about 60 m below the surface, that is

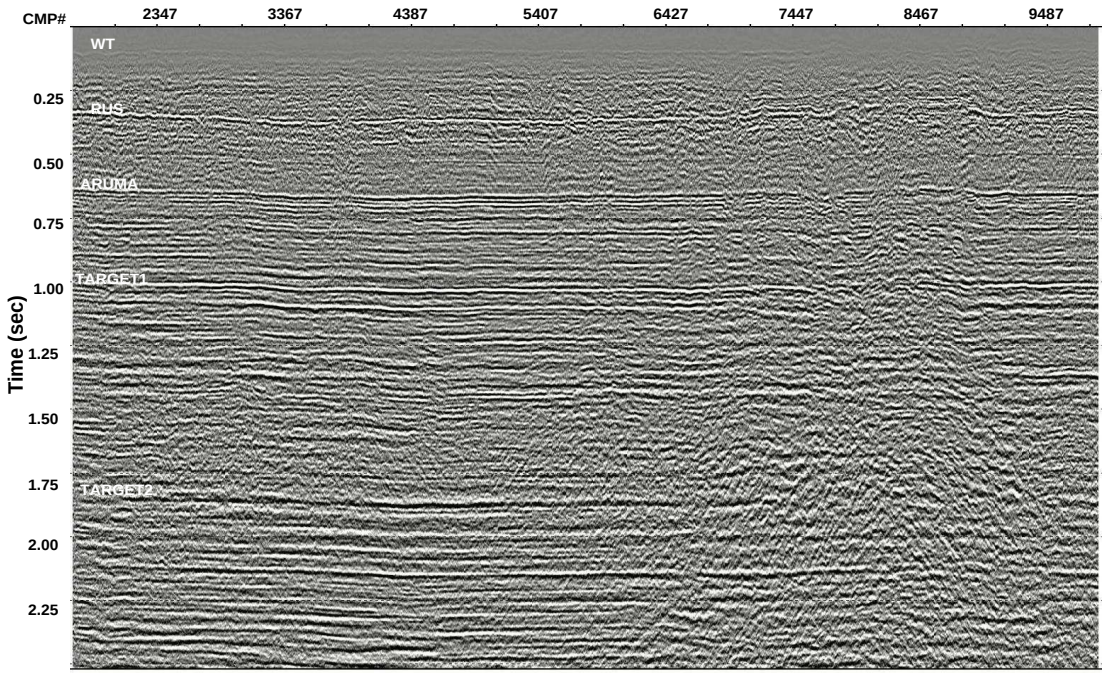

Figure 4.7. The initial stack after using the stack-based statics in the near-surface corrections.

about 80 ms two-way time (Figure 4.2).

An intermediate floating datum was created by smoothing the surface elevation. The total datum statics are also smoothed the same way. The high-frequency statics are computed by subtracting datum statics from the smooth profile. This part of the statics is applied in the prestack domain, while the smooth part is applied poststack.

Figure 4.7 shows the stack after applying the stack-based statics. When compared to the uphole-based stack, there are noticeable improvements in stack quality. Notice that the same processing parameters, but slightly different stacking velocity functions, were used for both stacks. In particular, the horizon continuity of TARGET1 and TARGET2 are improved. The horizon TARGET1 now is interpretable below the CDP range $8000 - 9000$. Another

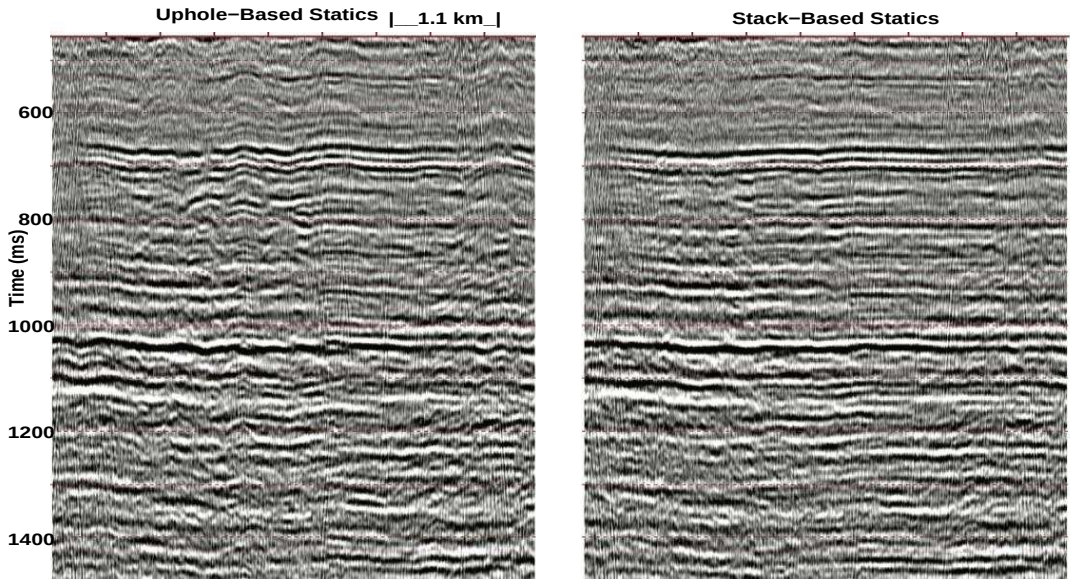

Figure 4.8. A small window showing the improvements of using the stack-based statics over uphole-based statics.

important difference between the two stacks is the shape of the main horizon TARGET1. A small window around TARGET1, which is at about 1 second, shows more clearly the differences in their shapes (Figure 4.8). The two stacks are from two different datums, the WT and the SRD. However, these datums are close to each other as we will also see in the next section.

Short-wavelength statics influence not only stack quality but also any subsequent multi-channel processes, such as conventional velocity analysis. Figure 4.9 shows two coherency analysis panels for the same CDP gather after applying the two different statics. The uphole-based statics were applied to the left panel, while the stack-based statics were applied to the right panel. Notice how the velocity coherency is more focused and well defined in the right panel especially around 1000 ms and 2200 ms.

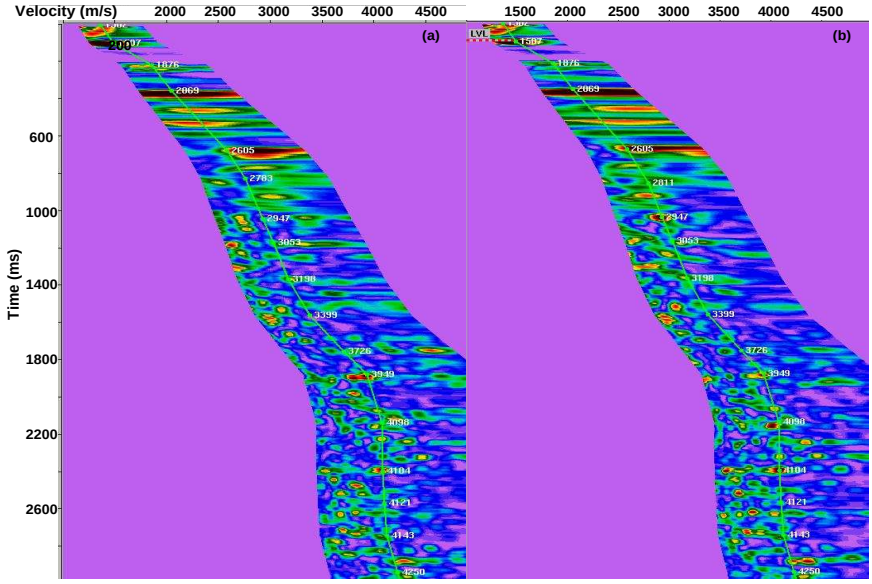

Figure 4.9. Two velocity-analysis panels for the same CDP gather, but using the two different sets of statics. The uphole-based statics were applied to the left panel, while the stack-based statics were applied to the right panel.

Model-Based Statics Correction: Another method to calculate the datum statics is to build a near-surface velocity model first. The statics values are calculated based on depth of the SRD. Here, the simple conventional velocity analysis is used to build the velocity model. Horizon-based velocity analysis (HVA) was used because the high-resolution data along the whole line are available. The accuracy of this procedure depends on the accuracy of the picked horizon time. If high-resolution data were acquired at discrete locations along the line, then vertical velocity analysis only might be utilized. The near-surface in this area consists mostly of partially consolidated sediments, which have weak anisotropy and layering. The layers are almost flat with no abrupt structures. For all these reasons, the stacking velocity is a good estimate of the interval velocity.

The WT velocity model shown in Figure 4.10 was built using conventional seismic velocity analysis of the high-resolution dataset. Zero-offset time for each CDP was picked from the stack in Figure 4.2. The RMS velocity at each CDP was estimated using the HVA-based velocity analysis. In the model, I also posted the time-depth points calculated from the check-shot surveys. The objective is to show the accuracy of the model at the upholes locations. Although this model was built using every CDP, every 2.5 m, an accurate model might be built using a point every $\mathbf{n^{th}}$ CDP, where n is an integer.

The model in Figure 4.10 was decimated to every 800 CDP to simulate an uphole survey every 4 km. Statics were estimated from this model and applied to the gathers of the decimated line. Reflection residual statics were calculated and applied to resolve the high-frequency near-surface variations. The result is shown in Figure 4.11, which is superior when compared to the uphole-based stack in Figure 4.6. The major horizons, TARGET1 and TARGET2 are now more continuous over the whole line. Moreover, the time images in both stacks are different; for example, refer to horizon TARGET1. Although the uphole coverage in this area is dense, most of them are not exactly on the line. Also, some of the upholes are not deep enough to penetrate the datum.

Most of the medium to long near-surface anomalies have bee resolved in the decimated model. To fully resolve all anomalies, the pseudo-uphole interval needs to be made smaller. To test this idea, the whole process was repeated, but for a decimation interval of 1 km. Figure 4.12 shows a comparison between the 1-km and the 4-km stacks. The apparent closure in horizon TARGET1 in the 4-km stack does not exist in the 1-km stack. Since most of the prospects in this area have small structural relief, the high-resolution based method will

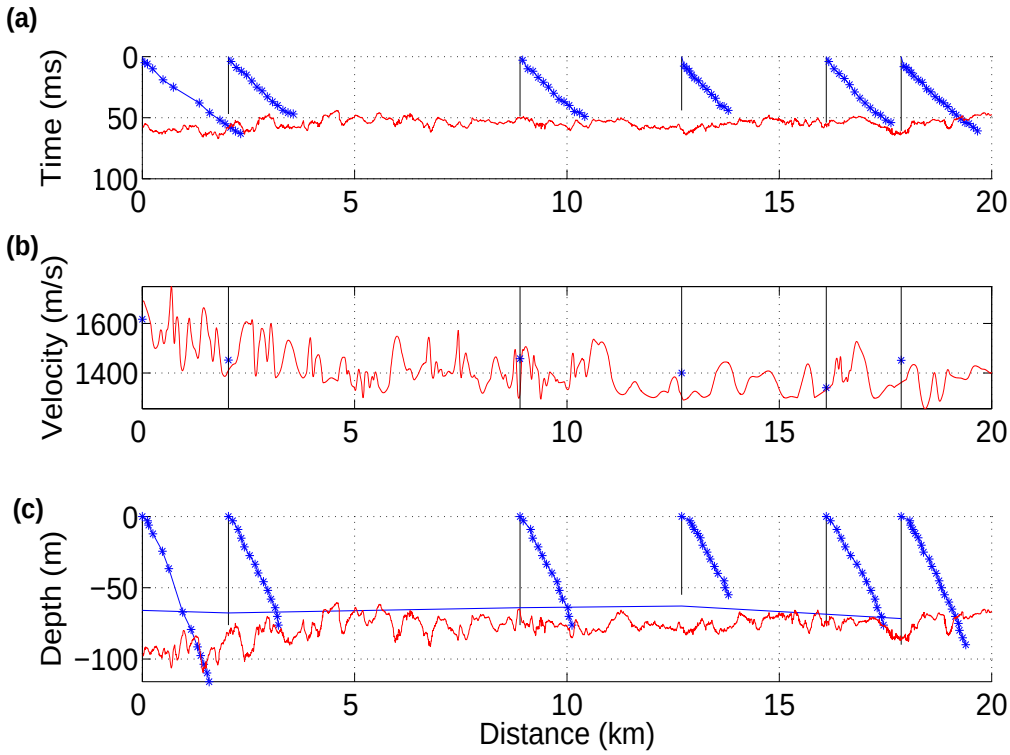

Figure 4.10. A composite plot showing the WT seismic-based velocity model (red curves). The picked one-way time, the estimated RMS velocity, and the calculated depth are shown in panels (a),(b), and (c), respectively. The curves with "*" marks in panel (a) are the check-shot data for six upholes along the line. The same data are shown in depth in panel (c). The "*" marks in panel (b) are the WT RMS velocity calculated from the same check-shot data. The smooth curve in panel (c) is the SRD along this line.

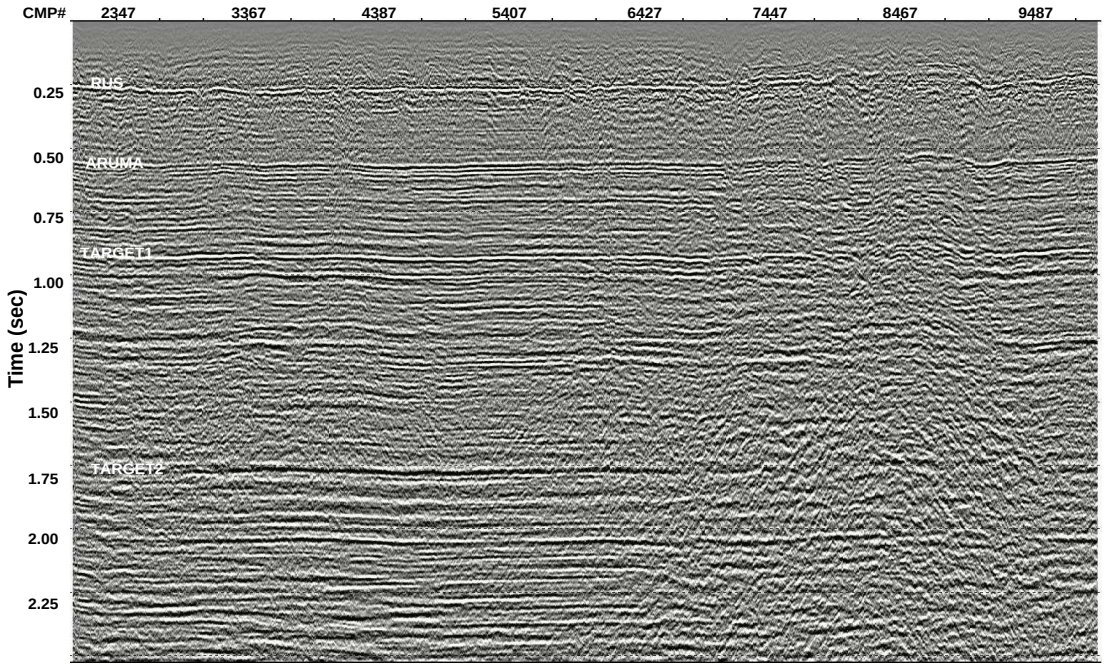

Figure 4.11. The stack after applying statics from the decimated (every 4 km) version of the model in Figure 4.10.

help discriminate true structures from anomalies.

High-Resolution-Model-Based Datuming: The purpose of applying statics to prestack data is to correct the kinematics of the data in such a way the shots and receivers are downward continued to a flat datum below the complex near-surface. A more accurate technique to accomplish this is through wavefield extrapolation using the near-surface velocity model. Figure 4.13 shows the result of applying wave-equation-based extrapolation technique. The horizons are better imaged than the stack in Figure 4.11; see, for example, the reflector at 1.2 sec. When compared to the uphole-based stack in Figure 4.14, the redatuming-based stack is more continuous throughout the line.

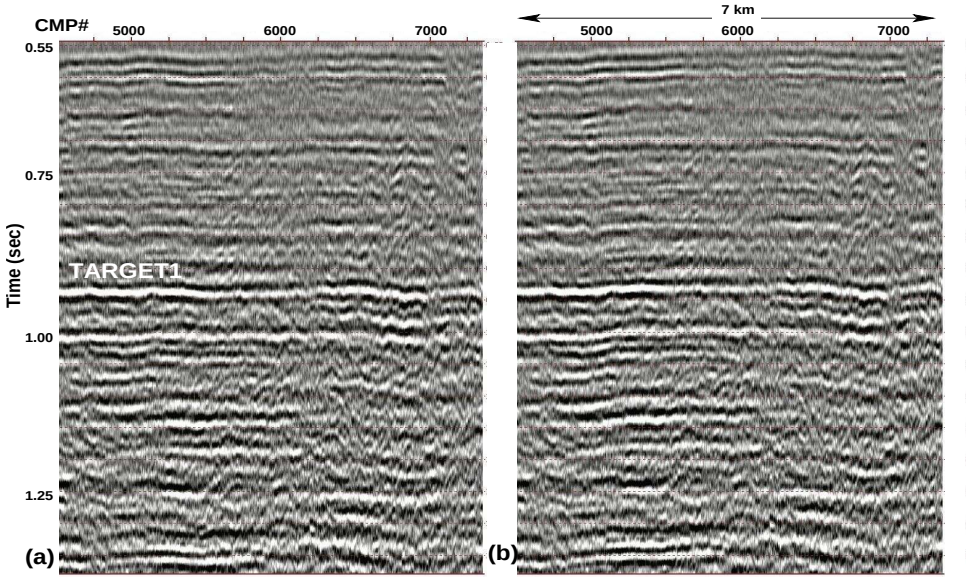

Figure 4.12. Two stacks which were corrected using velocity-model-based datum statics and residual reflection statics. The model sampling interval is 1 km in stack (a), and 4 km in stack (b).

The wavefield extrapolation technique works best when the wavefield is sampled more accurately. Figure 4.15 shows the result of redatuming of the original 5-m dataset. The stack has improved for all horizons including TARGET1 and TARGET2. In fact, the horizons are more interpretable inside the noisy zone below CDP 9000.

Summary: In this line (Zahar1), the high-resolution data used in velocity modeling were not typical shallow seismic data (Miller et. al, 1989). A heavy low-frequency vibrator and 12-Hz geophones were used data acquisition. Nevertheless, the output velocity model was more accurate than using a grid of costly upholes. For more cost-effective approach, discrete high-frequency CDP gathers can be collected and processed individually and then integrated together to build the final velocity model.

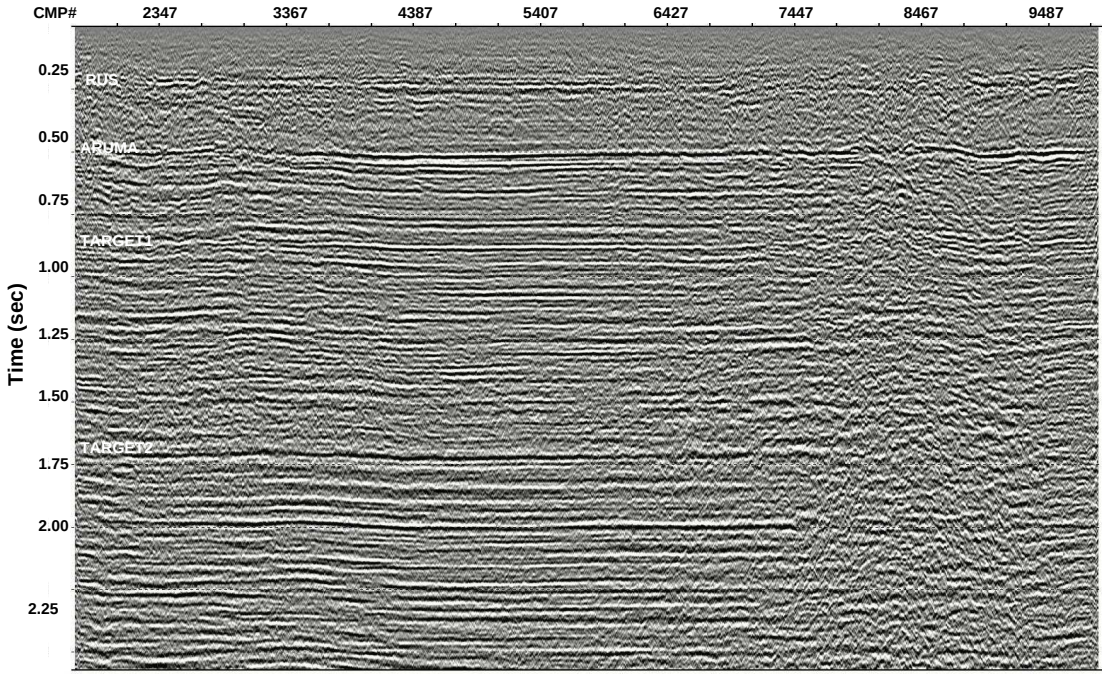

Figure 4.13. The stack of the decimated gathers after wavefield extrapolation to the SRD.

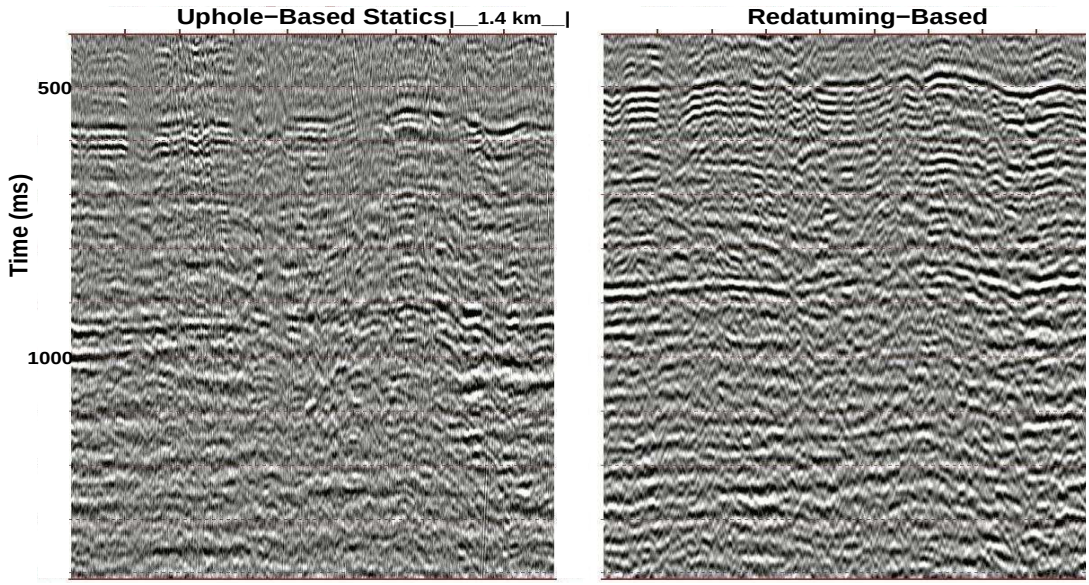

Figure 4.14. A small window from the sections at Figure 4.11, the left section, and Figure 4.13, the right section.

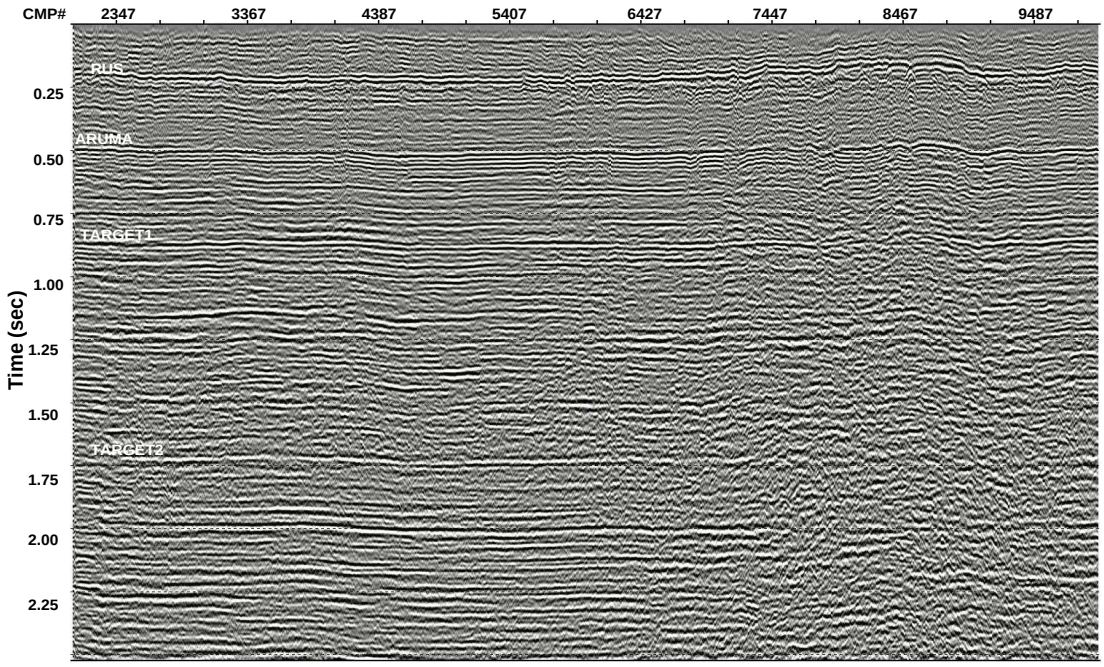

Figure 4.15. The stack after wavefield extrapolation to the SRD. Here the original 5-m dataset were used.

Table 4.2. Line Zahar2 acquisition parameters.

receiver interval	10 m
traces/shot	1440
source interval	10 m
CDP interval	5 m
maximum fold	720
source type	sweep 8-96 Hz
sampling interval	2 ms

When an accurate near-surface velocity model exists, wavefield extrapolation is a more accurate alternative way for near-surface correction. It gives a better result than the simple statics correction.

4.3 Line Zahar2

This line was acquired in the same area as line Zahar1 (about 20 km away). The surface and near-surface geology are similar to that in the area of line Zahar1. The terrain is a flat gravel plain covered by small 10-m high sand dunes. The main near-surface reflectors are the water table (WT) at a depth of 80 m and the RUS at a depth of about 300 m.

4.3.1 Data Acquisition and Processing

The acquisition parameters of the line, shown in Table 4.2, are not typical 2D acquisitions parameters in Saudi Arabia. The small source and receiver intervals (10 m) are used for the testing purposes similar to line Zahar1.

Part of the brute surface stack for line Zahar2 is shown in Figure 4.16. The stack quality of this line is good in general. Unlike Zahar1 (the original 5-

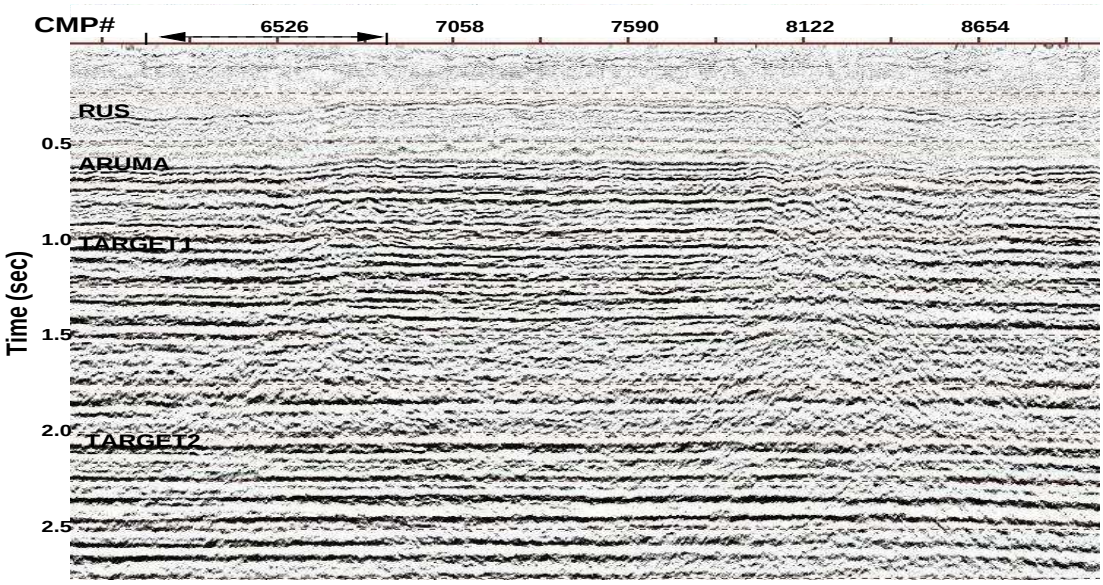

Figure 4.16. Part of line Zahar2 surface stack. Note that the CDP interval is 5 m. The double-head arrow shows the interval covered by the high-resolution line.

m line), the WT here is not as clear. The main problem, however, is whether the deep low-relief structures are created by near-surface statics anomalies. Any statics solution should distinguish between statics anomalies and true structures. The synthetic line and line Zahar1, show how the high-resolution-based technique provided a more accurate and reliable near-surface velocity model.

4.3.2 High-Resolution Line

For this line (Zahar2) and the next line (Dilam1), shallow high-resolution seismic data were acquired. A high-resolution 2D seismic line was acquired along about 3 km of the line using the parameters in Table 4.3. The source interval is double the receiver interval. This make the CDP interval smaller,

Table 4.3. Acquisition parameters of the high-resolution line.

receiver interval	5 m
source interval	2.5 m
no. of channels	112
max. offset	560 m
min. offset	3 m
CDP interval	2.5 m
maximum fold	112
source type	vibroseis (30-300 Hz)
sampling interval	0.5 ms
record length	1000 ms

which improves the accuracy of the image and the velocity model without additional cost.

A sample raw shot gather is shown in Figure 4.17 after the application of AGC for display purposes. Random noise overcomes the signal beyond an offset of about 250 m. Loose sand covering the area probably absorbs the input signal quickly, therefore a stronger input signal might be needed in this area. The prominent dipping energy in the middle of the gather has a velocity of about 210 m/s, which is slower than the speed of sound in air, about 300 m/s. These are probably surface waves, given that they are lower in frequency. These waves tend to divide the gather into two zones; the near-offset noise cone and the optimal window (Hunter et al., 1984). Within the optimal window, there are clear events, which could be guided waves or near-surface reflections.

The first breaks are easy to pick for offsets less than 250 m. Three distinctive layers corresponding to three different slopes in the first breaks can be identified. The top loose sand has velocity of about 500 m/s. The deep layer has a velocity of about 2500 m/s. The thick middle layer has a velocity

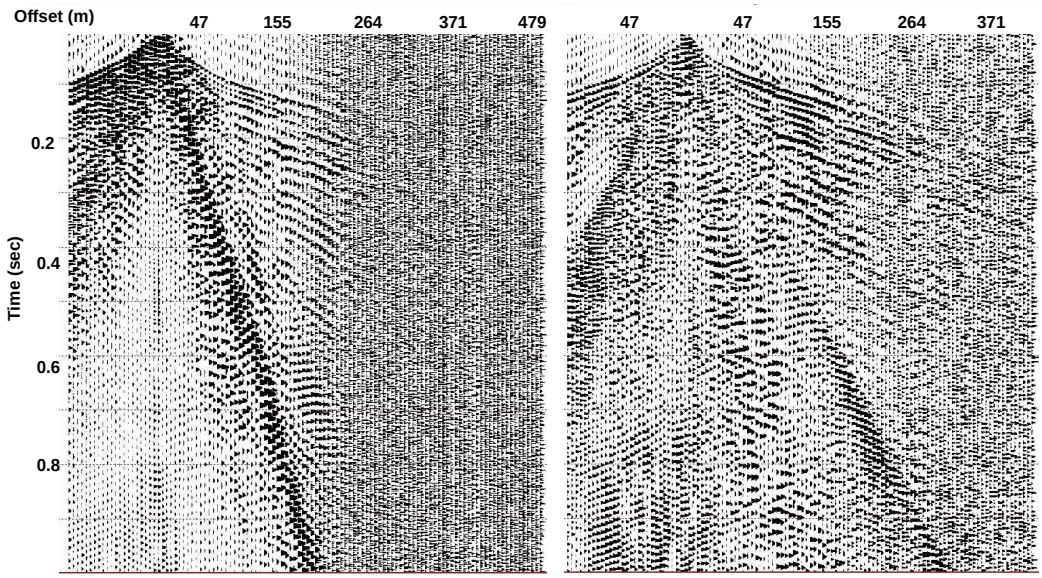

Figure 4.17. Two shot gathers, 70 m apart. The left gather is a raw shot gather, while the right gather is the same gather after applying the processing sequence below.

of about 1400 m/s as shown in the sample shot gather in Figure 4.18. These first-arrival picks can not be distinguished and picked from production shot gathers even when sampled every 5 m, as seen in the sample shot gather of line Zahar1 in Figure 4.4. These picks can be fed into any refraction-based inversion software to generate a high-resolution velocity model.

The maximum frequency in the input sweep is 300 Hz. The frequency spectrum of the gather in Figure 4.17 is shown in Figure 4.19. Clearly, not all the input frequencies were recovered. In fact, the maximum recovered frequency is about 140 Hz, but frequencies above 100 Hz are probably random noise.

Three common-offset gathers are shown in Figure 4.20. The high-frequency first-arrival event (E1) is clear at offsets 100 m and 200 m, but invisible at an

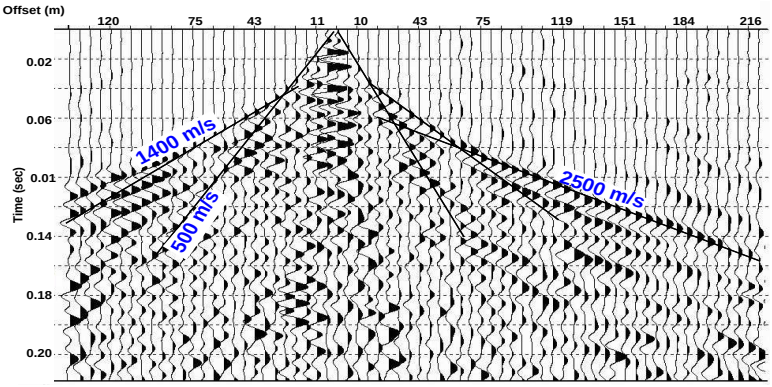

Figure 4.18. A sample shot gather showing the refraction arrivals and their velocities.

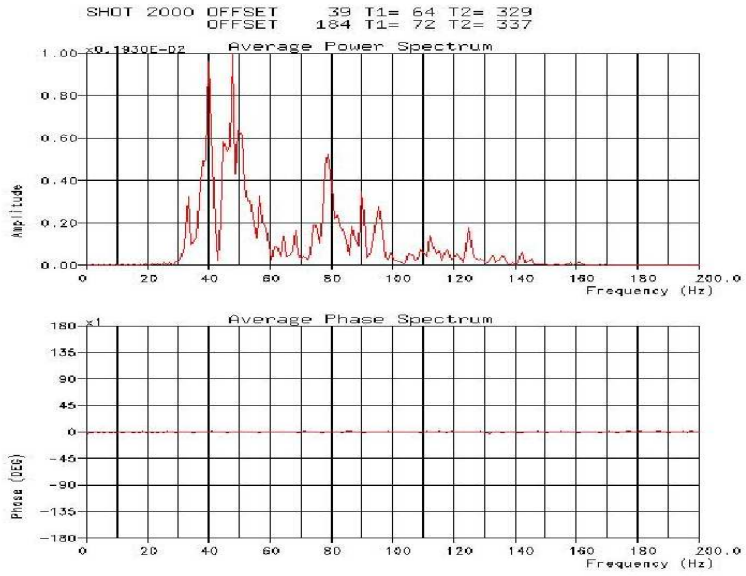

Figure 4.19. Frequency spectrum of the shot gather in Figure 4.17.

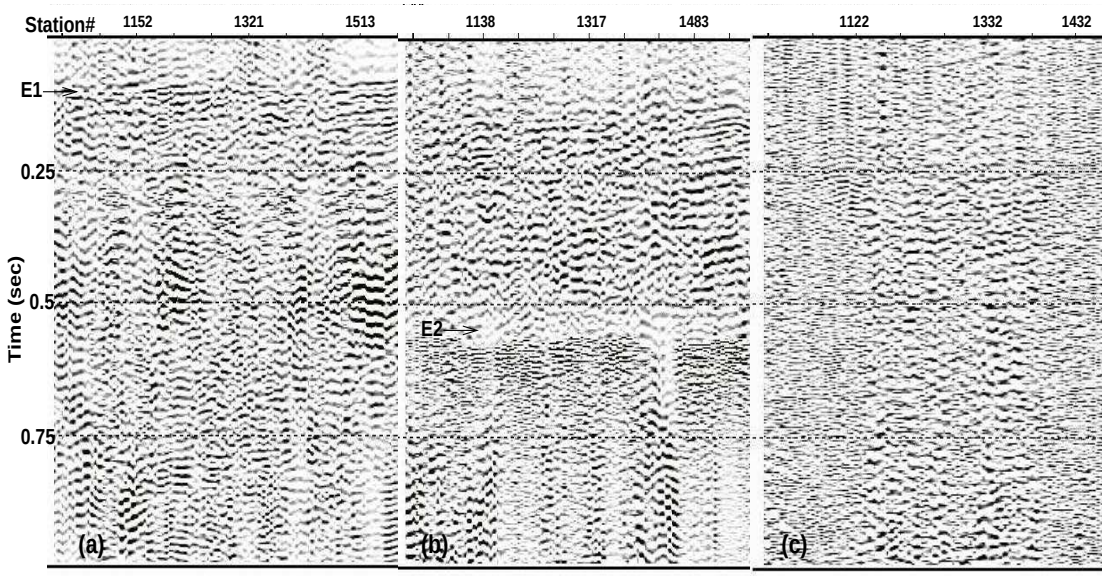

Figure 4.20. Common offsets (a) 100 m, (b) 200 m, and (c) 400 m.

offset of 400 m. The white band in the middle of the 200-m-gather (E2) marks the edge of the noise cone zone. At certain stations, for example 1120-1330, one can see signal up to offset 400 m.

Figure 4.21 shows the frequency spectrum of the the first 250 ms of the 100-m gather. This zone includes mostly refracted and guided waves, but some events may be reflections. It certainly shows that the maximum recoverable frequency is about 110 Hz. The spectrum shown in Figure 4.22 is for the 400-m gather. Since the maximum recoverable frequency is 110 Hz, energy above this frequency should be mostly noise. This comparison shows that at 400 m offset, noise amplitude is at about the same level as the signal amplitude. Stacking these noisy traces still helps enhance the final stack, however.

Data Processing: To use this data in velocity estimation, the data have to be processed carefully. After extensive testing, the processing sequence

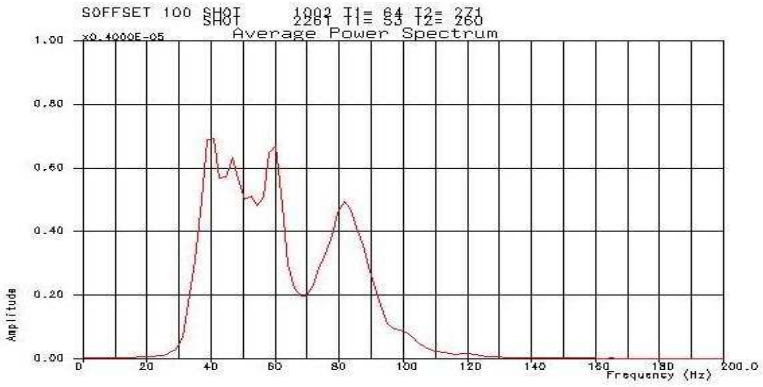

Figure 4.21. Frequency spectrum for the top 250 ms of the 100-m common-offset gather.

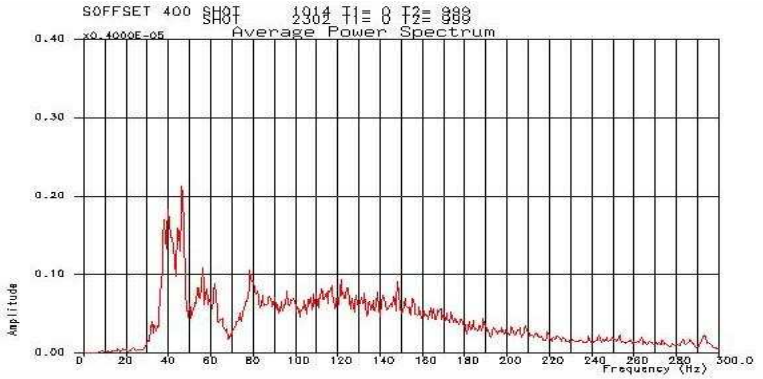

Figure 4.22. Frequency spectrum of the common-offset gather for offset of 400 m.

Table 4.4. High-resolution data processing sequence

Process	Description
1-Preprocessing	data editing and geometry assignments
2-Filtering	frequency and f-k filtering
3-Statics	elevation statics
4-Mute	mute first arrival
5-Deconvolution	gap deconvolution
6-Residual and velocity analysis	three iterations or refinements
7-Normal moveout	50% stretch mute
7-Trim statics	non-surface-consistent statics
8-Stacking	
9-Filtering	poststack frequency filtering

in Table 4.4 was used.

The f-k filter used in this sequence is a local filter applied over a movable window in t-x domain. The right panel of Figure 4.17 shows a sample shot gather after processing. The low-velocity surface waves are aliased which cause erroneous flat events after f-k filtering. some of the linear data are aliased and this f-k program unfortunately does not account for this problem. The data were put through three iterations of velocity and residual statics estimation in order to improve the time image and to better estimate the velocities.

Figure 4.23 is the final stack after processing the data using the sequence in Table 4.4. The final prestack trim statics greatly helped align the events and produce a better stack. This process was applied just before stacking to improve the continuity of the events. The process does not improve velocity picking because, after application of trim statics, the data would be biased to the applied NMO velocity. The final stack shows a strong continuous reflector at 100 ms, which corresponds to the water table (WT). Between 300 and

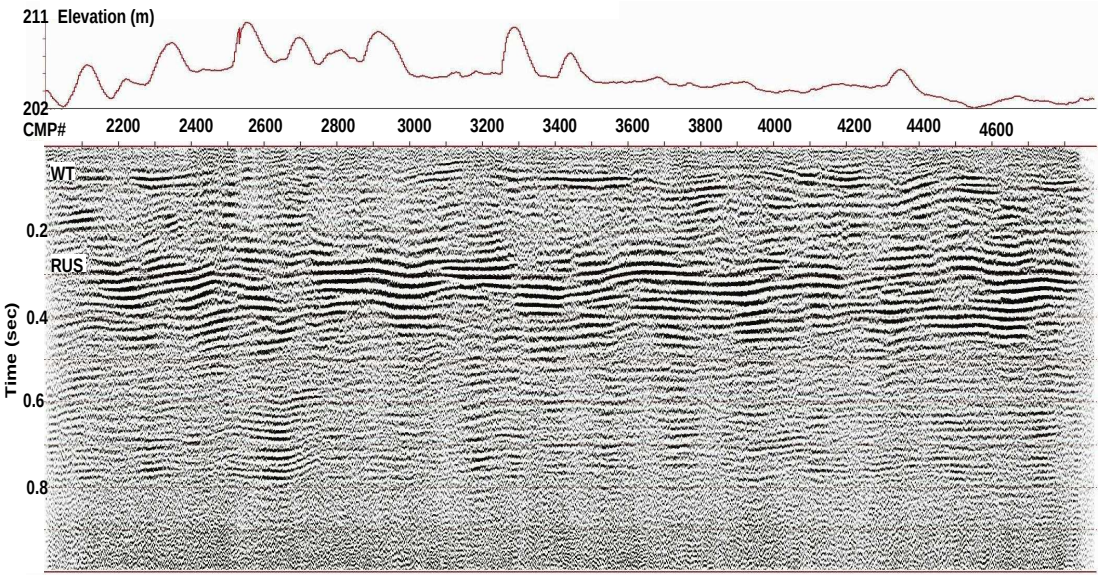

Figure 4.23. The final stack of the high-resolution data. The top plot is the elevation profile along the line.

400 ms there is a sequence of continuous reflections. The truncations and overlapping might be a result of the steep slopes in the face side of the dunes.

Building the Velocity Model: It is difficult to track a particular near-surface horizon through the whole line. For this reason, I believe that conventional stacking velocity analysis is the most usable and robust method in this case.

Refraction tomography is another applicable method in this case. However, the first arrival becomes very difficult to pick beyond an offset of 250 m. From the rule of thumb, this means that the penetration depth is about 50 m, one fifth of the maximum offset (Stefani, 1995).

Figure 4.24 shows the final velocity-depth model obtained using stacking velocity. The velocities were converted to interval velocity using Dix equation

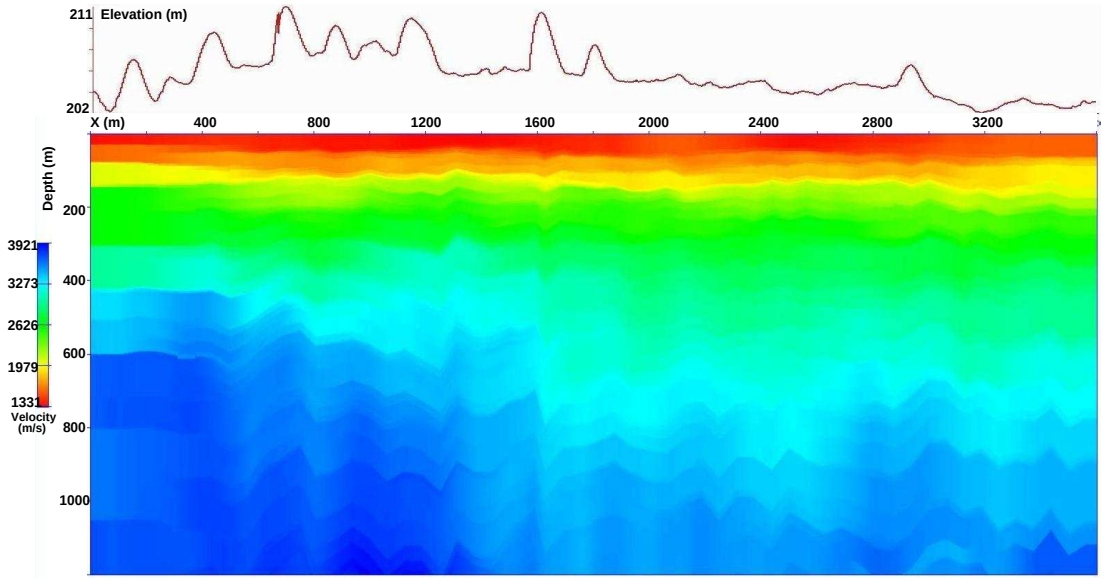

Figure 4.24. The final velocity model obtained from stacking velocities V_{stk} converted to interval velocities using Dix equation and smoothing.

and smoothing. Notice the fine details in the model shown more clearly in the enlarged section in Figure 4.25. In particular, the model shows a top-layer with a velocity of about 1400 m/s and a thickness of 100 m below which the velocity is about 2500 m/s. These velocities agree with first-break velocities, except that the top 500-m/s layer is not visible here. The top sand velocity of about 500 m/s can not be resolved from the reflection analysis only.

4.3.3 Statics and Redatuming

In this section, the estimated near-surface velocity model from the high-resolution line is applied to the conventional data of line Zahar2.

The velocity model was used to derive a set of datum statics for all source and receiver stations. Statics times are calculated by vertically integrating velocity from the surface to the seismic datum. Typically, residual reflection

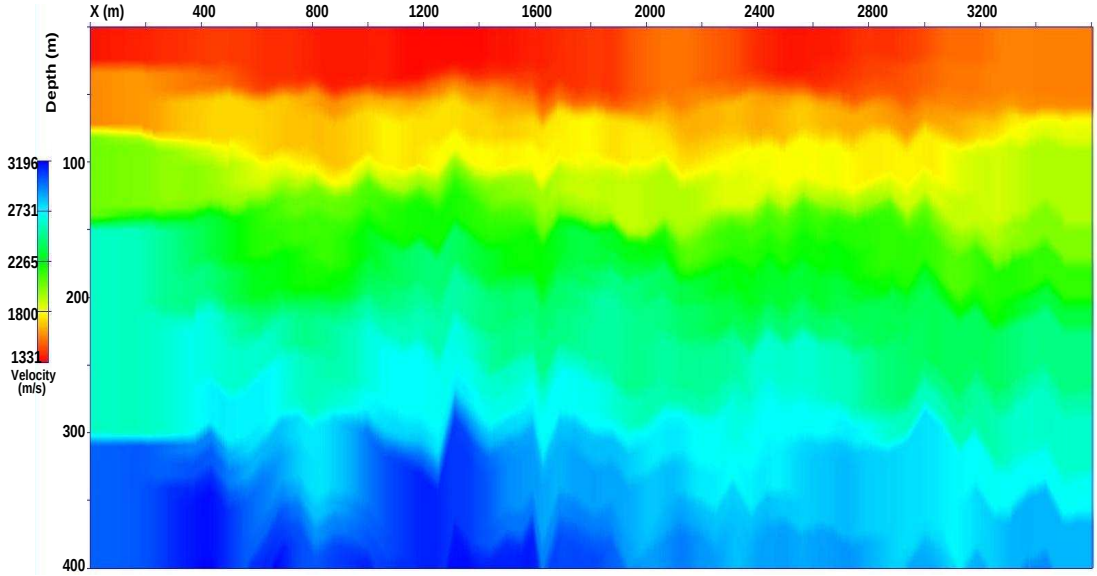

Figure 4.25. An enlarged window of the model shown in Figure 4.24.

statics are estimated and applied after applying datum statics. Figure 4.26-(a) shows the final stack of line Zahar2 after using the high-resolution-statics. The stacks at (b) and (c) have their datum statics derived from uphole-based and refraction-tomography models respectively. In general, there are no obvious differences between these three stacks. Actually, there are minor differences, which were eliminated after applying the reflection residual statics.

One major advantage of the high-resolution-based modeling is the deep penetration of reflected waves and , therefore, the ability to use a deeper reference datum. Conventional methods are limited either by depth of penetration, such as the refraction-based methods, or cost of operation, such as the uphole-based methods. Intuitively, the deeper the datum is the more near-surface effects are canceled from the seismic data. In this dataset, three datums were used at different depths, 100 m, 200 m, and 400 m, to demonstrate the effect of datum elevation on the final time image. A set of datum statics were cal-

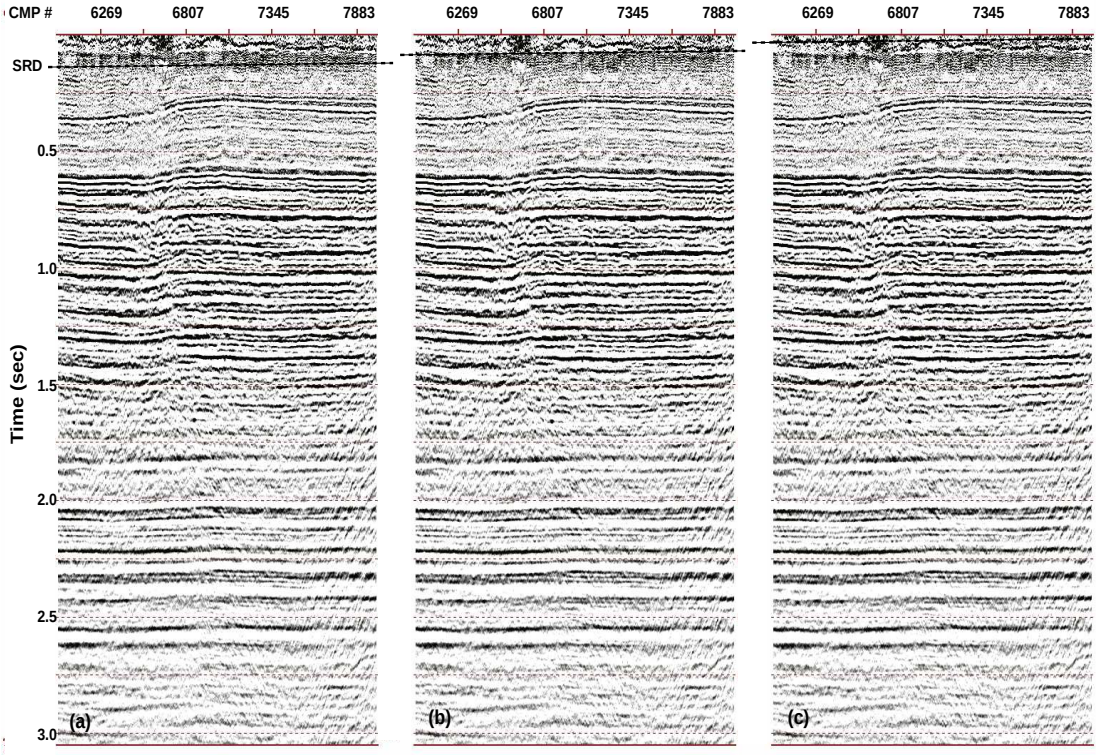

Figure 4.26. The stack of line Zahar2 after applying datum statics derived from the high-resolution velocity model, stack (a), uphole-based model, stack (b), and tomography-based model, stack (c). For display purposes, stack (a) was shifted by 100 ms, while stacks (b) and (c) were shifted by 70 ms and 40 ms, respectively.

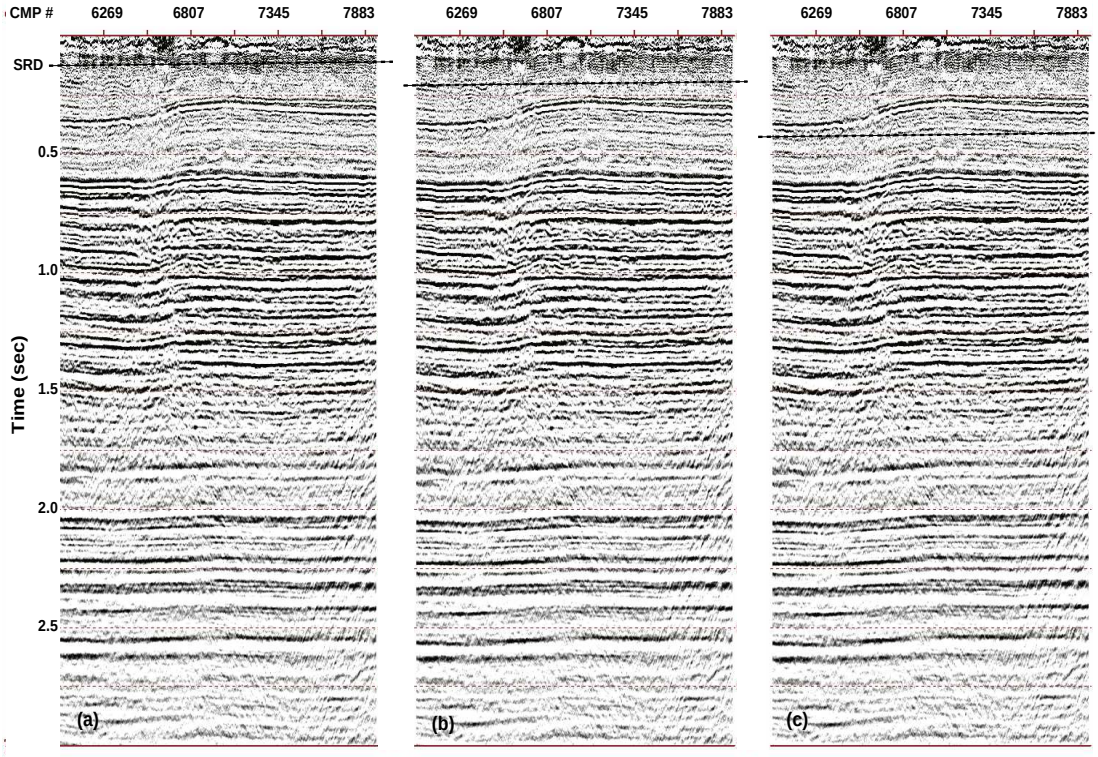

Figure 4.27. The stack after applying datum statics derived from the high-resolution velocity model. The SRD datum was set at a depth of 100 m for stack (a), 200 m for stack (b), and 400 m for stack (c). For the display purposes, stack (a) was shifted by 100 ms, while stacks (b) and (c) were shifted by 200 ms and 350 ms, respectively.

culated for every datum, which then were applied to the seismic data before stacking. Figure 4.27 shows the final stack for the three datums. There are some minor improvements in the stacks, for example the horizons at around 1.5 and 2.1 sec.

The main problem in this area, however, is the ability to distinguish genuine low-relief structures from statics anomalies. The enlarged plots in Figure 4.28 show that time structures change with depth of the datum. This should give the interpreter more confidence in any mapped structure.

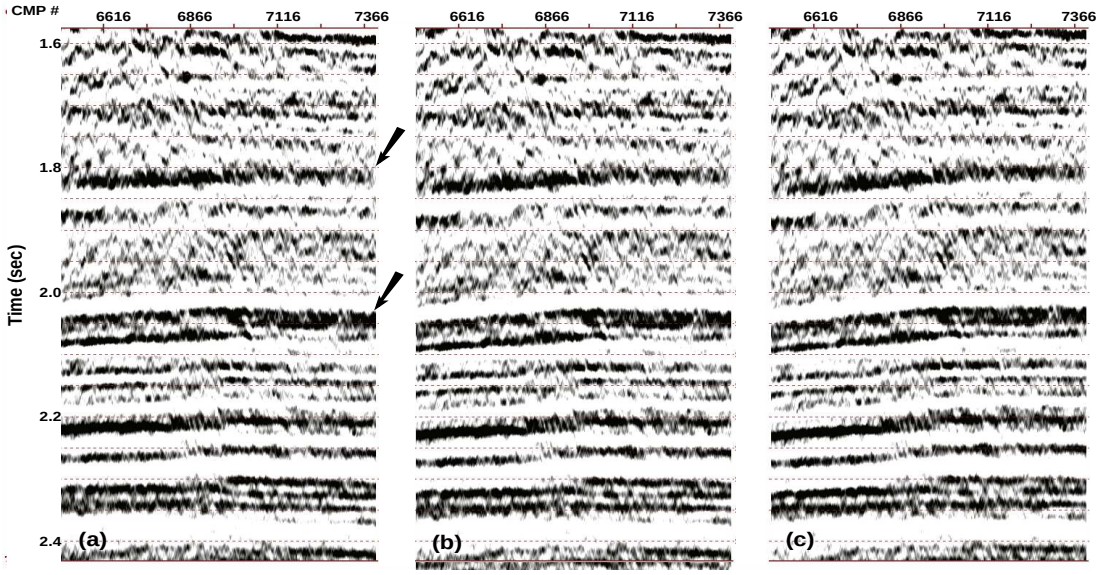

Figure 4.28. An enlarged window from the stacks in Figure 4.27. Notice how the dip of the horizons change direction as a deeper datum is used. The arrows point to two major horizons.

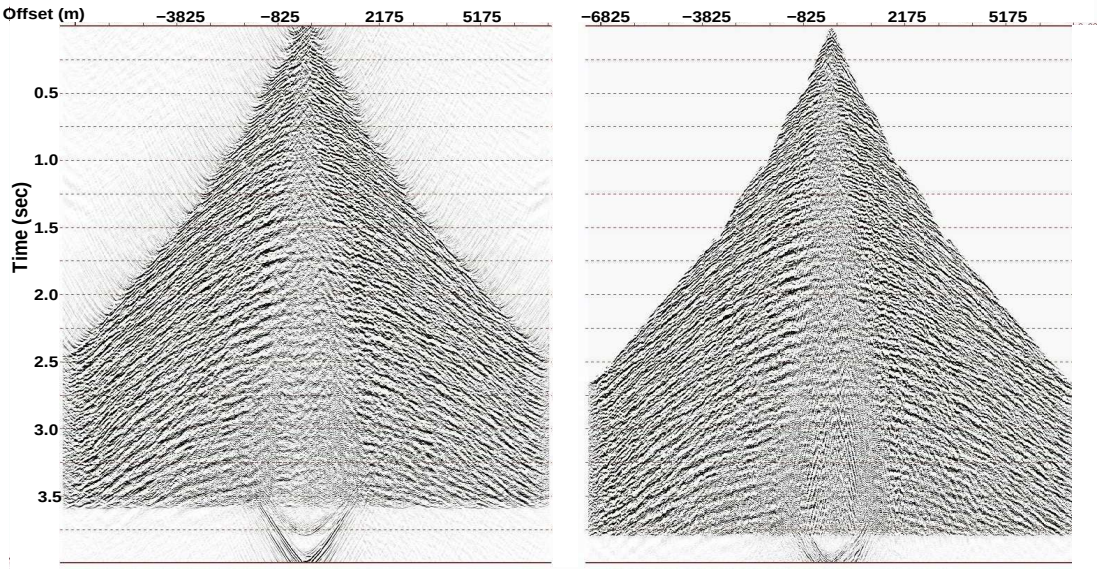

Figure 4.29. A common-receiver gather before and after redatuming. The receivers are redatumed to the new datum first. In a subsequent step, the data are sorted into common-receiver gathers and sources are redatumed.

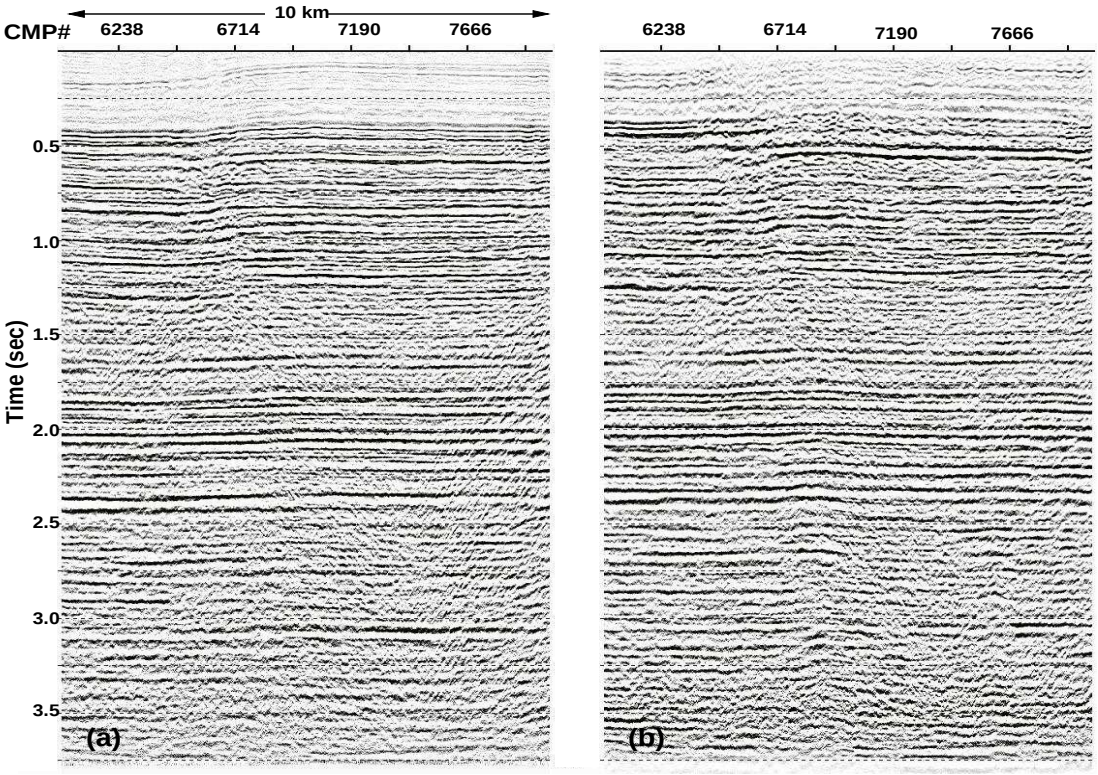

Figure 4.30. Section (a) shows the stack of line Zahar2 after applying the statics correction to a flat datum at 0 elevation. Section (b) shows the stack after redatuming to that datum.

Statics is not the best method to correct for the near-surface especially when the datum is deep or the velocity above the datum is large. In those cases, the best method is wave-field extrapolation (redatuming). The common-receiver gather shown in Figure 4.29 is an example of prestack data after redatuming to a flat datum at a depth of 200 m. Reflection hyperbolas are more continuous with less undulations due to the near-surface. Notice that shallow reflections are not well imaged after datuming due to low coverage.

Redatumed gathers were then sorted to CDP gathers, NMO corrected, and stacked. The final stack is shown in Figure 4.30 together with the statics-based stack for comparison. The horizons above 500 ms are not well imaged. The new section looks to have more continuous horizons and less multiples. See, for example, the time window between 1.25 and 2.25 sec. Structurally, this section is in agreement with the 200-m section shown in Figure 4.27. Below 1.5 sec, both sections show an anticlinal feature in the middle of the section.

Summary: The high-resolution near-surface velocity model was shown to be helpful in discriminating true low-relief structure from near-surface anomalies. For practical implementation, the shallow high-frequency data can be collected in discrete locations in the CDP mode. The velocity model is built be interpolating the velocity functions between the CDPs.

4.4 Line Dilam1

Data quality of prestack and poststack data in the previous case were excellent, which led to a coherent time image. The problem was in the long-period time structures, which might be near-surface related. Due to the low-

Table 4.5. Line Dilam1 acquisition parameters.

receiver interval	30 m
traces/shot	240
source interval	30 m
CDP interval	15 m
maximum fold	120
source type	sweep 10-100 Hz
sampling interval	4 ms

relief nature of the structures in this area, this ambiguity needs to be resolved before the first well is drilled. Line Dilam1 was acquired in an area where data quality is poor, which led to an uninterpretable stack section in some parts of the line.

4.4.1 Data Acquisition and Processing

Figure 4.31 shows an initial stack section of line Dilam1 after advanced processing. The processing included shot domain filtering and two passes of residual estimation and velocity analysis. This line crosses a highly-faulted graben in central Arabia below which the stack quality is poor. In both sides of the graben, however, the horizons are clearly interpretable. Incoherent stacking is caused by the complex near-surface, which causes severe statics problems. In addition, scattering caused by large rocks and sharp faults contributes to the problem. The production seismic line was acquired using the parameters in Table 4.5.

Several techniques were tried to better image the subsurface under the graben. These included statics-computation and wavefield extrapolation techniques. The improvements, however, were not significant. For example, Fig-

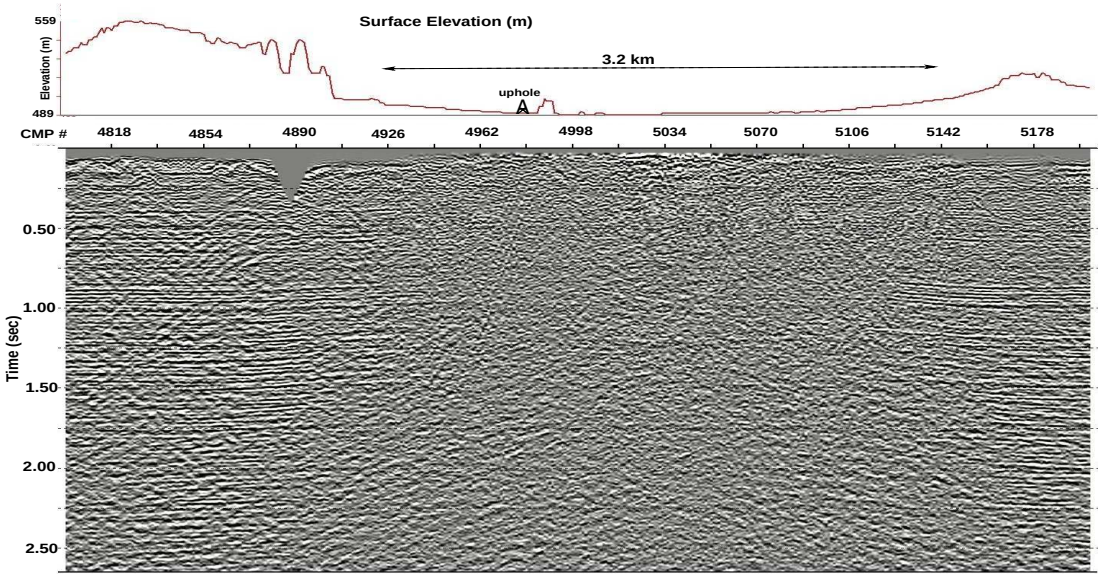

Figure 4.31. An initial stack of line Dilam1. The top panel shows the elevation profile and the location of the high-resolution line.

ure 4.32 shows the result of applying a datuming technique to correct for the near-surface (Alkhalifah and Bagaini, 2004). The technique worked well for most of the line, but failed to improve the stack under the graben, which is below point (3) in the figure. At this most challenging part of the line, I tested using high-resolution seismic data to build a near-surface velocity model.

4.4.2 High-Resolution Line

A high-resolution 2D seismic line was acquired using the parameters in Table 4.3. About 3.5 km of such data were acquired along the production line across the graben zone shown in Figure 4.31. Similar to production data, it is difficult to identify a clear and continuous reflector from the common-offset section shown in Figure 4.33. Moreover, it is difficult to identify coherent noise, such as surface waves. The frequency spectrum of the first-arrival window

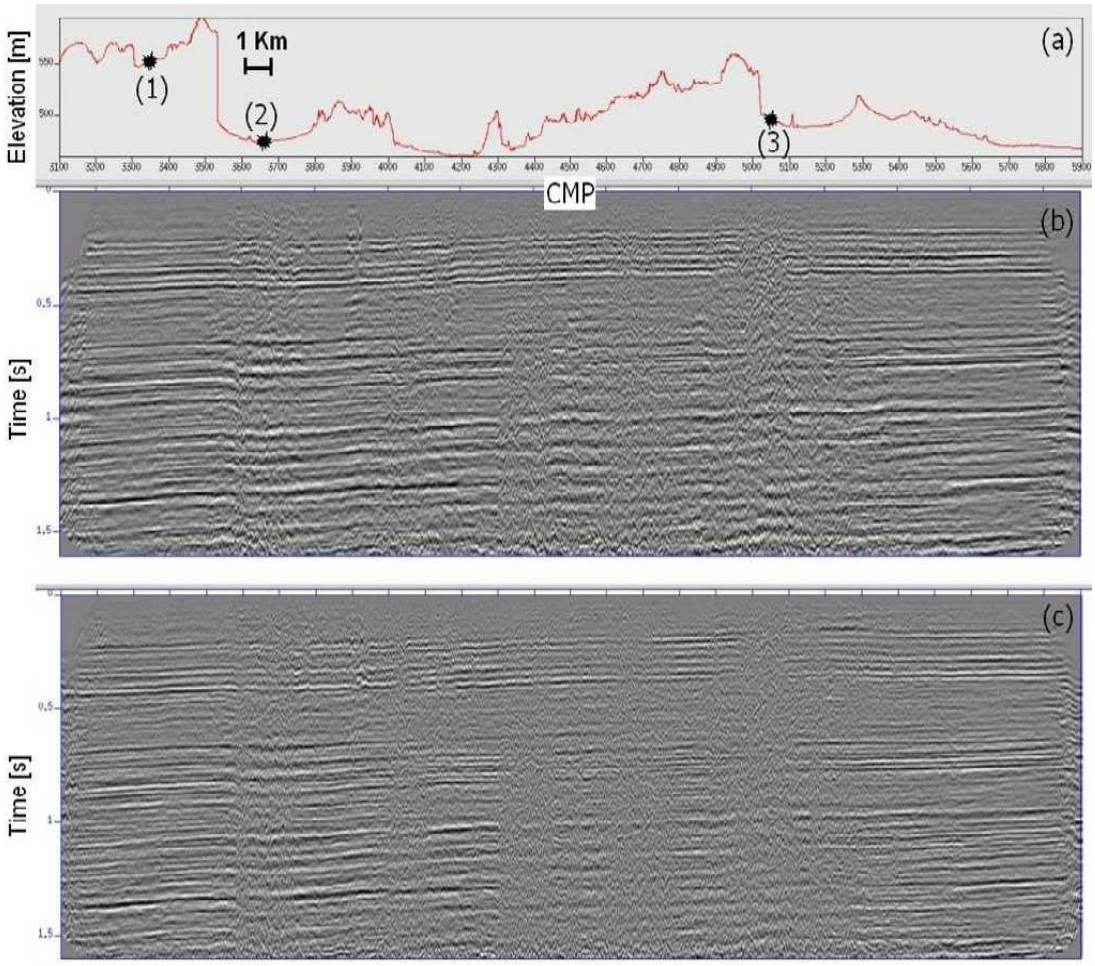

Figure 4.32. This figure was borrowed from Alklalifah and Bagaini (2004). It shows the result of applying a redatuming technique, named TDO, to correct for the near-surface. When compared to the production stack in panel (c), the improvements are clear. The method, however, failed near our zone of interest, under point (3).

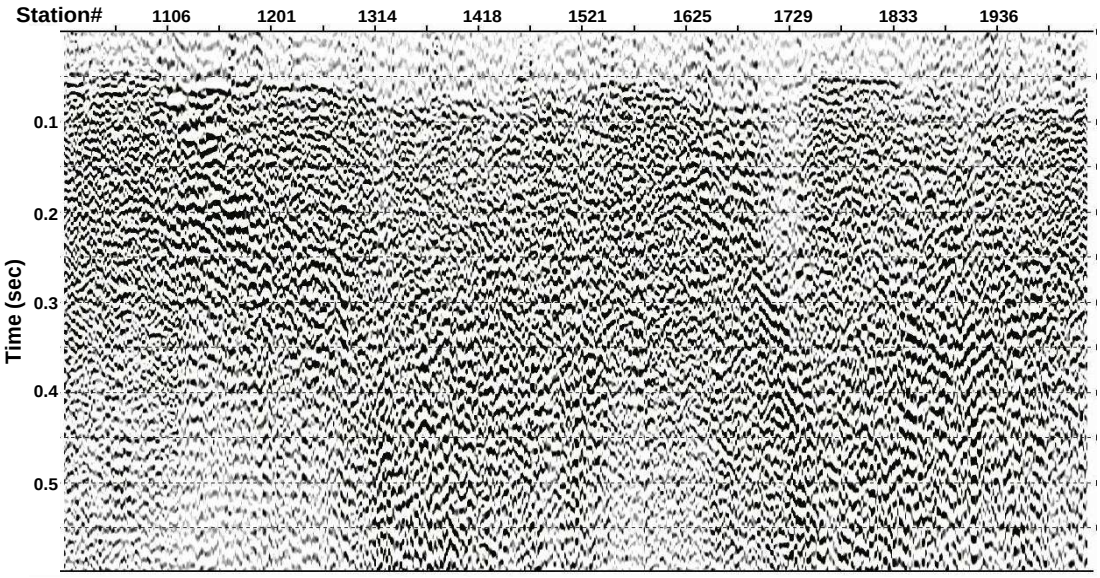

Figure 4.33. A common-offset gather for offset 100 m. The AGC gain was applied for the display purposes.

Figure 4.34 (bottom plot) shows that the maximum retrievable frequency is about 140 Hz. The frequency range of most of the data, however, is limited between 30 and 120 Hz (top plot).

The sample shot gather shown in Figure 4.35, shows that the only identifiable coherent events are direct, guided and ground-coupled air waves. No clear reflections can be identified although there is evidence of some at far offsets at time window 350 - 450 ms pointed to by the arrow.

Several processing techniques were used to produce an interpretable stack. The stacking velocities and residual were computed, in three iterations. The final stack shown in Figure 4.36 is still difficult to interpret. One process made a dramatic difference in stack quality; this is the trim statics. Trim statics are non-surface-consistent residual statics computed from the CDP gathers. These are the time residuals that produce the most coherent stack. Figure 4.37 shows

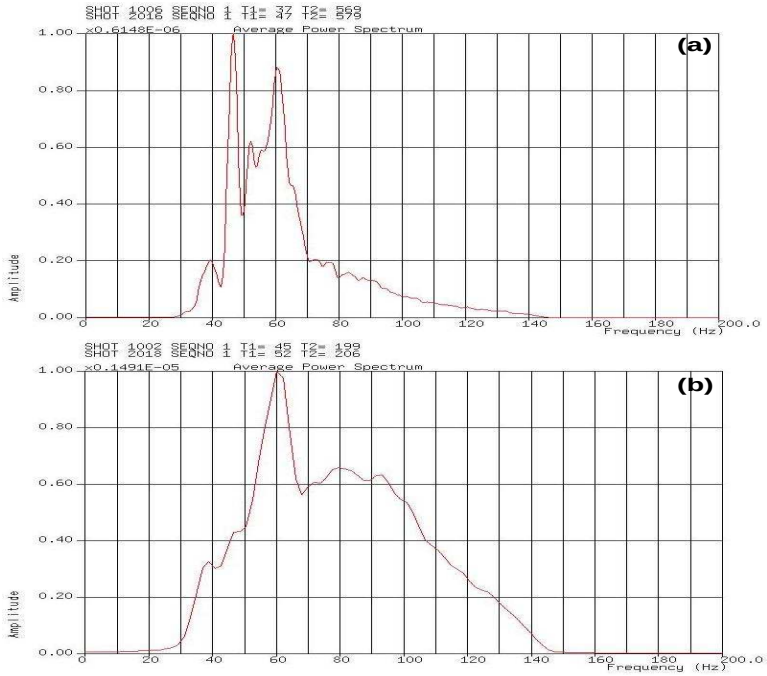

Figure 4.34. Frequency spectrum for two time windows in Figure 4.33. The top plot is the analysis of the whole time window, while the bottom plot is the analysis of the time window between 50 and 200 ms.

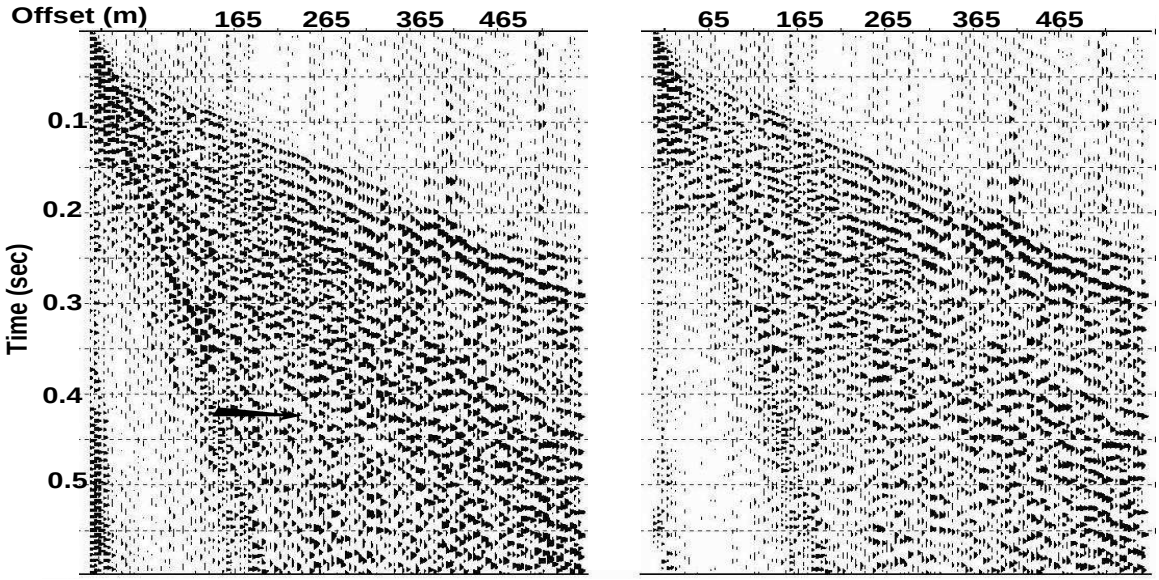

Figure 4.35. A sample shot gather after the $30-150$ Hz band-pass frequency filtering. The same gather is shown to the right after the local $f-k$ filtering. The arrow points to possible reflection events.

the clear improvements in stack quality. Several structural features, such as faults, can be interpreted from the section

4.4.3 Velocity Model and Statics Application

Our main objective is to estimate the near-surface velocity model. Similar to the high-resolution line in Zahar2, it is difficult to build a velocity model using horizon-based analysis. Therefore, the model was built using the stacking velocity analysis and Dix equation. The model is shown in Figures 4.38 and 4.39.

The velocity model was used to calculate datum statics to a flat datum below the surface. These values were then used to correct the production dataset. The final stack of line Diam1 is shown in Figure 4.40. This section is

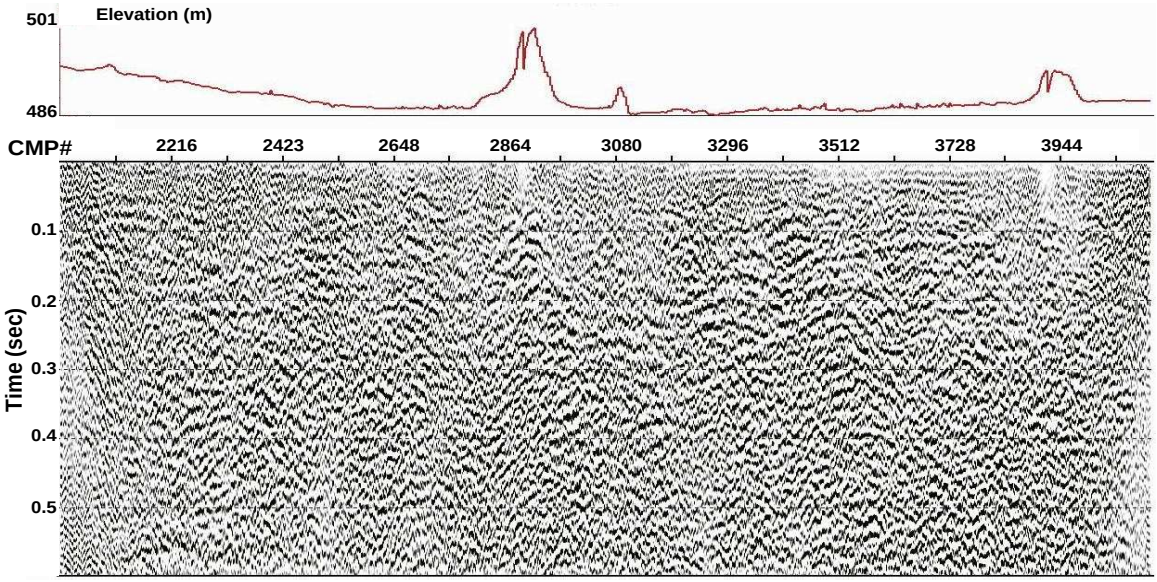

Figure 4.36. The final stack of the high-resolution line after three iterations of residual statics and velocity refinements.

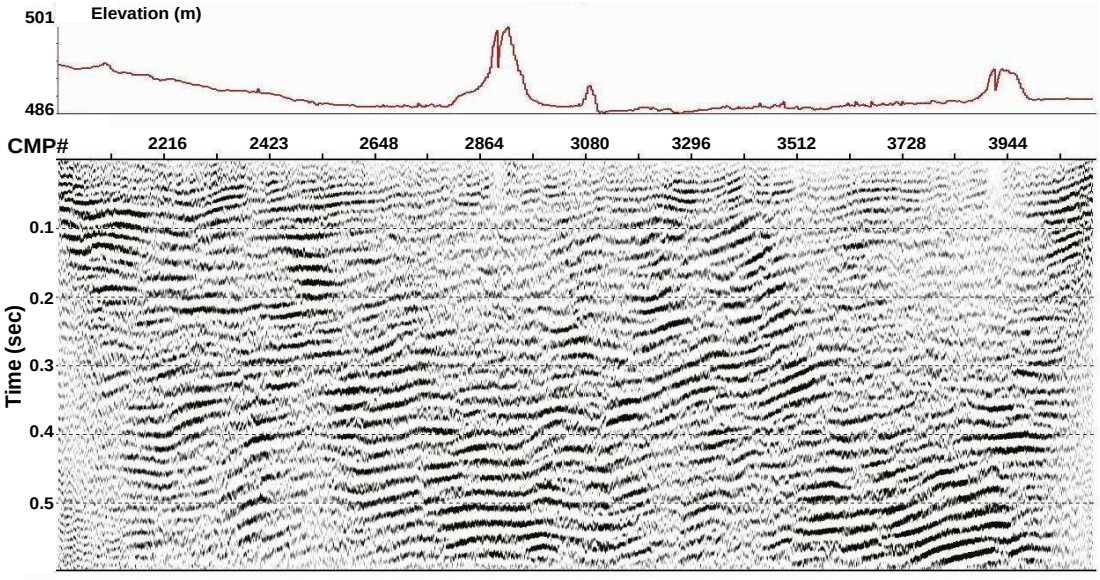

Figure 4.37. A final non-surface consistent statics were estimated and applied to the data which was used to produce the stack in Figure 4.36. Clearly, a great improvements were achieved.

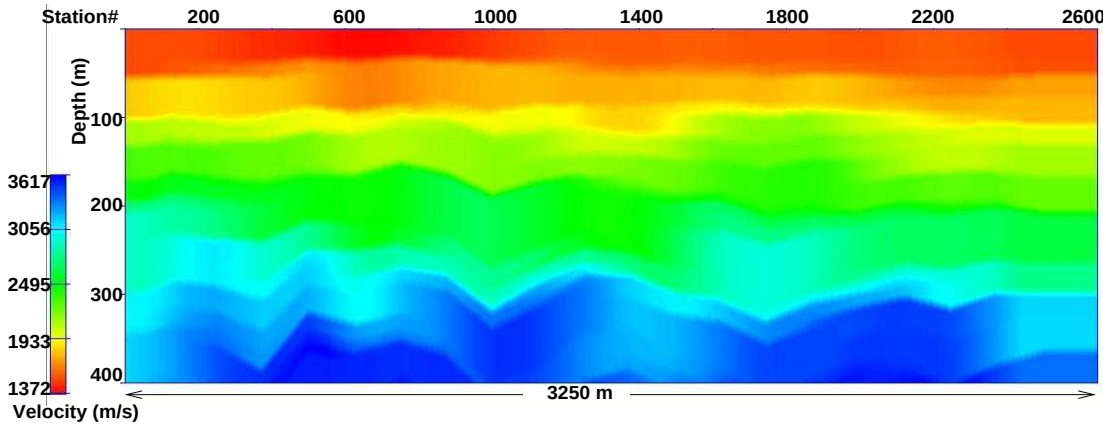

Figure 4.38. The final velocity model derived from the stacking velocity V_{stk}.

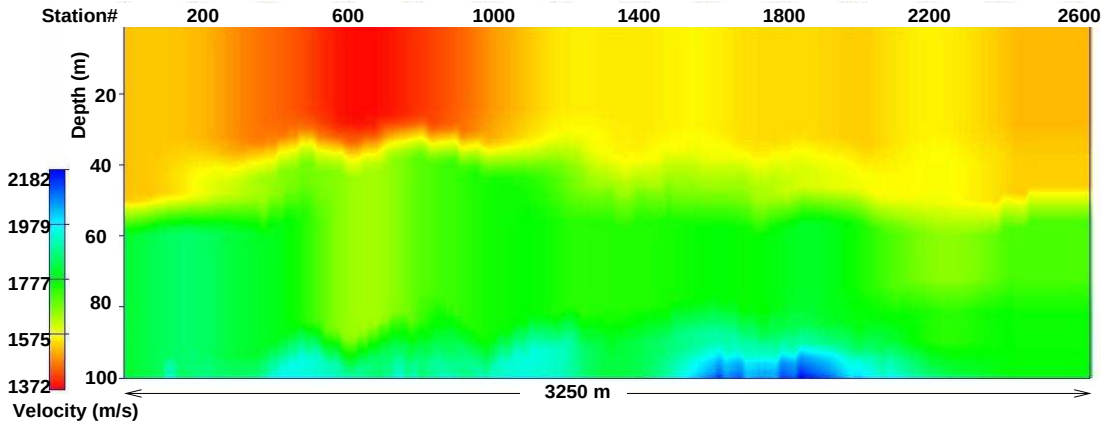

Figure 4.39. The upper 100 m of the model shown in Figure 4.38

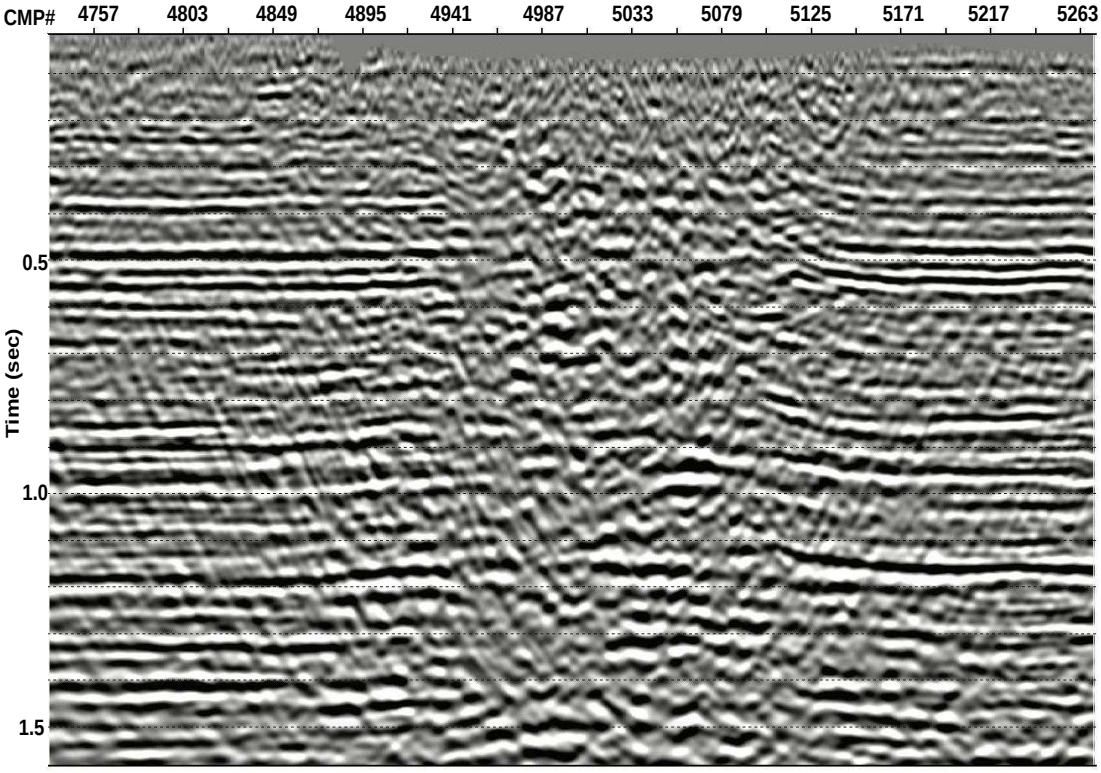

Figure 4.40. The final stack of the production line after applying the high-resolution statics.

superior when compared with the best available section shown in Figure 4.32. Deep events are more continuous with several possible faults interpreted.

Summary: In areas of strong scattering like this, it becomes difficult to acquire good high-resolution data. Nevertheless, the near-surface velocity model helped improve the time image. Several techniques were used to correct for the near-surface for this benchmarking line. By comparison, the high-resolution-data-based method was able to improve the data more than the other methods.

Chapter 5

COST-EFFECTIVE TECHNIQUES

5.1 Objective

In the last two chapters, use of high-resolution seismic data proved to deliver high-resolution near-surface velocity models that improved subsurface imaging of conventional exploration seismic. In this chapter, some solutions are discussed on how to make the model-building process more cost-effective. In particular, the discrete mode acquisition technique is discussed in the first section. In the second section, I discuss the use of a land streamer in data acquisition.

5.2 Introduction

High-resolution shallow seismic data proved to help building a more reliable high-resolution near-surface velocity model. Such a model is very important for conventional seismic data processing and interpretation and to obtain a more accurate subsurface image. The high-resolution-based model has the advantage of greater accuracy when compared to other techniques. However, it needs to be built in a more practical and cost-effective way.

The cost of acquiring such data has decreased dramatically since it was first introduced in the middle of the last century. But, deployment of sources and receivers at a meter spacing remains uneconomical. Here, I am suggesting

two ways in which the technique can be made even more cost-effective. In the first section, ultra high-resolution data are acquired at discrete points along the conventional exploration seismic line. The velocity functions from all these points are then interpolated to build a complete velocity model. In the second section, I discuss using a land-streamer to acquire high-resolution data. Some artifacts in the land-streamer data are also discussed.

5.3 Discrete CMP-Mode Acquisition

As described in the previous chapter, three continuous high-resolution lines were acquired and used to build the near-surface velocity model. Practically, however, there is probably no need to know the velocity every 1.25 m. Therefore, discrete CMP gathers could be acquired using the CMP acquisition mode every few kilometers, e.g. 2 km. A velocity function can be estimated at every CMP location using the ultra high-resolution data. The model, then, is built from interpolating all the velocity functions. This technique was implemented earlier for line Zahar1, using near high-resolution data.

To test this technique, near-surface velocity information was obtained from ultra high-resolution seismic data. The data were intentionally acquired close to an uphole. The velocity function was then compared to that obtained from the check-shot survey.

5.3.1 Field Data

The acquisition geometry and parameters were designed to image shallow depths of less than 500 m. The second column of Table 5.1 shows the acquisition parameters of the high-resolution data. The first column shows

parameter	conventional	high-resolution
receiver interval	30 m	1 m
traces/shot	240	112
source interval	30 m	5 m
spread type	split	split
CDP interval	15 m	1.25 m
maximum fold	120	22
sweep	$10 - 100$ Hz	$30 - 300$ Hz
sampling interval	4 ms	0.25 ms

Table 5.1. The acquisition parameters for line Dilam1 are compared to that for the ultra high-resolution data.

the conventional acquisition parameters of line Dilam1 on which the uphole was drilled. While the receivers were kept fixed, 24 shot gathers were acquired shooting between receivers. The location of the uphole, and therefore the ultra high-resolution line, is shown in Figure 4.31.

A raw shot gather from the high-resolution acquisition is shown in Figure 5.1. Reflections and refractions are clear in the optimal window between the direct-arrivals (B) and surface waves (A). An example is event (C), which is clear at far offset. Surface waves, with a velocity of about 400 m/s, have low amplitudes with no clear guided waves present.

5.3.2 Data Processing

The goal of data processing is to optimally remove noise and enhance reflections for an accurate velocity analysis. The estimated velocities are very sensitive to any processing step; therefore, the data need to be processed carefully. The processing sequence shown in Figure 5.2 was found to be effective in removing undesirable noise and enhancing the shallow reflections.

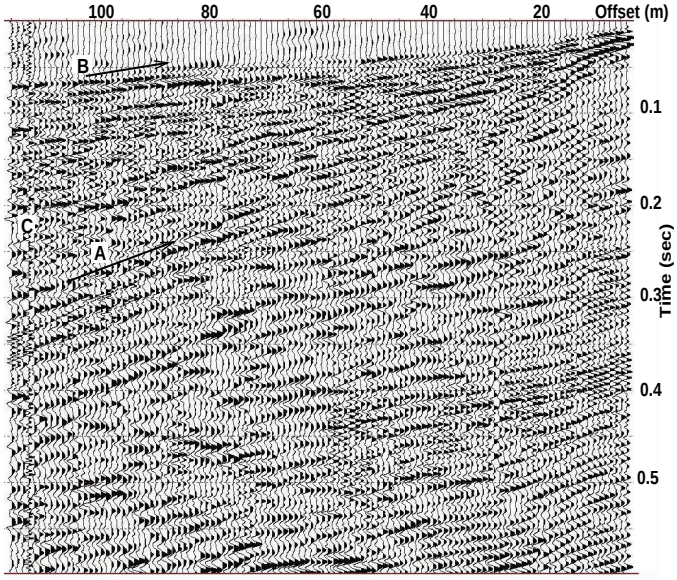

Figure 5.1. One shot gather from the ultra high-resolution dataset. A 100-ms AGC was applied for display purposes.

Unlike the conventional processing sequence, no datum statics are applied because the area is flat. Deconvolution did not enhance the shallow data, therefore, it was not used. Also, no residual statics were estimated because of the coarse 5-m source interval, compared to the 1-m receiver interval. The gathers have few traces from which to estimate the residuals.

Frequencies below 70 Hz were filtered out to help resolve different reflections. The left panels in Figures 5.3 and 5.4 show two of the processed shot gathers with maximum offset. The hyperbolic events marked by the purple lines are believed to be primary reflections.

5.3.3 Velocity Analysis Results

The panels in Figures 5.3 and 5.4 are typical velocity-analysis semblance panels generated using a commercial seismic processing software. The analysis

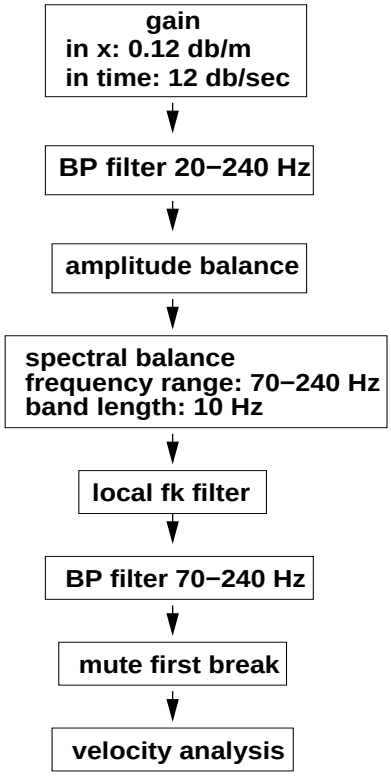

Figure 5.2. The processing sequence which was used to prepare the gathers for the velocity analysis.

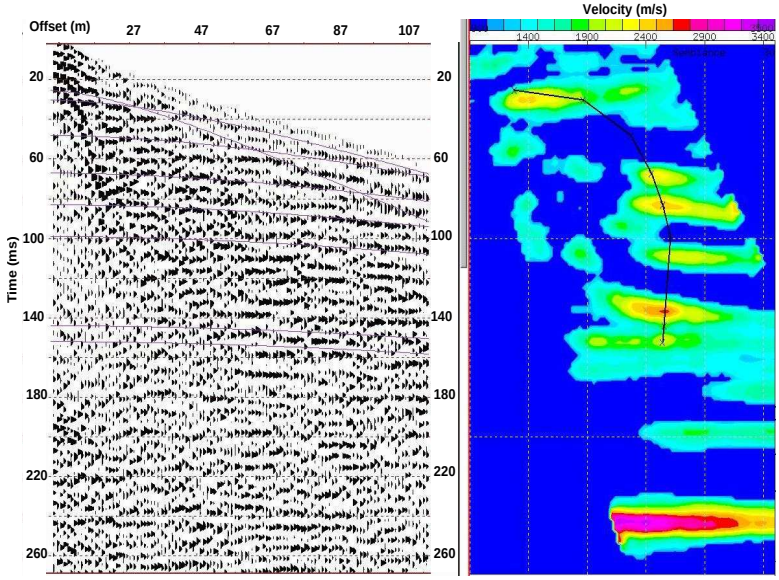

Figure 5.3. Velocity analysis of the first common-source gather of the receiver line.

is for two common-source gathers located at the two ends of the receiver line. The velocity analysis was performed on the shot domain because the offset increment is smaller than that in the CMP domain.

The semblance panels are similar, which indicates that velocities do not change noticeably within the receiver line. The small differences can be attributed to the scattered noise in the two locations. The semblances are very sensitive to the mute function, as was discussed by Miller (1992). So, the mute function or the stretch mute needs to be carefully chosen. The velocities were picked manually using the best-fit-hyperbola method on the gather. These velocities represent the velocity function at the mid-point. The accuracy of the picked velocities could have been improved if longer offsets were acquired.

For flat layers and small offsets, the stacking velocity, V_{stk}, is a good approximation to the rms velocity, V_{rms}, (Yilmaz, 1987). The Dix equation

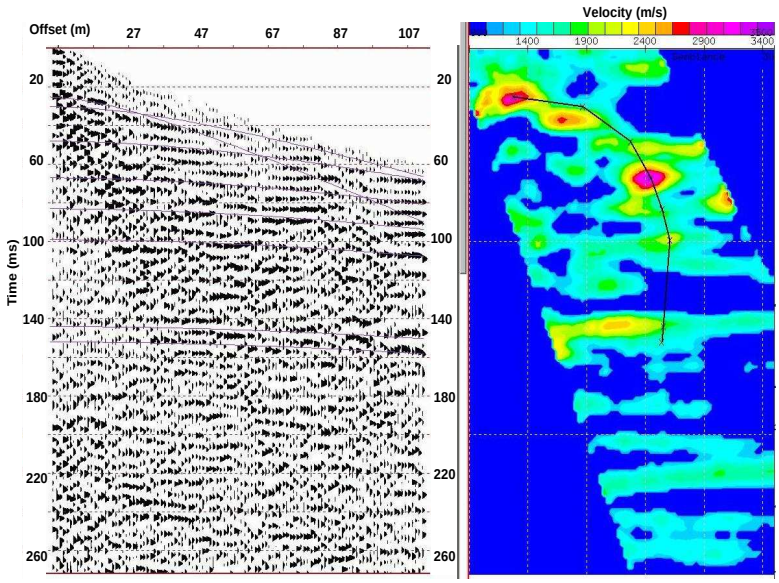

Figure 5.4. Velocity analysis of the last common-source gather of the receiver line.

can be used to convert the stacking velocities to interval velocities, V_{int}. The average velocities, V_{avg}, can then be computed from V_{int}. The plot in Figure 5.5 shows the estimated V_{rms} and V_{avg} when compared to the exact velocities obtained from the uphole. The V_{rms} curves match each other well above depth of 110 m. The maximum error is about 170 m/s. Similar results were obtained by Hunter et al. (1998). The picked velocity points were converted to depth and plotted against the one-way times in Figure 5.6. For comparison, the exact points from the check-shot survey are also posted on the same plot. The maximum time error is about 3 ms, which is within the first-break time picking error. From the synthetic data analysis above, the error in V_{rms} estimation was about $\pm$100 m/s. For real data, this might be slightly larger because of noise contamination. The reflections in the first 200 ms interfere with other wave modes such as refraction and guided waves. In addition, the small recorded

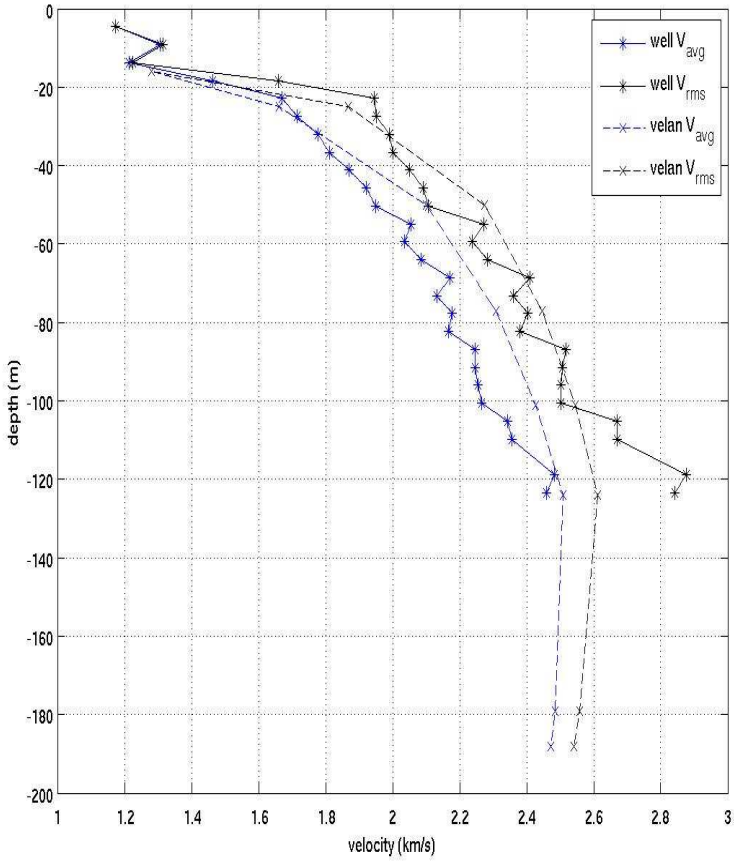

Figure 5.5. A comparison of the estimated velocities and the exact check-shot-based velocities.

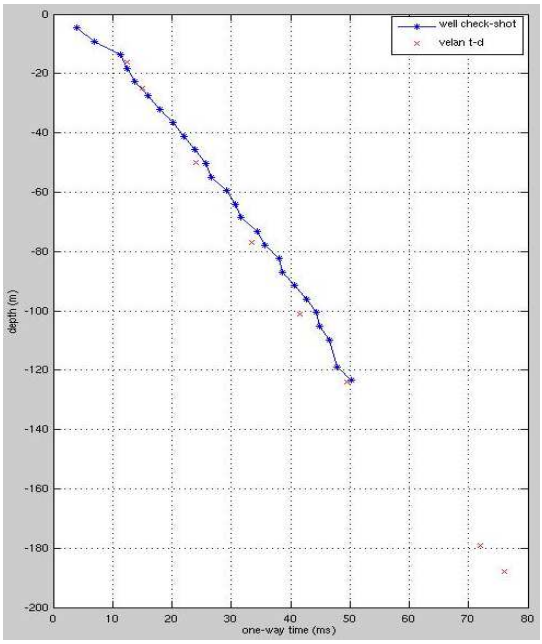

Figure 5.6. The picked points in Figure 5.5 are converted to depth and plotted together with the check-shot data points.

offset range, the NMO stretch, and the lack of statics correction limit the accuracy of the estimated velocities.

In addition to using hyperbolic moveout of reflected events to estimate the velocities, here refraction tomography was also tested. The first breaks in the sample shot gather shown in Figure 5.1 were fairly easy to pick. The picks were used to estimate the near-surface velocity model. Turning-ray refraction tomography was used in the first-break inversion. The maximum offset is 120 m; therefore, the maximum expected depth of penetration is about 30 m. The area between the first and the last shot point was discretized using cells with a size of 40 m in the x direction and 1 m in the z direction, this is almost a 1-D model. The output velocity model and the corresponding ray density plot are shown in Figure 5.7. The model shows that the velocity does not

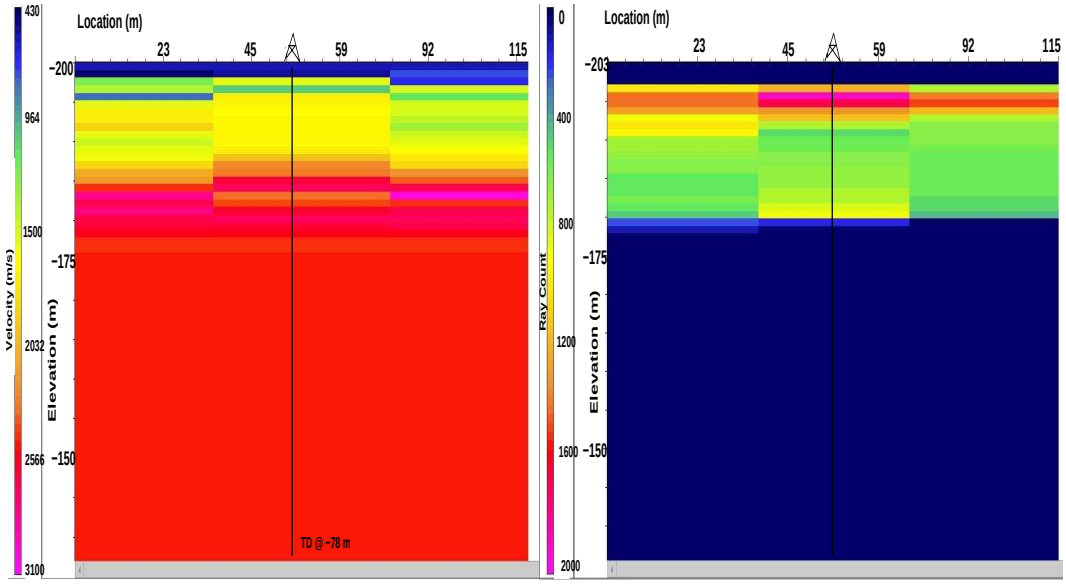

Figure 5.7. The output velocity model of turning-ray tomography for an almost 1-D model. Ray count at every cell is shown the right plot.

always increase with depth. There are some minor differences between the three columns in the figure.

To verify the accuracy of this model, the velocity function at the uphole location was used to compute the vertical time from the surface to every 1 m in depth. The calculated T-D pairs were then plotted in Figure 5.8, together with the measured T-D pairs from a check-shot survey. The model is accurate at a depth range 10 to 50 m. At greater depth, the model is not accurate because of lack of ray penetration. Also, the method is not accurate enough to resolve the very-near-surface velocities.

5.3.4 Stacking

The data were sorted into CMP gathers, NMO corrected, and then stacked. The NMO correction is too small for the velocity variation to make appreciable

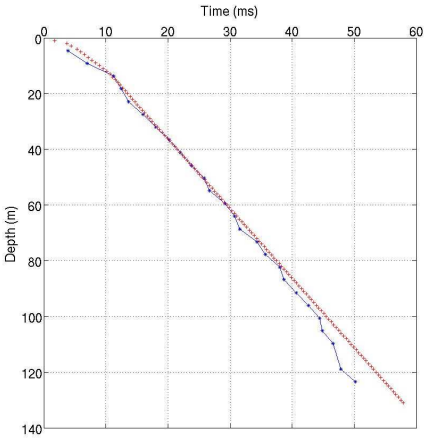

Figure 5.8. The calculated T-D pairs from the velocity function at the uphole location in Figure 5.7. The blue stars are the measured T-D pairs from the check-shot survey.

differences in stack quality. The stack is shown in Figure 5.9 with a maximum fold of 22 traces. When compared to the stack of the conventional data in Figure 4.31, some shallow horizons are now clear. For the acquisition parameters, see Table 5.1.

Summary: Using the CMP-mode in high-resolution data acquisition, accurate velocity model can be built at the location of every CMP. Besides the conventional hyperbolic moveout analysis of reflection events, the refraction tomography was used to estimate the model. Refraction tomography model, however, is not as deep as the reflection model.

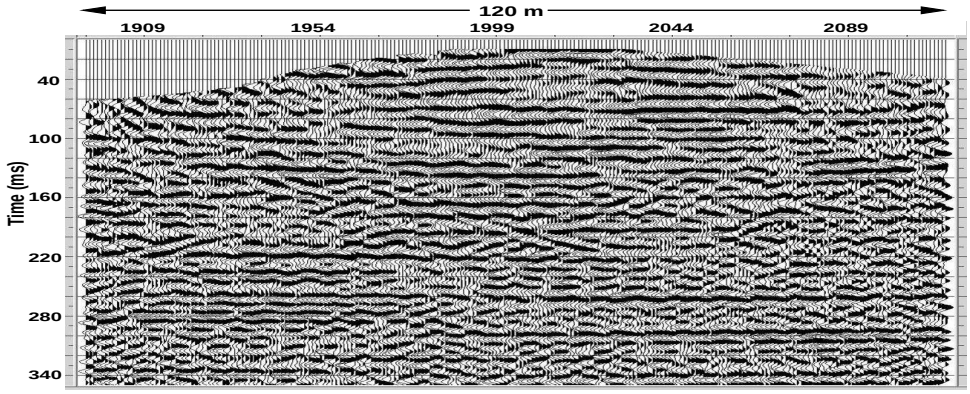

Figure 5.9. The stack of the high-resolution dataset.

5.4 Land Streamer

To make the process of acquiring high-resolution data for building the near-surface velocity model more efficient, one approach is using a land streamer. The main purpose of using a land streamer is to make the process of collecting high-resolution seismic data more cost-effective.

The idea of using the land streamer in land seismic surveying is to mimic the acquisition efficiency of marine surveying techniques. In general, a land streamer consists of a series of geophones, or hydrophones, usually mounted on base plates, which are connected to each other and towed behind a vehicle. Many case histories have been published about designing and using this technique in near-surface geophysics (Miller et al., 1984, Van der Veen et al., 1998, and Tsoflias et al., 2007). The general conclusion is that no significant differences were observed between conventional data collected by planted geophones and land streamer data.

In this section, the performance of a land streamer over sand dunes is analyzed. The characteristics of the plate-mounted signal are compared to the

conventionally recorded signals.

Two experiments were conducted using three types of plates. The first experiment was conducted in a sand box in a controlled environment. The second experiment was conducted in the field over thin sand at the KU campus. A third experiment was conducted over large sand dunes in Riyadh (Saudi Arabia). In this experiment seven slightly-modified designs were tested using a short geophone spread. In the following three sections, the datasets are displayed and analyzed.

5.4.1 Sand Box Experiment

Three types of plates were tested, all of which have the dimension of 20 cm x 13 cm. Two of the plates had a simple rectangular shape, 2-cm thick, with a flat bottom and made of steel and aluminum. These are the plates numbered 1 and 3 in Table 5.2. Their weights were 3 kg, and 1.5 kg, respectively. Plate number 2 has a W shape and was fabricated out of a 2-mm steel sheet with a total weight of 1 kg.

This experiment was conducted in an indoor 4 m x 4 m sand box at the University of Kansas campus. Three geophones, for the three components, were screwed to the top of each of the three plates. Another six geophones with spikes were planted in the sand. Three of them were planted on the surface, plate 4 in the table, and the other three were planted 5 cm below the surface, plate 5. A single 5-kg hammer was used as a source. Every three hammer strikes were vertically stacked and recorded as a 15-channel gather. Table 5.2 shows the channel number and color code for every trace in this dataset.

plate #	type	motion	channel	color code
1	steel plate	horizontal X	1	red
		horizontal Y	2	red
		vertical Z	3	red
2	W-shape plate	horizontal X	4	yellow
		horizontal Y	5	yellow
		vertical Z	6	yellow
3	aluminum plate	horizontal X	7	green
		horizontal Y	8	green
		vertical Z	9	green
4	surface spike	horizontal X	10	blue
		horizontal Y	11	blue
		vertical Z	12	blue
5	buried spike	horizontal X	13	black
		horizontal Y	14	black
		vertical Z	15	black

Table 5.2. Channel and color assignments of the sand-box dataset.

Figures 5.10 and 5.11 show two analysis plots for two time windows. The top panels show the recorded traces. The frequency spectra of these traces are shown in the bottom panels. The color codes used are shown in Table 5.2. The left panels show the signal detected by the horizontal X geophones (SH motion). The middle panels show the horizontal Y geophones (SV motion). The right panels show the vertical Z geophones (compressional motion). Channel number 7 is noisy because the screw is loose. There is a good correlation between the plate-mounted geophones. Similarly, there is a good correlation between the two planted geophones. This is true for the three recorded motions, X, Y, and Z. The correlation between the mounted and the planted geophones, however, varies in time. In general, the correlation improves with time for the three motion components.

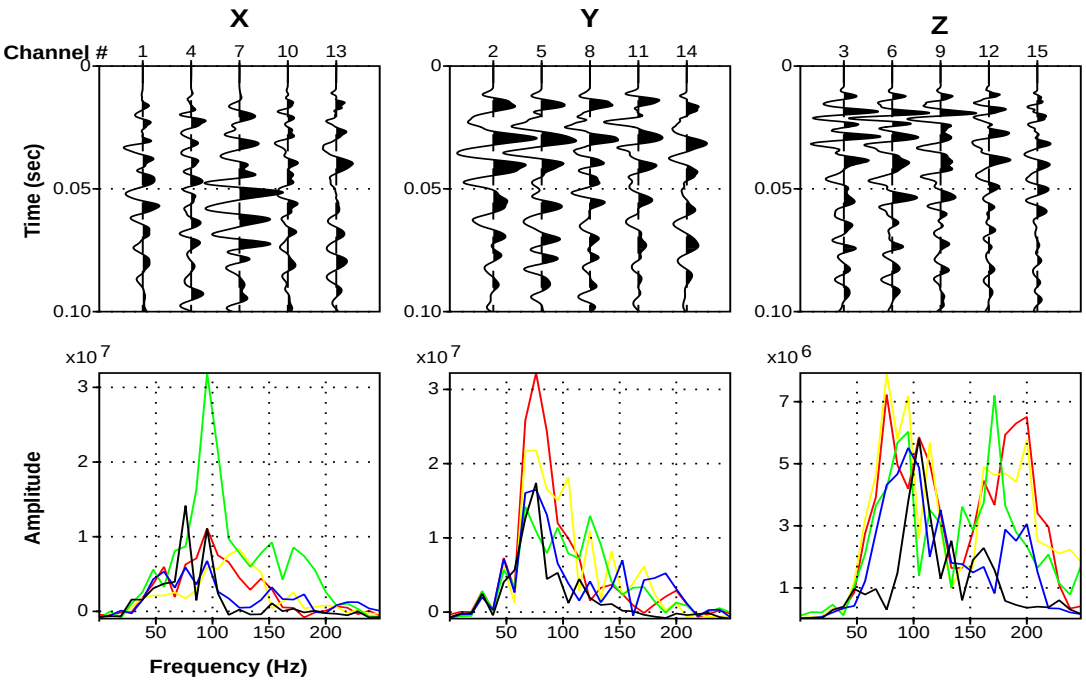

Figure 5.10. A time window of the recorded 15 channels shown in Table 5.2. The frequency spectrum for every trace is also shown, see the table for the color codes.

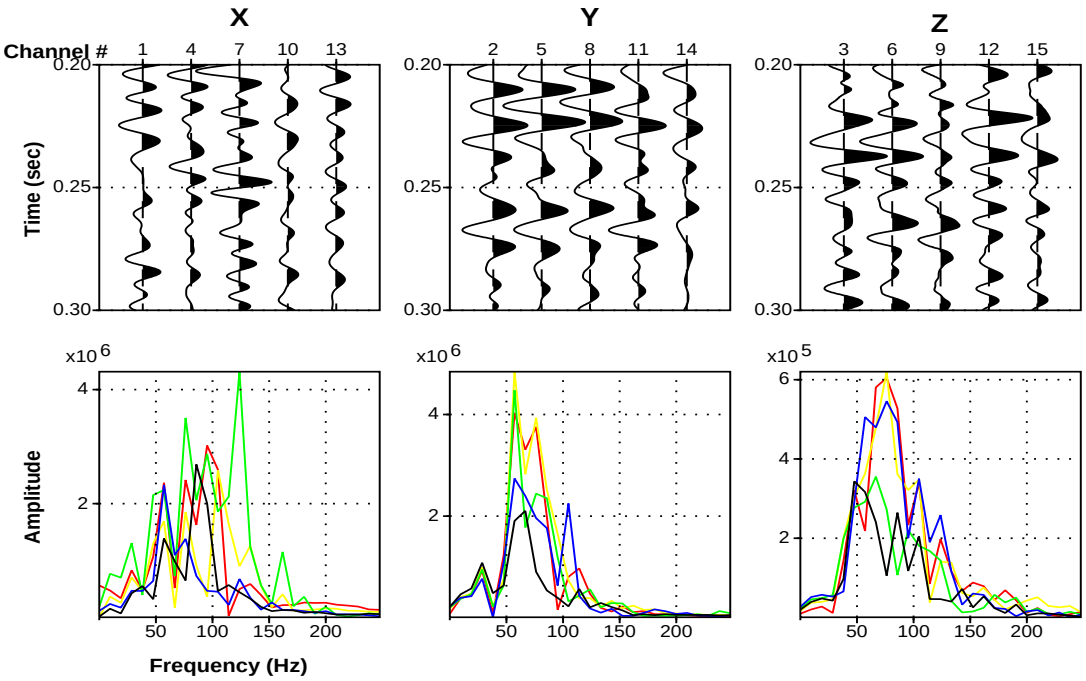

Figure 5.11. Similar to Figure 5.10, but for a deeper time window.

The differences in the frequency-spectrum plots in Figure 5.11 are less than those in Figure 5.10. This indicates that most of the differences are due to the first arrivals. In particular, the Z-components of the mounted geophones have larger amplitude in the frequency range 150 to 250 Hz than the planted geophones. From all the spectrum plots in the two figures, plates 1 and 2 recorded the best frequency response followed by plate 3. So, a better signal was recorded using plate-mounted geophones. However, the response of the plate-geophones lag by about 3 ms.

Another way of comparing traces and measure the degree of similarity is through cross correlation. Figure 5.12 displays the cross correlation functions of the five Z-component channels 3, 6, 9, 12, and 15. There is a good correlation among the mounted geophones, see traces 2, 3 and 8. Traces 4, 9 and 13

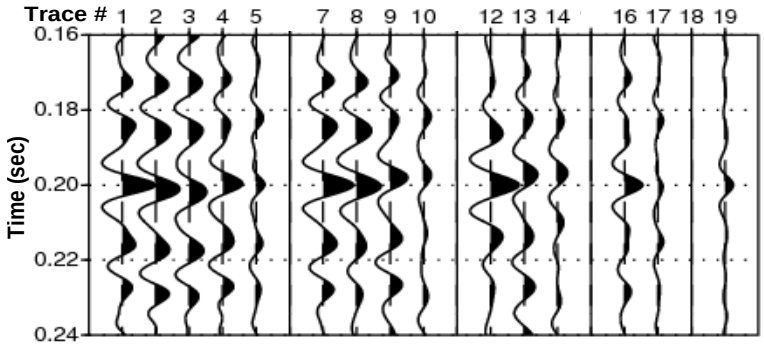

Figure 5.12. The cross correlation functions between the Z-component channels shown in Table 5.3. The correlation window is 200 ms, centered between 0.1 and 0.3 sec.

Traces	correlate channel	with channels
1 to 5	3	3, 6, 9, 12, and 15
7 to 10	6	6, 9, 12, and 15
12 to 14	9	9, 12, and 15
16 to 17	12	12, and 15
19	15	15

Table 5.3. Trace number assignments of the cross correlation functions shown in Figure 5.12.

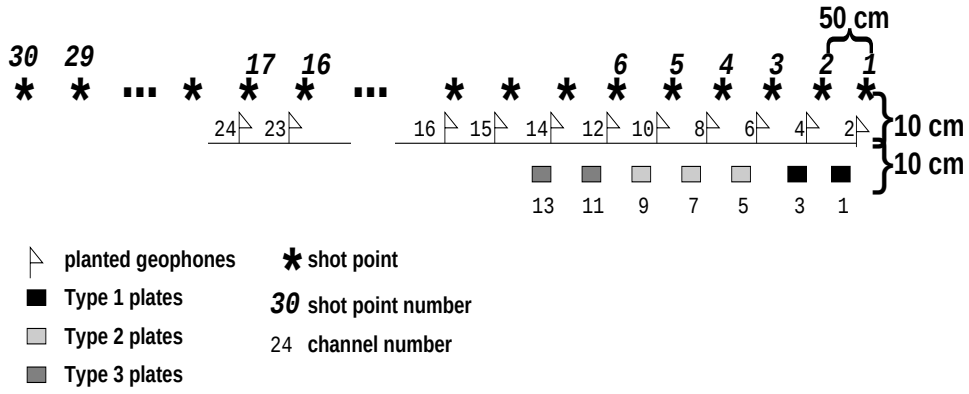

Figure 5.13. Acquisition geometry of Experiment 1.

show that there is a good correlation between the surface geophone and the mounted geophones. The buried geophone is not as well correlated as the surface geophone. A similar result was observed by Tsoflias et al. (2007). The time lag can clearly be observed in traces 9, 10, 13, and 14. Among the five vertical geophones, the steel plate 1 (trace 5 in Figure 5.12)has the least lag relative to the planted geophones.

5.4.2 Field Experiment 1

The objective of this experiment is to repeat the sand-box experiment, but in a more realistic environment. Wind is an extra factor affecting the recorded signal quality. On the other hand, there are no side walls to reflect the waves. Here, only the vertical Z-component was recorded. The signals recorded using plate-mounted geophones were compared with that recorded using conventionally planted geophones.

The experiment was conducted at the University of Kansas campus in Lawrence (Kansas). The terrain is covered by compact soil with only a 20-cm thick dry-sand layer at the surface. Figure 5.13 shows the acquisition

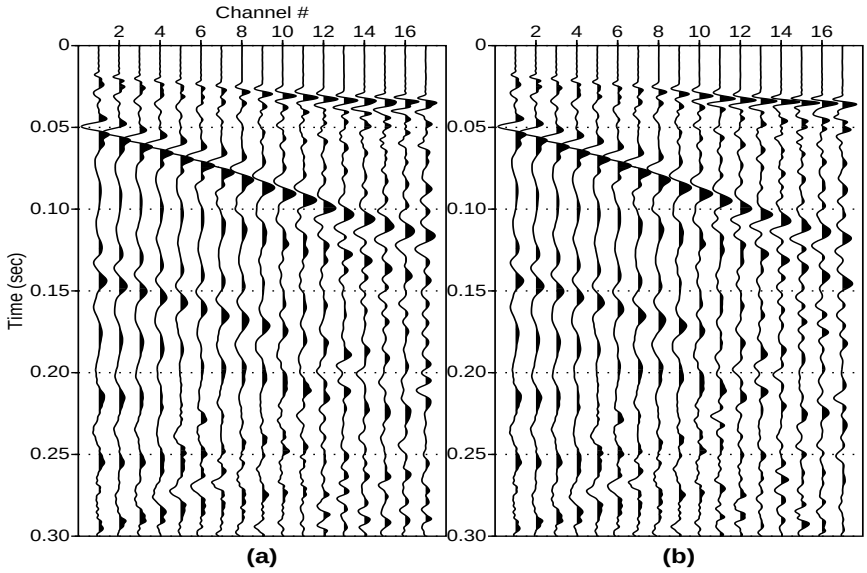

Figure 5.14. Common source gather number 30, the first 10 traces in both gathers are from the compact-soil geophones. The last 7 traces in gather (a) are from the dry-sand planted geophones, while those in gather (b) are from the plate-mounted geophones as in Figure 5.13.

geometry of the experiment. Seven plate-mounted geophones were placed on top of the flat surface at a 0.5-m spacing. Two heavy-steel plates (type 1), three light-steel (W-shaped) plates (type 2), and two aluminum plates (type 3) were placed next to each other (Table 5.2). Next to them (10 cm away), seven geophones were planted in the sand. The remaining 10 geophones were planted in the compact soil to extend the spread to 17 stations. The source type was a 22-mm caliber gun. Thirty source points were shot at a 0.5-m spacing with an offset of 10 cm from the receiver line.

Shot number 30 in Figure 5.14 was split into two gathers, (a) and (b). The first 10 traces are common in both gathers. They were recoded by the compact-soil geophones. The last 7 traces in gather (a) are from the sand-

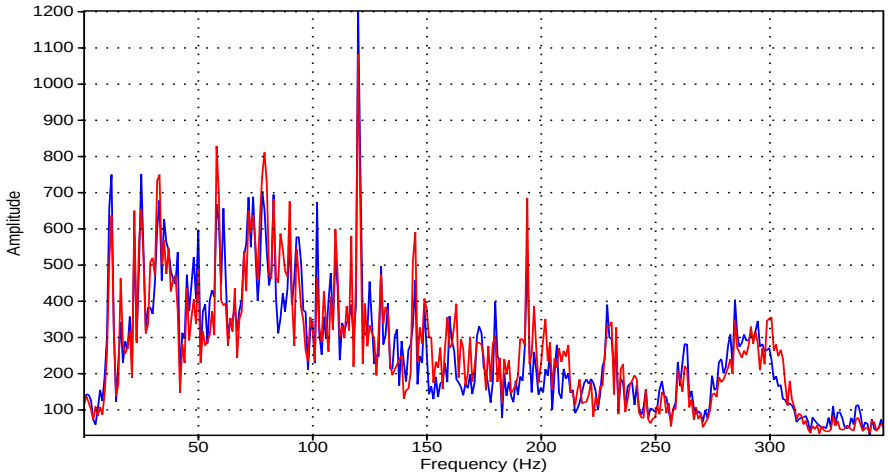

Figure 5.15. Average frequency spectrum of last seven traces in the gathers shown in Figure 5.14. The spectrum of the sand-planted geophones is in blue, wile the spectrum of the plate-mounted geophones is in red.

planted geophones. The last 7 traces in gather (b) are from the plate-mounted geophones. Direct and surface waves are clear in both gathers with a velocity of 550 m/s and 300 m/s, respectively.

By visual comparison, the signal recorded using the two different geophones are very similar. In fact, the amplitude spectra shown in Figure 5.15 show an almost identical frequency content. However, the first-arrival signal of the plate-mounted geophones have a wider frequency bandwidth and larger amplitude. This is not very clear in the all-trace-window amplitude spectra shown in Figure 5.15.

Besides the first-arrival advantage of the plate-mounted geophone, another one was clear after simple data processing. The shot gathers in Figure 5.14 were band-pass filtered from 150 - 300 Hz, and then NMO-corrected

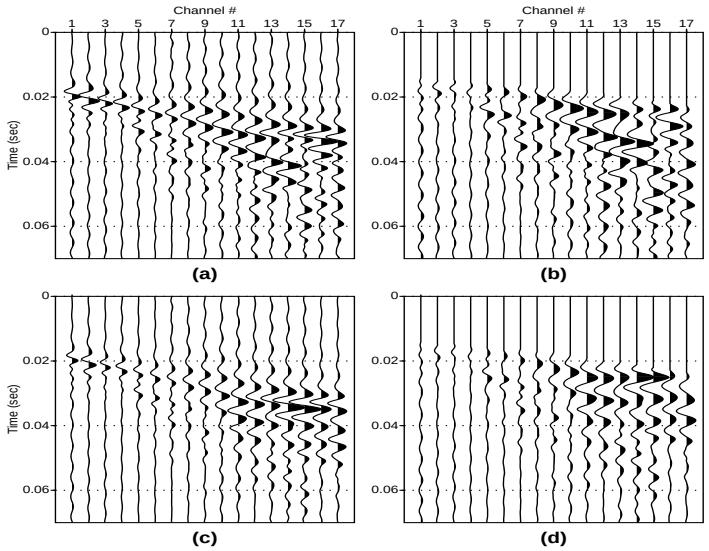

Figure 5.16. The two shot gathers in Figure 5.14 are displayed here after frequency band-pass filtering. The top gathers are for the sand-planted geophones, while the bottom gathers are for plate-mounted geophones . Gathers (b) and (d) are after the NMO correction using a velocity of 550 m/s.

using a velocity of 550 m/s. The results are shown in Figure 5.16. After the moveout correction, the event at about 20 ms is the direct head wave. The event at 40 ms is probably a reflection event. This event is clearer in the plate-mounted geophone dataset (Figure 5.16-(d)).

One of the objectives of this experiment is to compare the coupling of different streamer plate types with conventional geophones. The optimal design should record the signal without any plate-related artifacts. The common-receiver gathers in Figures 5.17, 5.18, and 5.19 are for the plate type 1, 2, and 3, respectively. Among the three plates, the geophone mounted on the aluminum plate introduced the least distortion to the recorded signal. The near-source plate-mounted geophones recorded the signal without amplitude clipping.

The comparison between the plate-mounted and the sand-planted signals shows a time-variant lag of the plate-mounted geophone. This can clearly be seen in the one-trace comparisons shown in Figure 5.20. The plot shows a comparison for shot point 1 (a), 18 (b), and 30 (c). The recorded signals from three plate-mounted geophones (red traces) are displayed on top of their adjacent sand-planted geophones (blue traces). The traces are displayed without any gain. Since the amplitude decays rapidly in time, two separate windows are shown for every trace. The match between the blue and red traces is excellent. The time shifts and the minor differences in amplitudes are due to differences in the geophones response. This will be discussed theoretically in the last section of this chapter. Another possible causes to the observed differences are the responses to the geophones to the horizontally-propagating waves such as surface waves.

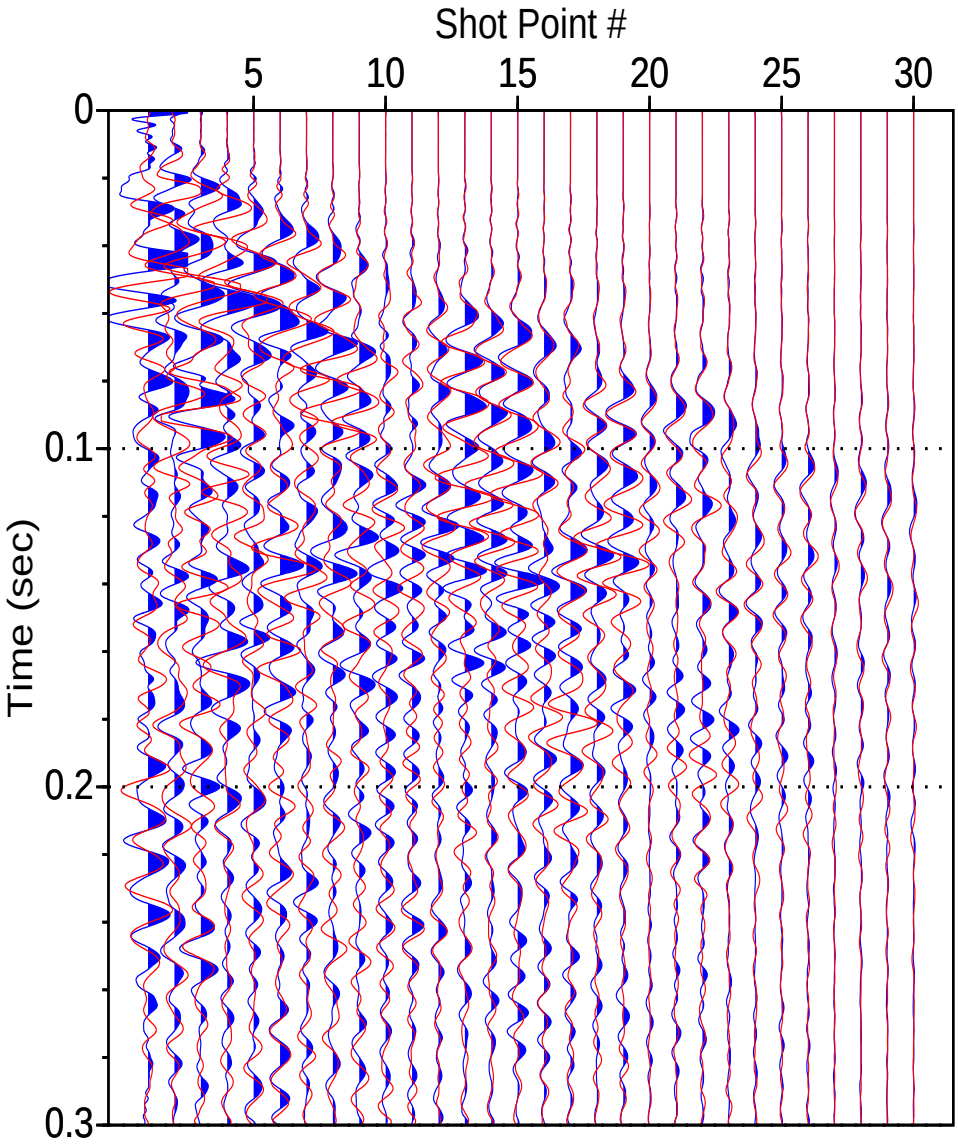

Figure 5.17. Two common-receiver gathers; the red traces are from a heavy-steel-plate-mounted geophone, while the blue traces are from the geophone planted next to the plate.

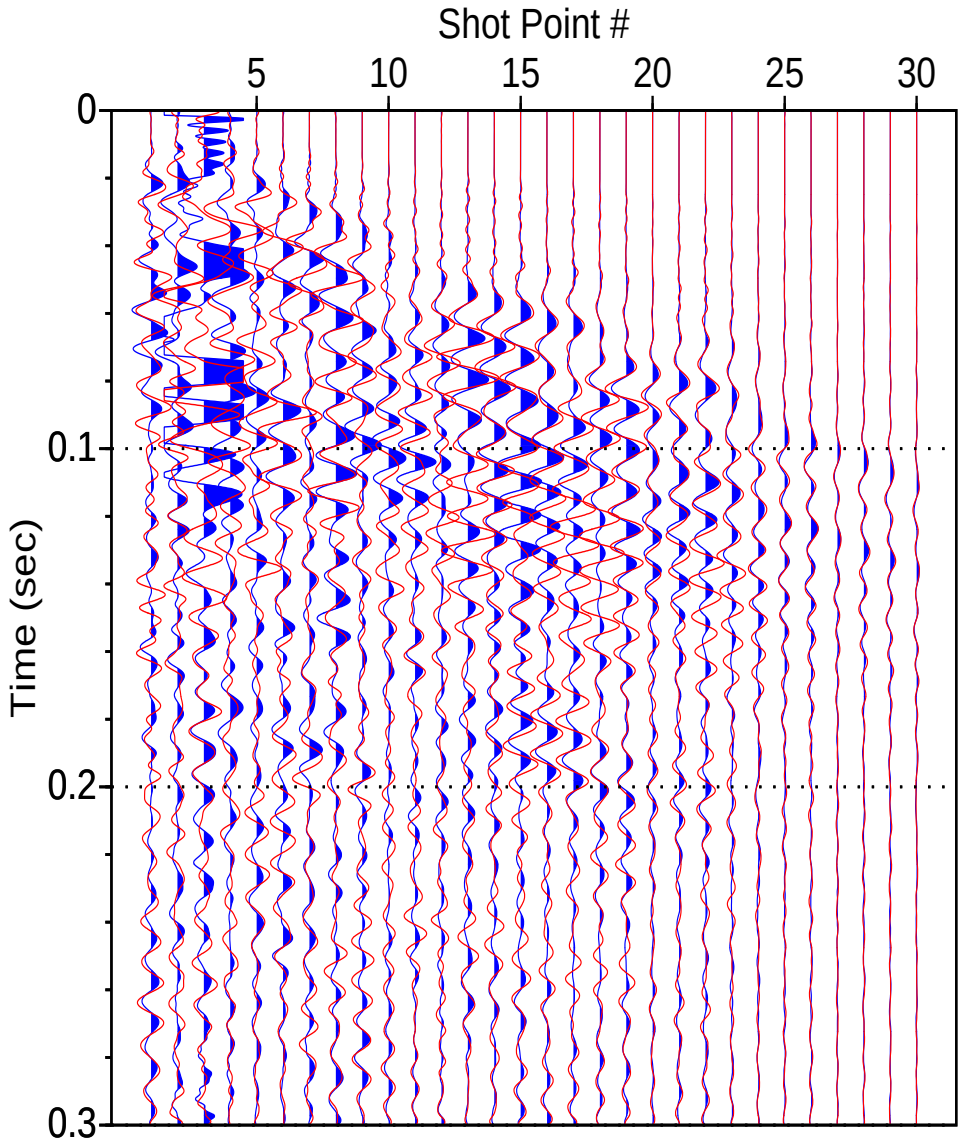

Figure 5.18. Two common-receiver gathers; the red traces are from a light-steel-plate-mounted geophone, while the blue traces are from the geophone planted next to the plate.

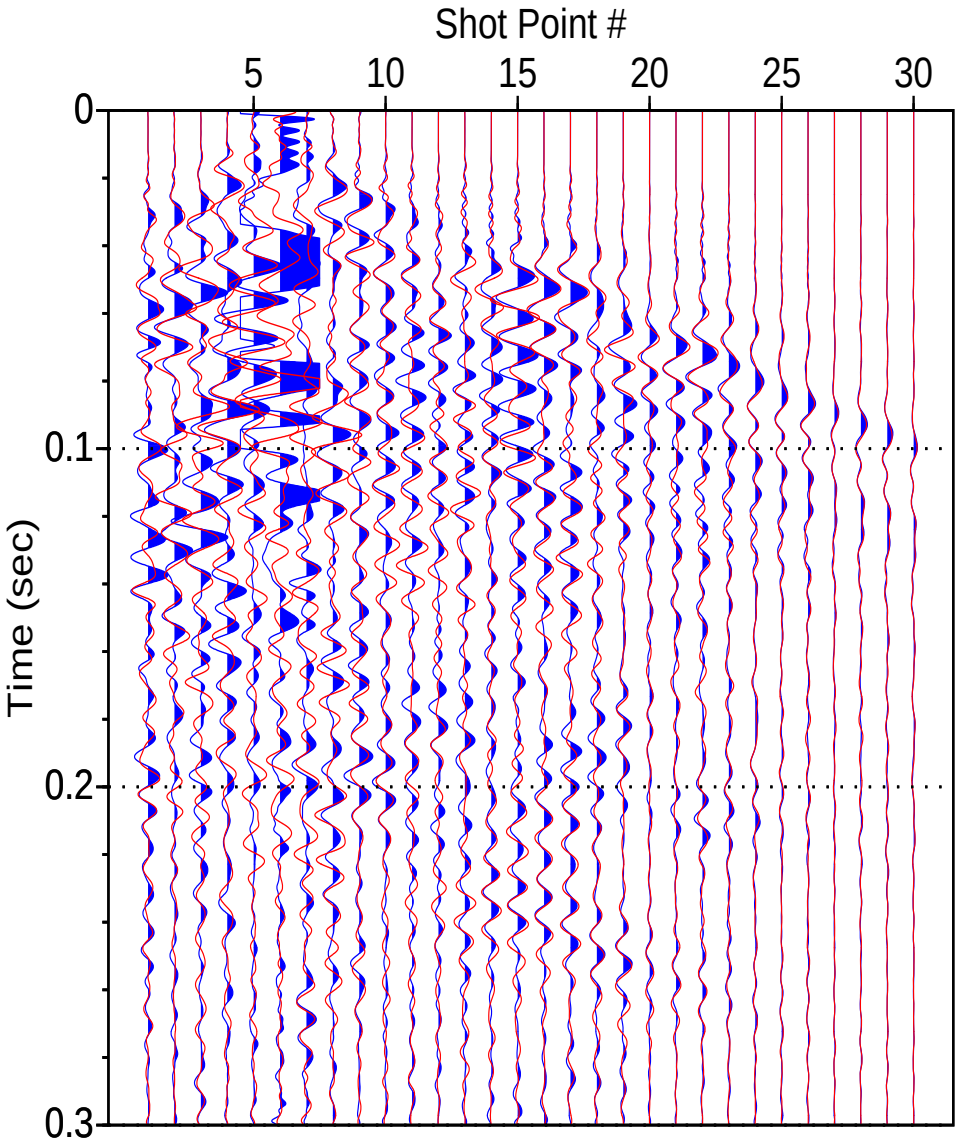

Figure 5.19. Two common-receiver gathers; the red traces are from an aluminum-plate-mounted geophone, while the blue traces are from the geophone planted next to the plate.

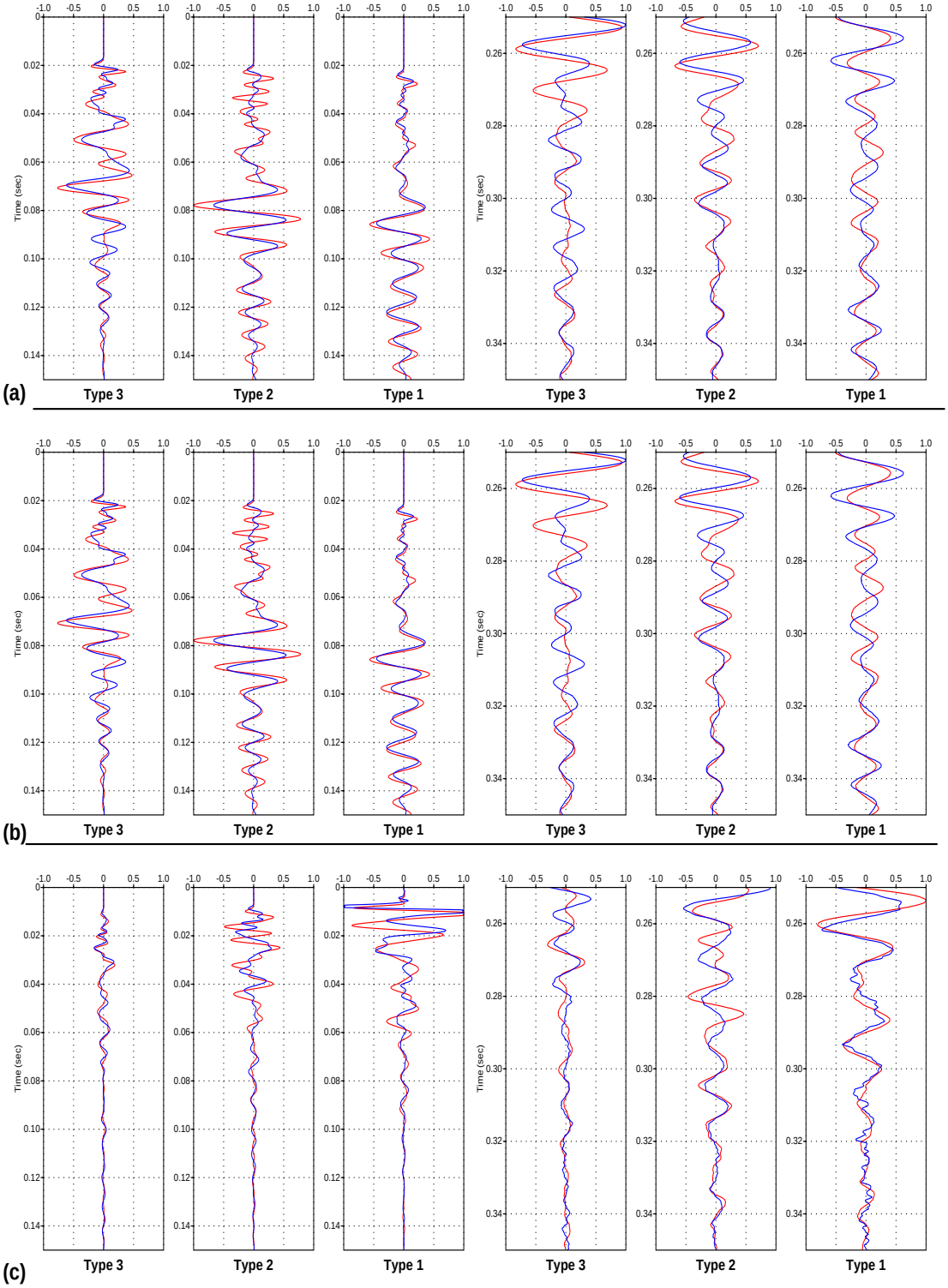

Figure 5.20. Six traces from shot point 1 (a), 18 (b), and 30 (c). Plate-mounted traces (in red) are displayed on top of their adjacent sand-planted traces (in blue). Two windows of the traces are displayed without any gain.

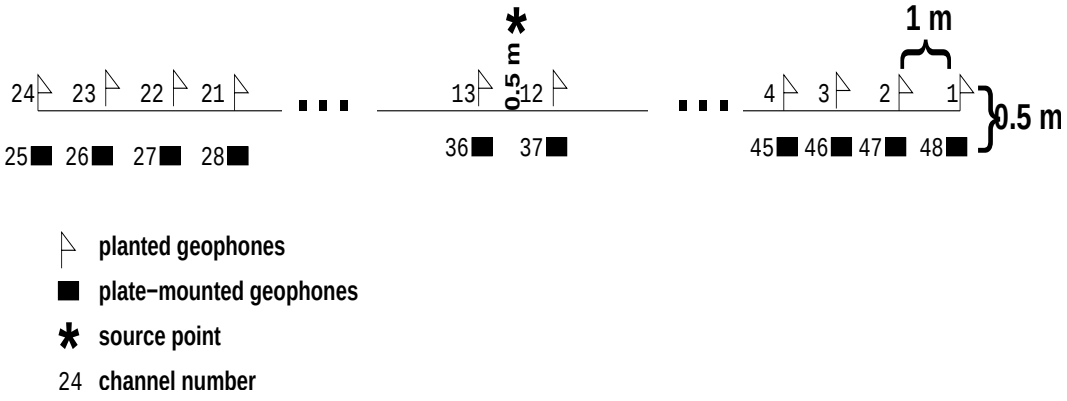

Figure 5.21. Acquisition geometry of field experiment 2 in Riyadh (Saudi Arabia).

5.4.3 Field Experiment 2

The second field experiment was conducted over a 20-m-high sand dune in Riyadh (Saudi Arabia). The objective of this experiment was to study the response of plate-mounted geophones over dry sand. This is similar to KANSAS field experiment 1, but in a desert environment. One common-source gather was acquired using a 3-kg hammer in the middle of two geophone spreads as shown in Figure 5.21. The near-source channels 1 to 24 were for the sand-planted geophones, while the far channels 25 to 48 recorded the signal from the plate-mounted geophones. All the plates in this experiment were of type 2 or slightly-modified designs.

Figure 5.22 shows the data from the two spreads after t^2 gain and 200-ms AGC. The slope of the first-arrival is 380 m/s, which is similar to the speed of sound waves in air, 340 m/s. The top soil is dry and soft sand, which explains such a low velocity. Another clear event is the surface wave with a velocity of 250 m/s.

Similar to the data in field experiment 1, the amplitudes of the plate-

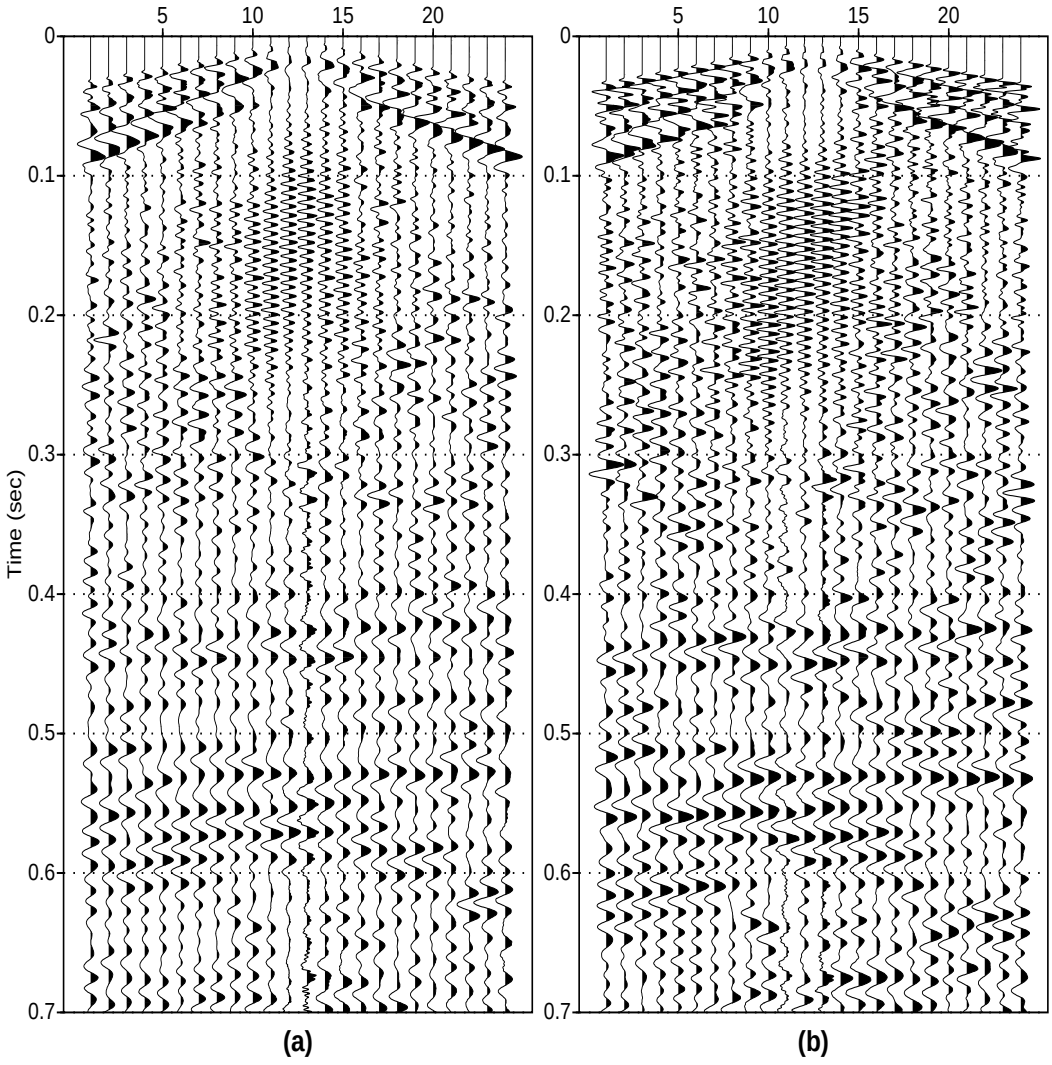

Figure 5.22. A single shot gather after t^2 gain and 100-ms AGC. Traces in (a) are from the sand-planted geophones, while traces in (b) are from the plate-mounted geophones.

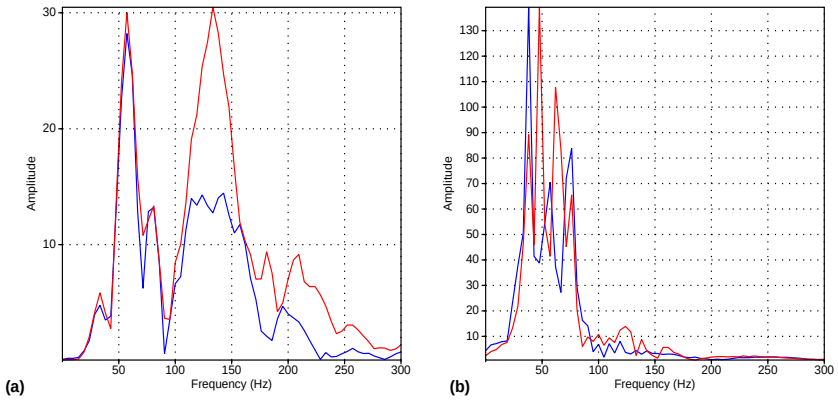

Figure 5.23. Frequency spectrum of trace 24 for two time windows, (a) 0-200 ms and (b) 400-600 ms. The blue graph is for the sand-planted geophone, while the red graph is for the plate-mounted geophone.

mounted geophones, in general, are larger than the sand-planted ones. Based on the data characteristics, three time windows can be identified in the shot record. The first window extends from the first arrivals to about 100 ms. This window is dominated by surface and direct waves. The frequency spectrum of channel 24 at two time windows, shown in Figure 5.23, show that the signal in this window has a broader band. Frequencies over 100 Hz most probably are from the direct arrivals. In the second zone, 100-400 ms, there are no clear reflections. The high-frequency oscillations of the near-source traces are artifacts due to to the bandwidth limitations of the 40-Hz geophones. This window is well within the noise cone. In the third zone, below 400 ms, there are clear deep reflections. The maximum time move-out is small because the maximum offset is only 5.5 m. The spectrum in Figure 5.23-(b) shows the similarity of the recorded signal by both geophones with a bandwidth of 20-90 Hz.

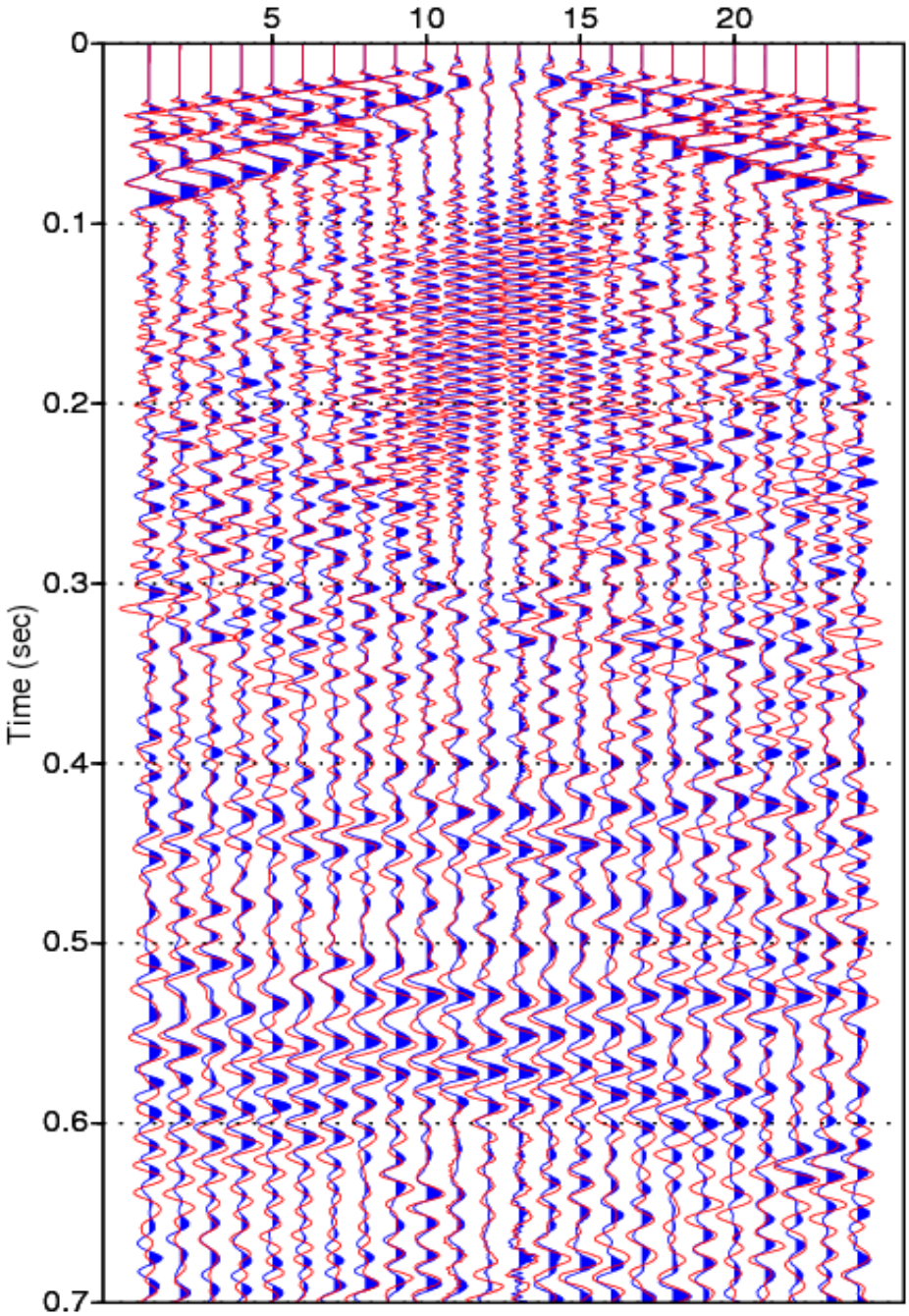

Figure 5.24. The same gathers shown in Figure 5.22 plotted over each other. Gather (a) is plotted in blue, while gather (b) is plotted in red.

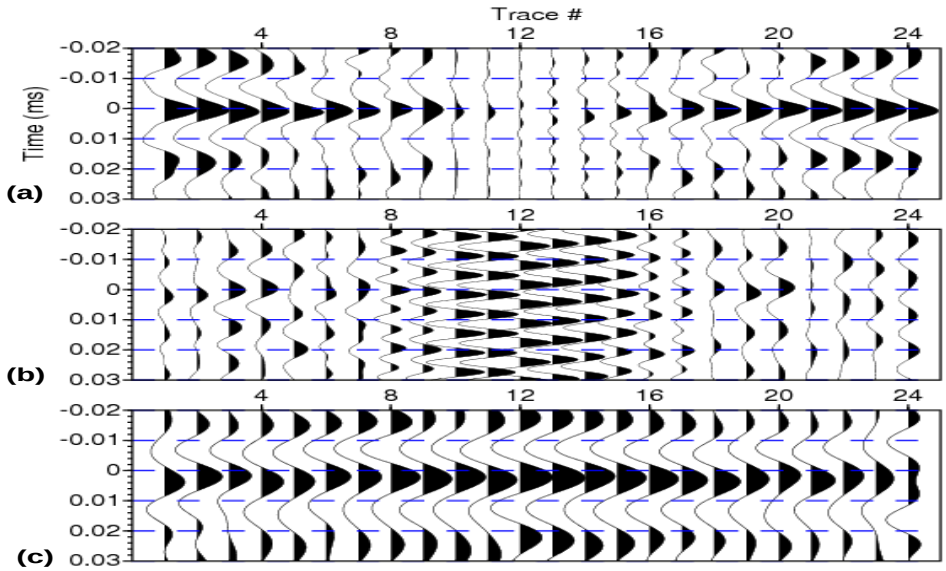

Figure 5.25. The cross-correlation functions between the sand-planted geophones and the plat-mounted geophones for the time window 0 - 100 ms (a), 100 - 300 ms (b), and 400 - 600 ms (c).

The two gathers in Figure 5.22 are plotted on top of each other in Figure 5.24. There is an excellent match between the two gathers in the first and the third time windows. The noise, the ground-coupled air waves, and the geophone artifacts in the second window are clearly different for the two geophones: the mounted and the planted. Similar to the data in the sand-box and the field experiment 1, a time-variant lag of about 1 to 5 ms is observed between the two geophones.

These visual observations are confirmed by cross correlating the signal from the sand-planted geophone with the signal from the adjacent plate-mounted geophone. Figure 5.25 shows the cross-correlation functions for the three time windows. The correlations in the first window are excellent with almost zero time lag except for few near-source traces. The poor correlations

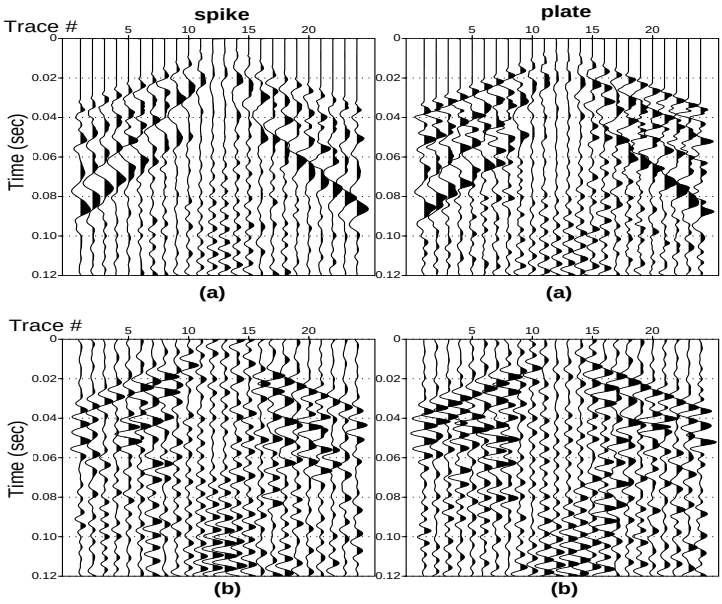

Figure 5.26. The first 120 ms of the gathers in Figure 5.22. The gathers after the gain in (a) are plotted in (b) after the 80-250-Hz band-pass filter.

of the second window are as expected. The signals in the third time window correlate well except for a variable time lag. The lag is about 5 ms in trace 1 and 1 ms in trace 22.

In field experiment 1, the near-surface reflectors were more clearly imaged using plate-mounted geophones. This interesting result is confirmed again in this experiment and shown in Figure 5.26. After a 80-250-Hz band-pass filter, a number of reflections become clear. The hyperbolas at 40 and 80 ms are two examples where the reflections in the plate-mounted gather (b) are more continuous than in the sand-planted gather. Since these are only two examples and can not be generalized everywhere, it is sufficient to say that the data from a land-streamer are at least comparable to the conventional geophone data.

Our main objective is to estimate the near-surface velocity using high-

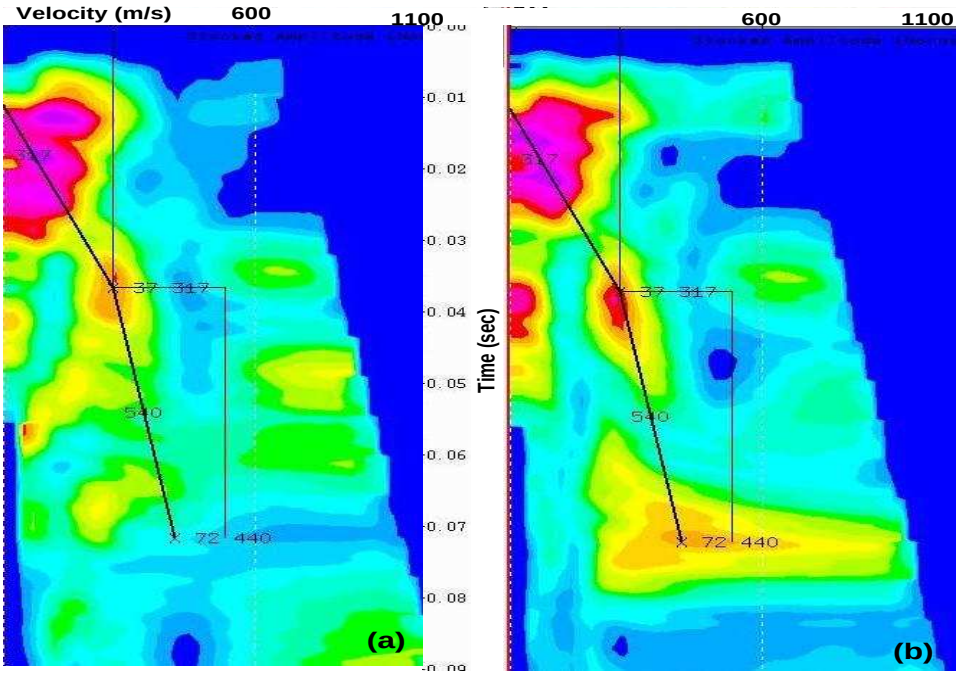

Figure 5.27. The velocity analysis panels for the two gathers shown in Figure 5.26. Panel (a) is for the sand-planted gather, and (b) is for the plate-mounted gather.

resolution data collected by a land streamer. The velocity analysis panels in Figure 5.27 show that using plate-mounted geophones improved the coherency panels and therefore our ability to estimate the velocity. Any analyst can identify two distinct reflections, at 37 ms and at 72 ms. These are associated with the base of the top dry sand and base of the sand dune. The velocity of layer 1 is 317 m/s, which agrees reasonably well with the first-arrival velocity of 340 m/s. The interval velocity of the second layer is 540 m/s. This two-layer sand-dune model is consistent with our understanding to the geological layering in this area.

5.4.4 Geophone-Ground Coupling

From the sand box and the two field experiments, is apparent that there are time variant lags of the plate-mounted geophones relative to the sand-planted geophones. Geophone-ground coupling is probably the cause of this time lag. Geophone-ground coupling refers to the accuracy with which the geophones measure the actual ground motion. Geophone coupling can be modeled as a system of two damped springs (Krohn, 1984) as shown in Figure 5.28. The output geophone voltage is proportional to the difference between the velocity of the geophone case V_g and the velocity of the coil V_{cl}.

V_{cl} depends on the resonant frequency, f_g, and the damping factor,η_g, for the internal spring of the geophone as expressed in equation 5.1. The equation represents the frequency response of a geophone, where f_g and η_g are the two main characteristics of every manufactured geophone (Krohn, 1984).

$$H_g(f) = \frac{-(f/f_g)^2}{1 \; - \; (f/f_g)^2 \; + \; j\eta_g(f/f_g)}. \tag{5.1}$$

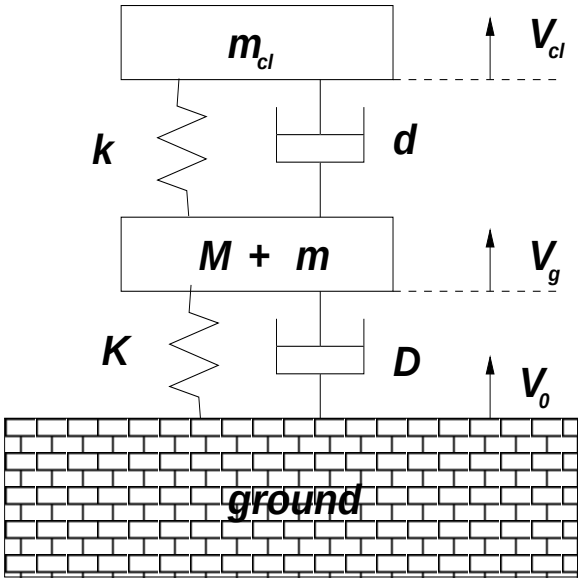

Figure 5.28. Mathematical model for geophone coupling; m_{cl}: mass of coil, k spring constant of coil, d: damping constant of coil, m mass of geophone case, M: mass of coupling, K spring constant of coupling, D: damping constant of coupling, V_{cl}: velocity of coil, V_g: velocity of geophone case, V_0: velocity of ground.

Geophones with natural frequency of 40 Hz or 100 Hz are usually used in shallow seismic surveys. Total damping of 70% is acceptable compromise between considerations of overswing, output amplitude, and phase shift.

V_g depends on the resonant frequency, f_c, and the damping factor,η_c, of the ground-geophone coupling system as expressed in equation 5.2 (Krohn, 1984).

$$H_c(f) = \frac{1 \ + \ (f/f_c)^2}{1 \ - \ (f/f_c)^2 \ + \ j\eta_c(f/f_c)}. \tag{5.2}$$

f_c and η_c depend on soil consolidation and the weight and area of the geophone casing. They can be approximated by (Kimura, et al., 1997)

$$f_c = \frac{1}{\pi} \sqrt{\frac{\rho a}{(1-\sigma)m} c_s} \ , \tag{5.3}$$

and

$$\eta_c = 2a_{21} \sqrt{\frac{\rho a^3}{(1-\sigma)m}} \ , \tag{5.4}$$

where a and m are the radius and the mass of the case. ρ, σ, and c_s are the density, Poisson ratio, and the shear wave velocity of the soil. a_{21} is a constant, which depends on the Poisson ratio. The resonant frequency of the coupling system, f_0, is nonlinearly controlled by the amplitude of the recorded waves, f_0 becomes smaller with larger amplitude.

Figure 5.29 shows the approximate response of two geophones using equations 5.3 and 5.4. The blue curves are the response of a 40-Hz geophone with small rounded base, while the red curves are the response of a similar geophone but mounted on a heavy and narrow base. The effect of coupling on a recorded seismic signal can be inferred from this figure. If the total damping of the geophone is small, the peak amplitude is high and narrow, as the case for

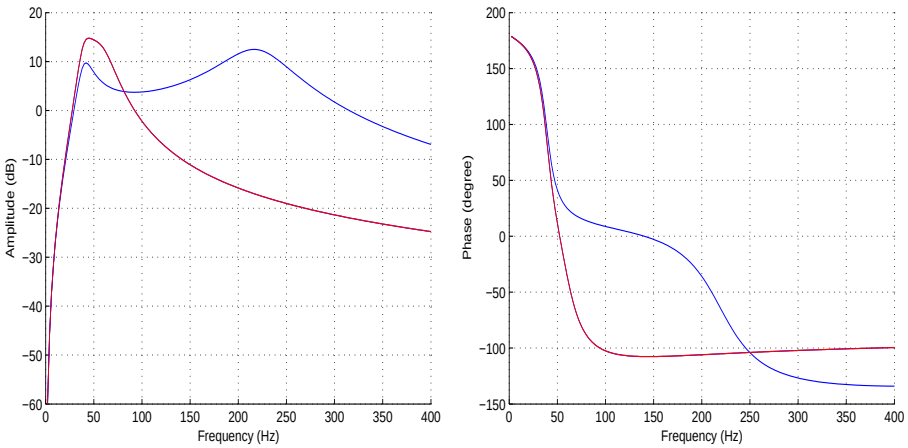

Figure 5.29. The response for two ground-geophone coupling systems in loose sand with $\rho = 1.6$, $\sigma = 0.48$, $a_{21} = 0.4$, and $c_s = 200$ m/s. Both geophones have a resonant frequency of $f_g = 40$ Hz and a damping factor $\eta_g = 0.4$. The mass and the radius for the case of the blue geophone are 5 g and 2 cm, and 800 g and 12 cm for the red geophone.

the red geophone. In this case, the coupling system acts as a low-pass filter. The amplitude near the resonant frequency is greatly enhanced, and the pulse will ring with this frequency. Above this frequency,however, the amplitude is reduced. For high damping, the peak amplitude is low and broad, as the case for the blue geophone. In this case, the amplitude is not drastically affected, but there would be phase distortion over a broad bandwidth of frequencies, which manifest itself as a time shift. Such time shift has been observed in all the datasets acquired above. Since the phase varies over a broad band, the magnitude of the time shift varies and depends on frequency and magnitude of the recorded signal.

Figure 5.30 shows the geophone-coupling system for two band-limited wavelets: 30-Hz and 100-Hz low-pass. Clearly the response of the 30-Hz wavelet is almost identical for both geophones except for a small magnifi-

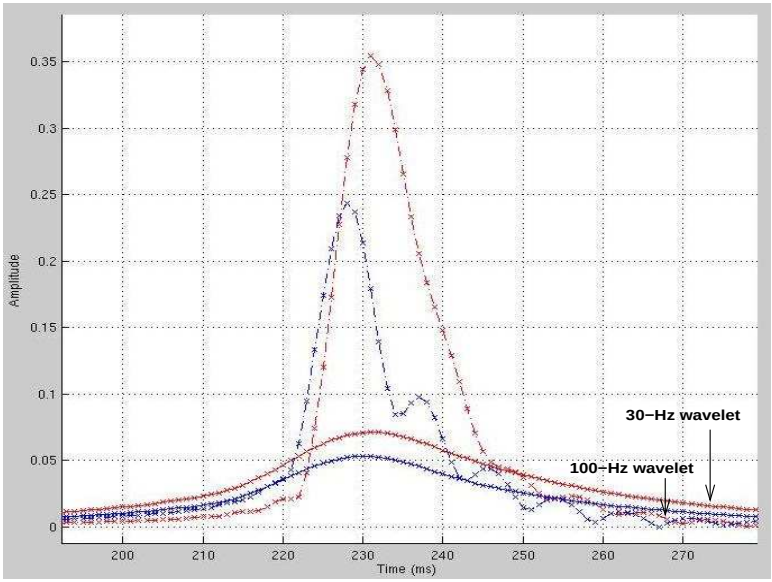

Figure 5.30. The response of two geophone-coupling systems for two band-limited wavelets: 30-Hz low-pass and 100-Hz low-pass. The blue curves are for the light geophone, while the red curves are for the heavy geophone, Figure 5.29

cation by the heavy geophone. The response of the 100-Hz wavelet shows a 3-ms time-lag and a noticeable magnification by the heavy geophone.

In exploration seismic, the resonant frequency is not very important because the recorded frequencies are way below this frequency. In shallow seismic surveys where the recorded frequencies might be as high as 300 Hz, great care should be taken in choosing the right geophone.

Equations 5.1 - 5.4 form a basis to study the optimal plate design. Two major variables need to be considered in the design: plate weight and area. A third factor for an optimal plate-design is the mobility which is actually an engineering problem.

Chapter 6

CONTRIBUTIONS AND FUTURE WORK

6.1 Contributions

This study illustrates the limitations of the refraction- and the uphole-based methods for imaging the near-surface in exploration seismic. The literature review in the first chapter covered the shortcoming of the uphole- and the refraction-based methods. These methods are considered the industry standard for estimating the near-surface velocity model. In certain cases, however, these methods might produce reasonably accurate models. Therefore, analysts need to be aware of their limitations. The new method of using shallow high-resolution data to build the near-surface velocity model overcomes most of these problems.

The analyst needs to study the geomorphology and geology of the near-surface to be able to make a judgment about which method is best for the the near-surface in the exploration area. This knowledge is also necessary to wisely choose the discrete points of investigation. The near-surface geology and geomorphology of the Arabian Peninsula were discussed in the context of the near-surface problem. Our study confirmed the need for a new method that provide better horizontal resolution and greater depth of investigation.

The horizontal and vertical resolution of the near-surface velocity model must be proportional to the heterogeneity of the near-surface. From the nu-

merical studies it is apparent that there is a need for a sufficiently spatially sampled velocity model. The sampling interval should be at least half the length of the smallest near-surface velocity anomaly. Undersampling the near-surface by drilling and sampling few shallow upholes does not resolve the long-wavelength statics as some geophysicists believe.

High-resolution seismic can provide a detailed high-resolution velocity model. In particular high-resolution reflection is an accurate alternative to drilling deep upholes at close distances. High-resolution shallow reflection seismic may not be applicable in certain areas. In such cases high-resolution refraction has provided an accurate velocity estimation. In either cases, the output is a high-resolution (in time and space) velocity model which can be used to compute the datum statics to the desired datum. Such a high-fidelity model is the key to the success of the more accurate wavefield extrapolation (redatuming).

The conventional stacking velocity analysis is the fastest and most robust velocity estimation method. To estimate velocities from the high-resolution seismic, I found that the velocities provided using conventional stacking velocity analysis are as accurate as reflection tomography. When there are clear continuous reflectors, this method is preferable. The velocities obtained using the high-resolution data were compared with true velocities measured through a check-shot survey. The velocities were in agreement within a few milliseconds.

Utilization of a land streamer in CMP mode is recommended to make the process of velocity model building or statics estimation more cost-effective. The process of acquiring data at discrete points mimics drilling an uphole at

every CMP location. The advantage is that the operation cost is reduced dramatically. A land streamer was designed and used to collect high-resolution data over sand dunes. It was found that the land-streamer data imaged shallow reflectors quite accurately. A non-stationary time shift between the conventional and the land-streamer data were observed. This phenomena was explained theoretically by the response of plate-mounted geophones. The analysis predicts an undesirable response for very heavy plates.

High-resolution shallow seismic surveys were designed, acquired and processed in the Central and the Eastern of Saudi Arabia. Over sand dunes, the input signal decayed rapidly which required using higher-energy sources. Nevertheless, shallow reflections, the shallowest at depth of 70 m, were imaged. The near-surface velocities were estimated to depths not usually attained by shallow upholes or by using refraction-based methods. The model can be used in seismic data migration by splicing it to the deep velocity model.

The new method of near-surface modeling not only increases the accuracy of the estimated velocity models, it reduce the operational cost of the exploration program. It also reduce the environmental impact of upholes drilling and the cycle time of exploration.

6.2 Future Work

The recommended and the more effective technique is base on acquiring high-resolution data in the CMP-mode. Therefore, A natural subsequent step should be implementing this technique in a 2D or 3D survey. These pilot surveys might employ a land streamer, which will cut more in acquisition time and cost.

This technique can be integrated with one of the advanced state-of-the-art single-sensor acquisition systems. Future work should investigate the possibilities of such integration, which might be more cost-effective. Such a multiple acquisition might requires using dual sources. Recently, digital geophones have become more widely used in the industry. Their frequency response has a broader bandwidth. Future work should compare these geophones with the conventional geophones.

The high-resolution field data in this dissertation were collected using using a mini vibroseis, a sledge hummer, or a downhole gun. For logistics reasons, the gun was not used in Saudi Arabia. Future work should examine using a powerful impulsive source to increase the resolution and depth of penetration. The mini vibroseis used in some of the high-resolution surveys above was a practical and fast seismic source. Future work need to optimizing the vibroseis parameters or study alternative seismic sources which will perform better in such sandy terrains.

The land streamer needs to be customized for use over sand dunes. The plates are the main performance factor in a land streamer. The plates should be designed in a way to eradicate the phase distortions. The designs should make the streamer easier to drag over soft sand. Since dragging a long streamer might not be practical, acquiring long offsets will require more studies. Similarly, designing a 3D streamer might be a research topic in the future.

The ability to estimate velocity from high-resolution data is hampered by the presence of non-random noise, such as guided waves. Future work should focus on special processes to filter the data, especially those which can filter aliased noise. Also, using a 3D CMP might help filtering noise and obtaining

more accurate velocities.

The velocity analysis process could be a future research topic. The velocities at a particular CMP location can be estimated using either reflection or refraction data. Future work might compare using the two modes separately of jointly to constrain the model.

REFERENCES

Al-Sayari, S.S. and Zotl, J.G. (eds.), 1978, Quaternary Period in Saudi Arabia, Volume 1: Sedimentological, Hydrogeological, Hydrochemical, Geomorphological, and Climatological Investigations in Central and Eastern Saudi Arabia: Springer-Verlag, Wien-New York, 335 p.

Alkhalifah, T., and Bagaini, C., 2004, Cost-effective datuming in presence of rough topography and complex near-surface: SEG Expanded Abstracts 2004.

Berryhill, J., 1984, Wave-equation datuming before stack: Geophysics, 49, p. 2064-2066.

Bridle, R., Ley, R., Al-Homaili, M., Al-Inaizi, S., and Boon, S., 2004, Near-surface layer model using first break arrivals applied to 3D blocks: SEG Expanded Abstracts 2004.

Cox, M., 1999, Static Corrections for Seismic Reflection Surveys: Soc. of Expl. Geophys., 531 p.

The Center for Wave Phenomena (CWP), ¡http://www.cwp.mines.edu/cwpcodes¿, 2005.

Diggins, C., Carvill, C., Daly, C., 1988, A Hybird Refraction Algorithm: SEG Expanded Abstracts 1988.

Dix, H., 1955, Seismic velocities from surface measurements: Geophysics, 20, p. 63-80.

Davis, J.L., and Annan, A.P., 1989, Ground Penetrating Radar for High-Resolution Mapping of Soil and Rock Stratigraphy: Geophysical Prospecting 37, p. 531-551.

GeoQuest International Ltd., 1976, Model Study of Near-Surface Anomalies: Aramco Research and Development (internal reoprt), 111 p.

Jado, A. and Zotl, J.G. (eds.), 1984, Quaternary Period in Saudi Arabia, Volume 2: Sedimentological, Hydrogeological, Hydrochemical, Geomorphological, and Climatological Investigations in Western Saudi Arabia: Springer-Verlag, Wien-New York, 360 p.

Kimura, M., Watanabe, H., and Kawashima, S., 1997, Coupling Characteristics between Geophone and Ground Model: Jpn. J. Appl. Phys., 36, p. 3354-3357.

Krohn, C., 1984, Geophone ground coupling: Geophysics, 49, p. 722-731.

Holberg, O., 1988, Towards Optimum One-Way Wave Propagation: Geophysical Prospecting 36, p. 99-114.

Hu, L., Al-Marzoug, A., Erickson, K., and Kelamkis, P., 2002, Imaging Complex Near Surface Anomalies via Model-based and Velocity-independent Solutions; Current Practice at Saudi Aramco: SEG Expanded Abstracts 2002.

Hunter,J. A., Pullan, S. E., Burns, R. A., Gagne, R. M., and Good, R. S., 1984, Shallow seismic-reflection mapping of the overburden-bedrock in-

terface with the engineering seismograph-some simple techniques: Geophysics, 49, 1381-1385.

Hunter, J., Pullan, S., Burns, R., Good, R., Harris, J., Pugin, A., Skvortsov, A., and Goriainov, N., 1998, Downhole seismic logging for high-resolution reflection surveying in unconsolidated overburden, Geophysics, 63, pp. 1371-1384

Ivanov, J., Miller, R., Xia, J., Steeples, D., 2005, The Inverse Problem of Refraction Travel Times, Part II: Quantifying Refraction Nonuniqueness Using a Three-layer Model, Pure appl. geophys. 162 p. 461-477.

Konert, G., Afifi, A., Al-Hajri, S., De Groot K., Al Naim, A., and Droste, H., 2001, Paleozoic stratigraphy and hydrocarbon habitat of the Arabian Plate, in Petroleum Provinces of the Twenty First Century: AAPG Memoir 74, p. 483-515.

Ley, R., Bridle, R., Al-Homaili, M., Amarasinghe, D., Al-Ali, M., Zinge, M. and Rowe, W., 2003, Development of Near Surface Models in Saudi Arabia for Low Relief Structures and Complex Near Surface Geology: SEG Expanded Abstracts 2003.

Li, J., Castagna, J., and Yu, Q., 2003, Robust tomography and tomostatics/wave-equation datuming examples: SEG Expanded Abstracts 2003, 1481-1484.

Rajasekaran, S., and McMechan, G., 1996, Tomographic estimation of the spatial distribution of statics: Geophysics, 61, 1198-1208.

Marsden, D., 1993, Static corrections-a review, part I, , II, and III: Leading Edge 12.

Miller, R. D., Steeples, D. W. and Brannan, M., 1989, Mapping a bedrock surface under dry alluvium with shallow seismic reflections: Geophysics, Soc. of Expl. Geophys., 54, 1528-1534.

Miller, R. D., 1992, Normal moveout stretch mute of shallow-reflection: Geophysics, 57, pp. 1502-1507.

Palmer, D., 1980, The generalized reciprocal method of seismic refraction interpretation: Soc. Expl. Geophys.

Powers, R. W., Ramirez, L. F., Redmond, C. D., Elberg, E. L., 1966, Geology of the Arabian Peninsula. Sedimentary Geology of Saudi Arabia: U.S. Geological Survey, Professional Paper 560-D, Washington, 147 p.

Riser, J. A., 2002, Quaternary Geology and the Environment: Springer Praxis, 290 pp.

Smith, D. G., and Jol, H. M., 1995, Ground penetrating radar: antenna frequencies and maximum probable depths of penetration in Quaternary sediments: Journal of Applied Geophysics, 33, 93-100.

Steeples, D., Baker, G., Schmeissner, C. and Macy, B., 1999, Geophones on a board: Geophysics, Soc. of Expl. Geophys., 64, 809-814.

Steeples, D. W., Miller, R. D. and Black, R. A., 1990, Static corrections from shallow-reflection surveys: Geophysics, Soc. of Expl. Geophys., 55, 769-775.

Steeples, D. W., and Miller, R. D., 1990, Seismic-reflection methods applied to engineering, environmental, and ground-water problems, in Ward, S. Ed., volume on Environmental geophysics, Review and Tutorial, 1, Soc. Expl. Geophys., 1-30.

Stefani, J. P., 1995, Turning-ray tomography: Gephysics, Soc. of Expl. Geophys., 60, 1917-1929.

Taner M., Wagner, D., Baysal, E., and Lu, L., 1998, A unified method for 2-D and 3-D refraction statics: Geophysics, 63, p 260-274.

Tsoflias, G., Steeples, D., Czarnecki, G., Sloan, S. and Eslick, R., 2006, Automatic Deployment of a 2-D Geophone Array for Efficient Ultra-Shallow Seismic Imaging, Geophys. Res. Lett., 33.

Van der Veen, M. and Green, G., 1998, Land streamer for shallow data acquisition: evaluation of gimbal-mounted geophones: Geophysics, 63, p 1408-1413.

Zanzi, L., 1990, Inversion of Refracted Arrivals: a Few Problems: Geophysical Prospecting 38, p 339-364.

Zhdanov, M. S., Geophysical Inverse Theory And Regularization Problems, 2002, Elsevier, Amsterdam.

Yilmaz,, O., 1987, Seismic data processing: Soc. of Expl. Geophys.